

2007

## Topology synthesis and size optimization of morphing wing structures

Daisaku Inoyama  
*University of Dayton*

Follow this and additional works at: [https://ecommons.udayton.edu/graduate\\_theses](https://ecommons.udayton.edu/graduate_theses)

---

### Recommended Citation

Inoyama, Daisaku, "Topology synthesis and size optimization of morphing wing structures" (2007).  
*Graduate Theses and Dissertations*. 3459.  
[https://ecommons.udayton.edu/graduate\\_theses/3459](https://ecommons.udayton.edu/graduate_theses/3459)

This Dissertation is brought to you for free and open access by the Theses and Dissertations at eCommons. It has been accepted for inclusion in Graduate Theses and Dissertations by an authorized administrator of eCommons. For more information, please contact [mschlange1@udayton.edu](mailto:mschlange1@udayton.edu), [ecommons@udayton.edu](mailto:ecommons@udayton.edu).

**Topology Synthesis and Size Optimization  
of Morphing Wing Structures**

Dissertation

Submitted to

The School of Engineering

UNIVERSITY OF DAYTON

In Partial Fulfillment of the Requirement for

the Degree of

Doctor of Philosophy in Aerospace Engineering

by

Daisaku Inoyama


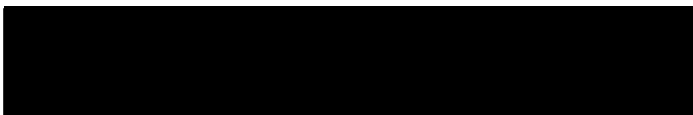



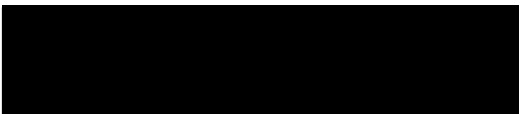
University of Dayton

Dayton, Ohio

May, 2007

## Topology Synthesis and Size Optimization of Morphing Wing Structures

APPROVED BY:

  
Brian P. Sanders, Ph.D.  
Advisory Committee Chair  
Adjunct Professor, Mechanical and  
Aerospace Engineering Department  
Robert A. Brockman, Ph.D.  
Committee Member  
Professor, Civil and Environmental  
Engineering and Engineering  
Mechanics Department  
Frank E. Eastep, Ph.D.  
Committee Member  
Professor Emeritus, Mechanical and  
Aerospace Engineering Department  
James J. Joo, Ph.D.  
Committee Member  
Assistant Professor, Mechanical and  
Aerospace Engineering Department  
Donald L. Moon, Ph.D.  
Associate Dean  
Graduate Engineering Programs & Research  
School of Engineering  
Joseph E. Saliba, Ph.D., P.E.  
Dean, School of Engineering

## **ABSTRACT**

### **TOPOLOGY SYNTHESIS AND SIZE OPTIMIZATION OF MORPHING WING STRUCTURES**

Name: Inoyama, Daisaku  
University of Dayton, 2007

Advisor: Dr. Brian Sanders

This research demonstrates a novel topology and size optimization methodology for synthesis of distributed actuation systems with specific applications to morphing air vehicle structures. The main emphasis is placed on the topology and size optimization problem formulations and the development of computational modeling concepts. The analysis model is developed to meet several important criteria: It must allow a rigid-body displacement, as well as a variation in planform area, with minimum strain on structural members while retaining acceptable numerical stability for finite element analysis. Topology optimization is performed on a semi-ground structure with design variables that control the system configuration. In effect, the optimization process assigns morphing members as “soft” elements, non-morphing load-bearing members as “stiff” elements, and non-existent members as “voids.” The optimization process also determines the optimum actuator placement, where each actuator is represented computationally by equal and opposite nodal forces with soft axial stiffness. In addition, the configuration of attachments that connect the morphing structure to a non-morphing structure is determined simultaneously. Several different optimization problem

formulations are investigated to understand their potential benefits in solution quality, as well as meaningfulness of the formulations. Extensions and enhancements to the initial concept and problem formulations are made to accommodate multiple-configuration definitions. In addition, the principal issues on the external-load dependency and the reversibility of a design, as well as the appropriate selection of a reference configuration, are addressed in the research. The methodology to control actuator distributions and concentrations is also discussed. Finally, the strategy to transfer the topology solution to the sizing optimization is developed and cross-sectional areas of existent structural members are optimized under applied aerodynamic loads. That is, the optimization process is implemented in sequential order: The actuation system layout is first determined through multi-disciplinary topology optimization process, and then the thickness or cross-sectional area of each existent member is optimized under given constraints and boundary conditions. Sample problems are solved to demonstrate the potential capabilities of the presented methodology. The research demonstrates an innovative structural design procedure from a computational perspective and opens new insights into the potential design requirements and characteristics of morphing structures.

## **ACKNOWLEDGEMENTS**

I would like to express my sincere gratitude to my dissertation advisor, Dr. Brian Sanders for his guidance, instruction and encouragement throughout my doctoral study. Dr. Sanders has provided me with many helpful advices from his expertise and experience in morphing technology and adaptive structures. His passion for advancement in morphing technology has always been a great inspiration to me. I am certain that I would not have progressed nearly as far without the instruction provided by Dr. Sanders. It is certain that I could not have had a better advisor. I really appreciate the valuable educational opportunities and challenges that Dr. Sanders has provided to me.

I would like to thank Dr. James Joo for his advice and assistance on topology optimization and numerous other details involved in the research. His vast knowledge and expertise in topology optimization and mechanism design has truly been an inspiration to me. When I was lost and did not know how to proceed with my research, Dr. Joo was always there to guide me with relevant advices that kept me moving forward.

I am grateful to Dr. Robert Brockman for his advice and instruction on finite element analysis and modeling. Many intricate details involved in the research are based on the knowledge and skills that I acquired from Dr. Brockman's finite element classes. Dr. Brockman's effective teaching style really made me understand many details of finite element analysis that certainly will be beneficial in my engineering career. I would also like to emphasize that Dr. Brockman has inspired me so greatly that I made a decision to

pursue a career in finite element analysis. It is my true opinion that Dr. Brockman is one of the greatest professors I have ever met.

I am greatly indebted to Dr. Frank Eastep who has provided me with valuable advices throughout the duration of my doctoral study. I feel very fortunate to be instructed by Dr. Eastep whose research credentials are well known in the aerospace field and who is greatly respected by peers. I was always fascinated with his decades of experience and knowledge in aerospace structures that are unparalleled and truly astounding. Dr. Eastep is the type of mentor who every young engineers, such as myself, would be very fortunate to have.

I would like to express appreciation to Dr. Kevin Hallinan of the Department of Mechanical and Aerospace Engineering. He has always been very kind to me and supportive of my research. His encouragements and helpful advices kept me motivated. I would also like to express special thanks to Carol Wilbanks who helped me a great deal with administrative issues in numerous occasions. I can imagine how stressful it may have been for me to deal with all the administrative mazes without her.

I would like to thank my wife, Kamala Limbu Inoyama, for her patience, love, and support. Throughout the duration of my doctoral study, she has always been there to motivate me. In many occasions, I felt discouraged mentally and physically. She has supported me both emotionally and morally and was always there for me with encouragements that put me back to the course. I have no doubt that I could have ever completed my doctoral study without her tremendous support and enthusiasm. I would also like to thank my parents, grand-parents, and brothers for their support during my

doctoral study. I also thank my ancestors for listening to my prayer and their continued protections.

Finally, I would like to acknowledge the support by Dayton Area Graduate Studies Institute (DAGSI) and Air Force Office of Scientific Research (AFOSR). Without their financial support, my doctoral study was never possible and I really appreciate them for providing me with the wonderful research opportunity at Air Force Research Laboratory.



## TABLE OF CONTENTS

ABSTRACT.....	iii
ACKNOWLEDGEMENTS.....	v
TABLE OF CONTENTS.....	viii
LIST OF FIGURES .....	xii
LIST OF TABLES.....	xiv
LIST OF SYMBOLS AND ABBREVIATIONS .....	xv
CHAPTER 1: INTRODUCTION.....	1
1.1 Motivations of the Research .....	1
1.2 Topology Optimization.....	4
CHAPTER 2: LITERATURE REVIEW .....	10
2.1 Introduction.....	10
2.2 Distributed Actuation.....	10
2.3 Actuator and Mechanism Integration.....	12
2.4 Optimization Techniques as Structural Design Tools .....	12
2.5 Research Focus .....	16
CHAPTER 3: ANALYSIS MODEL .....	18
3.1 Introduction.....	18
3.2 General Model Description.....	19
3.3 Line Element.....	20

3.4 Joint Element .....	21
3.5 Attachment Element.....	22
3.6 Flexible Skin Model.....	22
3.7 Cell Nodal Connectivity and Degrees of Freedom .....	23
3.8 Model Kinematics .....	25
CHAPTER 4: SINGLE CONFIGURATION FORMULATION .....	28
4.1 Introduction.....	28
4.2 Multiple Objective Minimization .....	29
4.3 Actuator Utilization Minimization with Shape-matching Constraints .....	32
4.4 Shape Error Minimization with Actuator Utilization Constraints .....	33
4.5 Combination of Formulations .....	34
4.6 Sensitivity Analysis .....	35
4.7 Solution Techniques.....	40
4.7.1 Sequential Quadratic Programming.....	40
4.7.2 Method of Moving Asymptotes .....	41
4.7.3 Globally Convergent Method of Moving Asymptotes .....	42
4.8 Example In-plane Problems and Results .....	43
4.8.1 Multi-Objective Case .....	44
4.8.2 Actuator Utilization Minimization with Shape Constraint Case .....	47
4.8.3 Shape Error Minimization with Actuator Constraint Case .....	49
4.8.4 Combinations of Formulations .....	51
4.9 Conclusion .....	53
CHAPTER 5: MULTIPLE CONFIGURATION FORMULATION .....	55

5.1 Introduction.....	55
5.2 Basic Multiple Configuration Problem Formulation .....	56
5.3 Sensitivity Analysis .....	61
5.4 Effect of Weight Constants.....	64
5.5 External-load Dependency and Reversibility .....	65
5.6 Actuator Distribution Control.....	67
5.7 Modified Relative Volume Constraint.....	70
5.8 Three-configuration Example Problem and Results .....	71
5.8.1 Base Solution .....	73
5.8.2 Solution with Modified Volume Constraints.....	76
5.8.3 Actuator Distribution Controlled Solution.....	78
5.9 Two-configuration Example and Results.....	82
5.10 Conclusion .....	85
CHAPTER 6: SIZE OPTIMIZATION .....	87
6.1 Introduction.....	87
6.2 Analysis Model Generation .....	88
6.3 Problem Formulation .....	90
6.3.1 Mean Positive Stress Constraint .....	92
6.4 Sensitivity Analysis .....	94
6.5 Example Problem and Results .....	96
6.6 Conclusion .....	100
CHAPTER 7: SUMMARY AND RECOMMENDATIONS .....	102
7.1 Summary .....	102

7.2 Future Research Direction and Recommendations.....	105
7.2.1 Material and Geometric Nonlinearity .....	105
7.2.2 Simultaneous Topology Synthesis and Size Optimization .....	106
7.2.3 Shape Optimization.....	107
7.2.4 Aeroelastic Equilibrium.....	108
APPENDIX A.....	109
APPENDIX B .....	116
REFERENCES .....	123

## LIST OF FIGURES

Figure 1 Spider Plot [Joshi et. al., 2004].....	3
Figure 2 General Problem Definition .....	5
Figure 3 Design Domain Representations .....	6
Figure 4 Representative Analysis Model .....	19
Figure 5 Line Element Configurations .....	21
Figure 6 Joint Element Configurations.....	21
Figure 7 Attachment Element Configurations .....	22
Figure 8 Cell Nodal Connectivity .....	24
Figure 9 Cell Degrees of Freedom.....	25
Figure 10 Joint and Line Element Kinematics.....	25
Figure 11 Model Kinematics .....	27
Figure 12 Line Stroke Length Definition.....	31
Figure 13 Shape Matching Definitions.....	32
Figure 14 Effect of Target Definitions.....	35
Figure 15 Method of Moving Asymptotes.....	42
Figure 16 Globally Convergent Method of Moving Asymptotes.....	43
Figure 17 Example Single-Configuration Problem Definition.....	44
Figure 18 Result: Multiple Objective Problem.....	47
Figure 19 Result: Actuator Utilization Minimization Problem .....	49

Figure 20 Result: Shape Error Minimization Problem .....	51
Figure 21 Result: Combination of Multi-objective and Actuator Problem .....	52
Figure 22 Result: Combination of Shape Error and Actuator Problem .....	53
Figure 23 Actuator Distribution Characteristics .....	68
Figure 24 Example Problem Description.....	72
Figure 25 Semi-ground Structure for the Example Problem .....	73
Figure 26 Base Solution.....	74
Figure 27 Solution with Modified Volume Constraint.....	77
Figure 28 Actuator Distribution Controlled Solution .....	80
Figure 29 Actuator Distribution Controlled Solution with Higher Control Parameter ...	81
Figure 30 Solution of Two Configuration Example .....	84
Figure 31 Multiple Stage Optimization Process .....	88
Figure 32 Line Element Sub-sectioning .....	89
Figure 33 Structural and Aerodynamic Model Integration.....	90
Figure 34 Topology Data for the Example Size Optimization Problem.....	97
Figure 35 Aerodynamics Models.....	98
Figure 36 Solution of the Example Problem.....	100
Figure 37 Effect of Convexity Parameter on the Convex Approximation .....	119

## **LIST OF TABLES**

Table 1	A Comparison of Solutions from Various Problem Formulations .....	54
Table 2	Comparison of Solutions: previous and new problem formulations .....	83
Table 3	Solution comparison for the three configuration example problem .....	86

## LIST OF SYMBOLS AND ABBREVIATIONS

$\rho, \rho_j$	=	Vector of design variables and its $j^{\text{th}}$ component in the set
$U_i^{TGT}, U_i$	=	Target and actual displacements at $i^{\text{th}}$ target degree of freedom
$T_j^{(i)}, U_j^{(i)}$	=	Target and actual displacements for $i^{\text{th}}$ configuration at $j^{\text{th}}$ target DOF
$U$	=	Vector of actual displacements
$U^{(i)}$	=	Vector of actual displacements for $i^{\text{th}}$ configuration
$W_i$	=	Weight/Scaling constant for $i^{\text{th}}$ objective term
$W_S^{(i)}, W_A^{(i)}$	=	Shape and actuator weight/scale constants for $i^{\text{th}}$ configuration
$K_i^{(R)}, K_i^{(NR)}$	=	Rotational and non-rotational stiffness matrix of $i^{\text{th}}$ joint element
$K_i^{(AX)}, K_i^{(NAX)}$	=	Axial and non-axial stiffness matrix of $i^{\text{th}}$ line element
$K_i^{(S)}, K_i^{(SN)}$	=	Sliding and non-sliding stiffness matrix of $i^{\text{th}}$ attachment element
$K_{skin}$	=	Simulated flexible skin stiffness matrix
$K$	=	Global stiffness matrix
$F_j^0$	=	Rated force vector of $j^{\text{th}}$ actuator
$F_{ext}^{(i)}$	=	External load vector for $i^{\text{th}}$ configuration
$F$	=	Global load vector
$S$	=	Equilibrium equations
$S^{(i)}, S_3^{(i)}$	=	2D and 3D equilibrium equations for $i^{\text{th}}$ configuration



$\beta, p, q, \alpha$	=	Penalty constants for joint, line, actuator, and attachment variables
$E_m^{(i)}$	=	Squared axial stroke length of $m^{\text{th}}$ line element for $i^{\text{th}}$ configuration
$E_{\max}^{(i)}$	=	Stroke limit of $m^{\text{th}}$ line element for $i^{\text{th}}$ configuration
$V_{\max}, V_{\min}$	=	Maximum and minimum allowable volume
$Tgt, A, J, L, B$	=	Target DOF set, actuator set, joint set, line set, attachment set
$\Omega_i, \Phi_i$	=	Set of coincident line element and actuator variables at $i^{\text{th}}$ location
$L1, L2$	=	Subsets of a line set
$A_i$	=	Subset of actuator set that corresponds to $i^{\text{th}}$ configuration
$\rho_{\min}$	=	Minimum value of design variables
$\varepsilon_{\max}$	=	Maximum allowable target DOF displacement error
$N_{\text{shape}}$	=	Total number of target shapes in the problem
$N_F$	=	Total number of fixed attachments allowed in the solution
$N_{\Omega}, N_{\Phi}$	=	Total number of line element and actuator locations in the model
$N_{tgt}$	=	Total number of target degrees of freedom at the morphing boundary
$N_L$	=	Total number of line elements in the model
$N_T$	=	Total number of target points in the model
$N_F$	=	Allowable number of fixed attachments
$G$	=	Spline matrix
$F_a$	=	Aerodynamic forces splined onto structural nodes
$P$	=	Aerodynamic forces on aerodynamic panels

$\gamma$	=	Specific weight
$A_i$	=	Size design variables of $i^{\text{th}}$ line element (chapter 6 only)
$\mathbf{A}$	=	Vector of size design variables
$l_i$	=	Length of $i^{\text{th}}$ line element
$\sigma_j^{(i)}$	=	Normal stress of $j^{\text{th}}$ line element for $i^{\text{th}}$ configuration
$ \sigma_j^{(i)} $	=	Mean normal stress of $j^{\text{th}}$ line element for $i^{\text{th}}$ configuration
$\sigma_{\max}$	=	Allowable normal stress
$A_{\max}, A_{\min}$	=	Maximum and minimum cross sectional area of line elements
$N_j^{(i)}$	=	Normal force in $j^{\text{th}}$ line element for $i^{\text{th}}$ configuration
$M_{z-j}^{(i)}, M_{y-j}^{(i)}$	=	Moments around z and y axes in $j^{\text{th}}$ line element for $i^{\text{th}}$ configuration
$\theta_j$	=	Angular orientation of $j^{\text{th}}$ line element
$u_{1-j}^{(i)}, u_{2-j}^{(i)}$	=	Local axial DOF of $j^{\text{th}}$ line element at nodes 1 and 2 for for $i^{\text{th}}$ configuration
$U_{1-j}^{(i)}, U_{2-j}^{(i)}$	=	Global axial DOF of $j^{\text{th}}$ line element at nodes 1 and 2 for for $i^{\text{th}}$ configuration
$V_{1-j}^{(i)}, V_{2-j}^{(i)}$	=	Global transverse DOF of $j^{\text{th}}$ line element at nodes 1 and 2 for for $i^{\text{th}}$ configuration
$\theta_{z1-j}^{(i)}, \theta_{z2-j}^{(i)}, \theta_{y1-j}^{(i)}, \theta_{y2-j}^{(i)}$	=	Rotational DOF around local z and y axes of $j^{\text{th}}$ line element at nodes 1 and 2 for $i^{\text{th}}$ configuration
$\Theta_{z1-j}^{(i)}, \Theta_{z2-j}^{(i)}, \Theta_{y1-j}^{(i)}, \Theta_{y2-j}^{(i)}$	=	Rotational DOF around global Z and Y axes of $j^{\text{th}}$ line element at nodes 1 and 2 for $i^{\text{th}}$ configuration

# **CHAPTER 1**

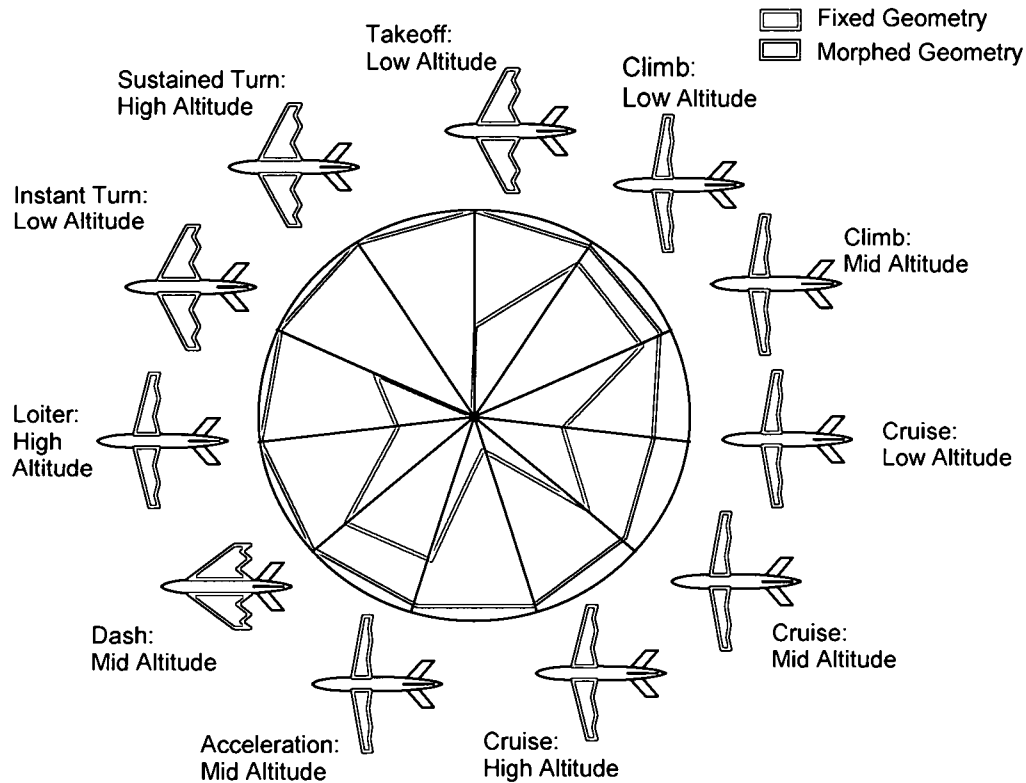
## **INTRODUCTION**

### **1.1 Motivations of the Research**

Conventional air vehicles are designed and optimized for specific flight conditions (level flight at cruise altitude, straight level climb, etc.). When the vehicle maneuvers away from this design point, the performance often declines dramatically. Therefore, the ability to adapt air vehicle aerodynamic shape to increase the optimum flight envelope is highly desirable. Although the shape morphing is technologically possible, its practicability and a balance between energy efficiency and system sophistication still remain as a major subject of investigation. The design of energy efficient morphing system is not an easy task, but this is an elusive goal that aeronautical engineers and scientists continually strive to achieve and keeps them motivated to invent new and innovative adaptive structural concepts.

Shape adaptive capability in air vehicles may be highly desirable for numerous reasons. First and foremost, such a capability can potentially enhance aircraft flight performance and efficiency dramatically, while attempting the operation across a broad envelop of flight conditions. The “spider plot” shown in Figure 1 is similar to the one presented by Joshi et. al. in their recent investigation [1]. The plot reveals the benefit of shape adaptive capability in air vehicles by illustrating relative efficiency measures of

morphing and fixed geometry vehicles for different phases of flight. Each radial line indicates a different phase of flight, such as take-off, cruise, or maneuver, with more versatile configurations occupying larger area within the circle along that direction. By observing a significant difference between two shades inside the circle, one can clearly see that fixed geometry air vehicles can only maintain their performance in certain areas while morphing air vehicles are capable of maintaining the performance all across the envelope. It is therefore apparent that the ability to continuously transform vehicle geometry provides a single air vehicle with a multiple mission capacity as it enables the vehicle to maintain and operate within the optimum or near-optimum flight envelope all the time, even as underlying flight dynamics may vary radically from mission to mission or segment to segment within a mission. Though the benefit of morphing is evident, the morphing structure must be designed, so that the shape adaptation cost does not overcome the potential advantage. This is a multi-disciplinary issue that requires an efficient integration of structural design, mechanism design, actuator placement, and aerodynamics.



**Figure 1 Spider Plot [Joshi et. al., 2004]**

Advancements in morphing technology will be attained not only from hardware development, but also from novel design methodologies. Conventional design methodology utilizes few large actuators to move large control surfaces in order to alter an effective aerodynamic shape of an air vehicle. However, for an air vehicle to maintain the optimum overall system efficiency, the vehicle must continuously adapt its configuration while simultaneously minimizing the total actuator utilization. The design of such an efficient morphing structure will certainly involve new and innovative design concept. Over the last century, air vehicle structures have evolved from the perspective of minimizing deformations. However, with our understanding of advanced structural designs, aeroelastic responses, and the development of modern actuator technologies and mechanisms, we are at the cusp of a design revolution in which we can control not only

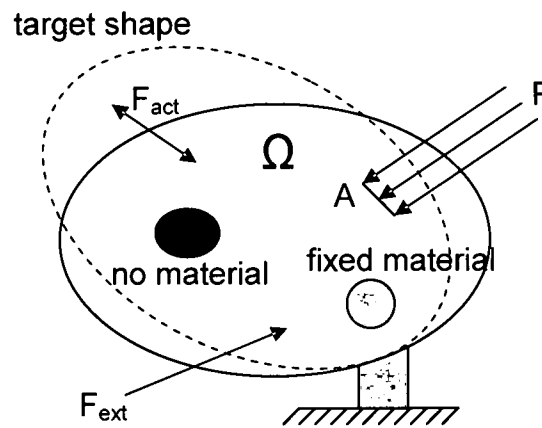
the deflection of control surfaces, but the shape of entire air vehicle components (i.e. wings).

Over the past decade, numerous investigations have been conducted for mechanism design, topology and structural optimization, actuator placement, and energy efficiency separately, but very little attention has been given to the combination of those disciplines. Therefore, the primary aim of this research is to develop an optimization-based computational tool required for efficient integrations of actuators, mechanisms, and elastic structures for design of morphing air vehicle structures. More specifically, the main focus of this research is to investigate topology and size optimization for design of an active actuation system that minimizes the total actuator requirement. The system will be constructed of actuators, mechanisms, load bearing structures, and aerodynamic loads. Furthermore, the system will allow rigid body motions in addition to elastic deformations.

## **1.2 Topology Optimization**

Topology synthesis of a morphing structure is not a simple task, often involving simultaneous solutions of multi-disciplinary problems with a large number of optimization variables. In spite of its complexity, topology optimization based design methodology is ideal for this research due to its capability to determine the optimum system configuration without well-defined initial conditions. For an application to morphing air vehicle design, complexity of multi-disciplinary topology optimization can be further exacerbated by large structural displacements and rigid body motions that arise from shape adaptations.

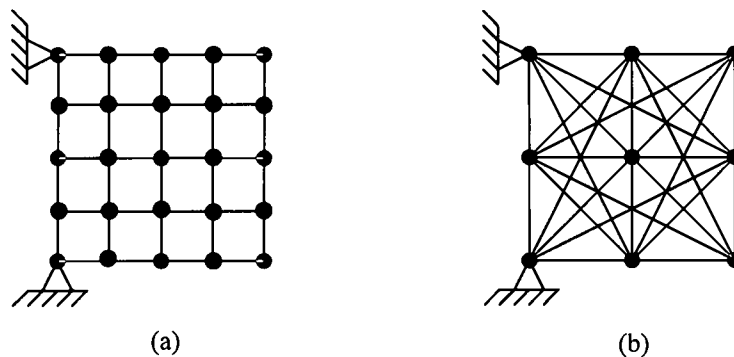
In general, any structural design contains definitions of topology, size and shape. The primary aim of topology optimization is to determine topology of structure using the given resources and surroundings. In order to perform a topology optimization, one must first define the problem to be solved. For instance, one may want to determine the structural layout that resists applied loads (point load  $F_{ext}$ , surface traction  $P$ ) and transfer actuation loads ( $F_{act}$ ) to cause a shape adaptation, given a design domain ( $\Omega$ ), boundary conditions, and imposed design criteria as shown in Figure 2.



**Figure 2 General Problem Definition**

After the problem definition is made, the topology optimization problem is formulated and numerical optimization techniques are applied to solve the problem. In topology optimization, there are two general approaches in defining the design domain, as shown in Figure 3. The first one is the material distribution method, where the domain is modeled as a continuous block of materials. In the material distribution method, topology optimization is performed to determine the existence of material within the design domain, according to the imposed boundary conditions. Another method is the ground structure method. In the ground structure method, every node in the design domain is connected to all other nodes by structural elements, such as frame, beam,

and/or truss elements. Topology optimization is applied to the ground structure to determine the existence of structural members. For both methods, the solution of a problem should reveal the complete structure or mechanism layout, depending on objective and constraint functions. There are advantages and disadvantages for each approach. In general, the ground structure method requires a smaller model with lower computational efforts to obtain a meaningful solution, while the material distribution method may provide better resolution and preciseness in a solution with higher computational requirements. Therefore, a choice of which approach to be utilized is problem dependent. In this research, the ground-structure method is considered appropriate due to the computational and modeling reasons.



**Figure 3 Design Domain Representations (a) Material Distribution (b) Ground Structure Methods**

Although there are numerous variations in problem formulations, the general topology optimization problem can always be written in the standard Non-Linear Programming (NLP) form:

Minimize:

$$f(\rho) \tag{1.1}$$

Subject to:

$$S(\rho) = 0 \tag{1.2}$$



$$V(\mathbf{\rho}) - V_{\max} \leq 0 \quad (1.3)$$

$$\rho_{\min} \leq \mathbf{\rho} \leq 1.0 \quad (1.4)$$

Here, (1.1) is the objective function and  $\mathbf{\rho}$  is a vector of design variables. The objective function may describe strain energy, output displacements, output energy or work, and other measures of structural design, depending on the problem. In case of morphing structural design, it may be natural to have an objective function that describes shape achievement and/or actuator utilization. (1.2) is the equilibrium condition that must be satisfied exactly and it is a function of design variables. The volume constraint (1.3) must be applied to the problem to ensure that the resulting structure conforms to design criteria. Side constraints (1.4) are applied to design variables. In topology optimization, design variables are generally kept between a small positive number  $\rho_{\min}$  and 1.0. Whenever design variables are assigned 1.0 or near, the corresponding elements are considered existent. Conversely, the elements are non-existent or void when design variables are at or near  $\rho_{\min}$ . Intermediate values are considered as “gray” and they are generally penalized strictly to prevent their excessive appearance in the solution. In addition to the constraints shown above, one can apply other constraints tailored to the problem. For instance, the problem formulation for mechanism or morphing structure design may require certain kinematics constraints.

One more important aspect of topology optimization that must be discussed here is a method to encourage design variables to be discrete 0 ( $\rho_{\min}$ ) or 1. If the non-gradient-based discrete optimization technique, such as Genetic Algorithm, is used to solve the problem, there is no extra step necessary to ensure 0-1 design. For the gradient based optimization technique, design variables are generally continuous in value. In such a

case, penalty constants are applied as exponent to design variables. The design variables are generally multiplied with the local stiffness of materials or elements with penalty constants as exponent:

$$K(\rho) = \sum_{m=1}^{N_{elem}} \rho_m^p K_m^{(e)} \quad (1.5)$$

One should notice the penalty constant ( $p$ ) in (1.5). Since the penalty constants are generally chosen to be 3.0 or greater, it becomes natural for optimization to choose discrete 0-1 solution due to steeper sensitivities near the upper bound. Clearly, more of such effects can be observed with higher values of these penalty constants, but one should note that numerical instability may arise if the design variables at the lower bound cause singularities in a stiffness matrix. It is important to remember that a void or an empty space in topology optimization is represented by a lower bound of the design variables and the singularity may result if the numerical value of design variable with large exponent becomes excessively low. Strategies for choosing these penalty constants are well explained in the text by Bendsoe and Sigmund [2].

It is clearly evident from the discussion above that topology optimization is capable of providing a conceptual design without a well-defined initial point (i.e. it only requires a design domain and boundary conditions). One should also note that topology optimization is a conceptual design tool and it is not meant to provide a detailed solution that can readily be transferred to CAD and manufactured. Topology optimization is a powerful conceptual design tool and is ideal for a research problem, such as the one encountered in this research, where the good starting point is probably unavailable or difficult even to imagine. In addition, topology optimization with appropriate design objective and constraints can possibly open new insights into design requirements and

characteristics of morphing structures. One of the main focuses of this research therefore is to investigate and pursue such potential benefits of topology optimization for design of morphing structures.

## **CHAPTER 2**

### **LITERATURE REVIEW**

#### **2.1 Introduction**

In order to develop a morphing air vehicle, it is necessary to revolutionize the basic construction of the structure to have controllable and desirable deformation and displacement characteristics built-in. This is a multidisciplinary issue that requires the efficient integration of power systems, structures, mechanisms, and actuators to achieve the desired performance, and the conventional design approach is not capable of performing this duty. In this section, some of the relevant design studies on issues related to morphing aircraft technology will be reviewed.

#### **2.2 Distributed Actuation**

Recently, several studies were conducted on the distributed actuation to control the performance of air vehicles [3,4,5]. One of the notable investigations by Gern et al. has demonstrated the possible advantage of morphing wing with distributed actuators, especially at the high speed [3]. The research was conducted on the equivalent plate model of generic Uninhabited Combat Air Vehicle (UCAV). The aerodynamics analysis involved the vortex lattice method together with Prandtl-Glauert compressibility correction. In the analysis, fully coupled static aeroelasticity was considered and flexible roll performance comparison of morphing and conventional air vehicles was made.

Beside its potential in system robustness and redundancy, the research has shown that distributed actuators may efficiently control wing morphing while achieving vehicle performance equivalent or superior to conventional control systems. Although researchers addressed the actuator energy requirement, they place no consideration to the impact of actuator placement or mechanism topology. In addition, the study only involved the airfoil morphing and no large-scale morphing was considered.

Another notable investigation on the morphing air vehicle focuses on the optimization with minimum actuator energy as an objective [4]. Researchers approached the problem analytically using a simplistic wing model with articulated control surfaces. By constraining flight performances together with static aeroelastic equilibrium, the research demonstrated that actuator energy requirement can be reduced due to the work done by the air stream on the wing in the aeroelastic environment. Researchers also explored the actuator energy requirement for deforming the two-dimensional airfoil to a certain shape. Although the research established an excellent example of morphing structure in aeroelastic environment, they did not include any consideration to the location of actuators and the design of mechanism. In addition, no aerodynamic and aeroelastic effects were considered for the two-dimensional airfoil case.

Several studies involving optimal actuator placement were conducted in the recent years [6,7,8,9,10,11]. One investigation demonstrates the minimization of the number of discrete actuators while achieving a specified flight performance [6]. The study utilizes a Genetic Algorithm (GA) to solve the actuator placement optimization problem and explained the characteristics of GA as applied to such problems. Moreover, researchers introduce an innovative method of aerodynamically defining an actuator by the source-

sink combination. It is an excellent approach, but the analysis model consists solely of rigid aerodynamic panels. Therefore, it lacks the effect of elastic and rigid-body structural deformations on the actuator placement.

### **2.3 Actuator and Mechanism Integration**

A recent research by Joo et al. on the energy based efficiency demonstrated the behavior of a coupled, loaded mechanism-actuation system of adaptive structures [12]. Researchers analytically developed a general methodology for evaluating the system energy efficiency through the investigation of interactions between external loads, actuators, and compliant mechanisms. The unloaded and loaded energy efficiencies of uncoupled and coupled actuator-mechanism systems were identified for general problems. In addition, the research addressed important issues on the variation of system energy efficiency due to the stiffness of components and geometrical alignment of the system. The research formed an important foundation to the understanding of fully coupled mechanism-actuation system efficiencies.

### **2.4 Optimization Techniques as Structural Design Tools**

The potential benefit of a topology optimization methodology as a mechanism design tool, in general, is well depicted in the study by Pedersen et al. [14]. The research describes the topology synthesis of a large-displacement compliant mechanism using nonlinear finite element analysis. In addition, the research explains a solution procedure for path-generation problems. A more recent study demonstrates the topology optimization process for a design of path-generating articulated mechanisms [15]. Though these investigations cover the general aspect of path-generation procedures, the

concept may possess close relationships, including its multi-objective nature, to the design of morphing air vehicle structures.

Recent studies by Maute et al. on the morphing wing mechanism illustrated that the topology optimization method has the potential to be applied to efficiently determine the optimum mechanism topology of a morphing air vehicle wing [16,17]. One of the investigations presents a material-based topology optimization methodology for the mechanism design of an in-plane morphing wing [16]. The study involves single and triple layer wing models to observe the artificial stiffness of the model and its effect on the mechanism topology. In addition, the effect of skin stiffness on the mechanism topology is demonstrated. Consideration and analyses are given to different problem formulations, including output energy maximization and shape matching. The globally convergent version of the method of moving asymptotes or GCMMA is utilized to solve the in-plane morphing problem. Although Maute established the foundation to the work being introduced here, no consideration is given to a combined actuator placement/topology optimization problem, as well as the determination of wing-fuselage attachments.

A research effort by Lu et al. on the mechanism topology demonstrated a synthesis of a compliant mechanism for morphing structural shapes using simultaneous topology and dimensional optimizations [18,19]. The study uses a Genetic Algorithm (GA) to simultaneously determine mechanism topology and dimensions by minimizing the coordinate errors between active and target points on shape changing boundaries. Several problem formulations are presented in their work, including point-wise least-square error and curve-wise Fourier transform (FT, DFT, and FFT) error minimization

problems. In addition, analyses and consideration are given to the variation of mechanism topology due to these formulations. Although the study has shown the versatility of topology optimization as applied to mechanism design, no consideration is given to actuator placement.

Among few recent investigations [15,20,21,22] that address the mechanization aspect of a morphing aircraft structure, one investigation [20] presents an innovative structural concept based on tendon-actuated compliant cellular trusses. The modeling concept includes the lattice of cells, constructed of truss members and compliant joints, actuated by pulling and/or releasing cables or tendons within each cell. The main feature of this concept is that the cells, by controlling appropriate tendons, can be made to behave as compliant mechanism locally and temporarily. Researchers demonstrate that collective local behaviors of each individual cell can be translated to a large-scale global shape change. In addition, consideration is given to the more detailed aspects of the concept, such as cell sizing and geometry, structural strength and weight, and potential skin designs. The subsequent investigation [21] involves the formulation and solution of topology optimization problem to optimally place tendons and trusses, using a specialized Genetic Algorithm (GA).

The potential effectiveness of optimization techniques in the design of a morphing air vehicle with multiple design points and criteria is demonstrated in few notable investigations [17,23]. One of the investigations demonstrates the topology optimization methodology for the design of a compliant mechanism for an airfoil shape adaptation [17]. The study involves the determination of an optimum airfoil shape and the corresponding mechanism topology, as well as actuator placements, to adapt the original



shape to the determined optimum shape. The researchers present the solutions of both coupled simultaneous approach, involving couple fluid-structure analysis, and decouple two-step approach. Another notable investigation addresses the multiple-objective nature of an optimization process for the design of morphing air vehicles at multiple configurations [23]. The investigation involves the performance optimization of buckled wing morphing air vehicle at its fused and parted configurations. The design variables that define various airfoil shapes of fused state and the parting line for two buckled airfoils are optimized to maximize lift-to-drag ratio of fused state and lift coefficient of the buckled airfoils. The researchers demonstrate both multiple-step and simultaneous approaches to solve the optimization problem. Though the investigations mentioned above do not consider a mechanism design that is capable of achieving multiple shapes or configurations, they provide excellent illustrations of how optimization techniques can be applied to the conceptual design of a morphing air vehicle.

The dimensional optimization of a compliant mechanism is demonstrated by Hetrick et. al. [24]. The investigation introduces the implementation of simultaneous size and shape optimizations to the existent compliant mechanism topology to maximize the mechanism output efficiency. The mechanism members are first subdivided into several segments (H-refinement) and parametric size design variables that represent cross-sectional area are applied to each segment. In addition, the shape optimization involves assignment of parametric shape design variables to active nodes that control the locations of these nodes within the predefined wander region. The values of size and shape design variables that maximize the energy output are determined using Sequential Quadratic Programming (SQP).

The adaptive system design via topology optimization technique is well demonstrated in a recent investigation by Trease et. al. [25]. The researchers demonstrate a topology optimization methodology for design of compliant mechanism system. The main focus of their research is the simultaneous synthesis of optimal structural topology and actuator placement for maximum output energy efficiency. Genetic Algorithm is utilized to perform a large integer optimization. The researchers also consider multiple stage process to consider sensing and control to the analysis. Although the investigation provides an excellent illustration of how topology optimization can potentially be employed for distributed actuation system design, many aspects of their investigation are not appropriate or ideal for design of morphing structures.

## **2.5 Research Focus**

Although the past investigations shown above pose an excellent illustration of the basic pieces of design for morphing structures, no work has been conducted on the combined system of real interest. Therefore, the main emphasis of this research is placed on the development of a reliable analysis model and the formulations of combined multi-disciplinary topology and size optimization problems that are excluded from the past investigations. The investigation is conducted on the combination of disciplines including mechanization, actuator placement, attachment determination and topology optimization. Several different problem formulations are introduced in this research. The first formulation involves the multi-objective function with total actuator utilization and shape-matching terms. The other formulations involve the choice of either actuator utilization or shape-matching as objective and the one not included in the objective function to be treated as a constraint. The potential benefits of combined or sequentially

executed formulations are investigated in some detail. In addition, the investigation involves the extension of the concept and problem formulations developed for the single configuration problem to those capable of accommodating multiple-configuration definitions. Finally, the size optimization is performed on the morphing structure obtained from the topology optimization process. The research demonstrates a novel computational design strategy that combines issues of mechanization, actuator placement, and topology synthesis in an integrated procedure for design of morphing structures.

## **CHAPTER 3**

### **ANALYSIS MODEL**

#### **3.1 Introduction**

In order to computationally represent general features of a morphing structure, an innovative finite element model must be conceived. The primary purpose of this chapter therefore is to introduce a novel computational modeling concept that can exhibit kinematics, load-bearing, and actuation characteristics of a morphing structure simultaneously using a variety of active and inactive components. In case of a morphing wing, a mechanized structure must undergo large rigid-body motions and planform changes without excessive elastic deformations. The actuation components must be embedded and distributed within the structure. In addition, the model must include means to consider external loads and an influence of flexible skin. The principal idea behind the modeling concept introduced in this chapter is based on a collective behavior of active and inactive structural components, variable stiffness joints, and actuation elements. Detailed descriptions of these elements, as well as their connectivity and combined kinematics characteristics, are provided in subsequent sections. In the following chapters, the analysis model is used as one of the key ingredients for the topology synthesis of morphing structures.

### 3.2 General Model Description

The in-plane morphing wing model introduced in this chapter is a semi-ground structure consisting of joint, line, attachment and flexible skin elements as shown in Figure 4. Although it is understood that more reliable results can probably be obtained from full- or other forms of semi-ground structure with finer mesh resolutions, this particular form is chosen for simplicity and to minimize computational efforts. In other words, the full ground structure shown in Figure 3b may provide the better representation, but the subset of it is used in this research to avoid the excessive computational cost. In order to determine the appropriate displacement boundary condition at the wing root that attaches to a non-morphing fuselage (simulated by imposed fixed displacement boundary condition), attachment elements are introduced at each point along the inner edge of the model. Aerodynamic drag loads are simulated by in-plane nodal forces at the wing leading edge as shown in the figure as vertical arrows. In this chapter, descriptions of the elements as well as their connectivity, degrees of freedom, and kinematics are discussed. One should note that the modeling concept is applicable beyond the simple in-plane wing model presented here for demonstration purposes. For instance, a model of much higher fidelity may be created using the same concept if the computational capability permits.

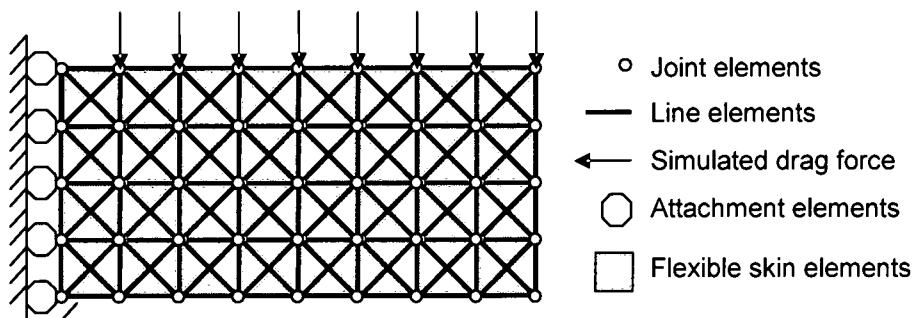


Figure 4 Representative Analysis Model

### 3.3 Line Element

The in-plane morphing wing model used in the investigation consists of a lattice of cells that contain definitions of joint, line and attachment elements as shown in Figure 4. Each line element assumes an appropriate configuration depending on the value of design variables that are determined by the optimization process, which is discussed later. Line elements in the model can be frames, trusses, telescoping members, or actuators as shown in Figure 5. Frame elements are conventional finite elements with axial and bending stiffness. Truss elements are the decompositions of frame elements and consist only of axial stiffness. Though the physical distinction between trusses and frames often do not exist, load-bearing characteristics of the structure may be revealed by observing the topology or the layout of these elements. Telescoping members are classified into two categories, active and inactive. Inactive telescopes are prismatic elements that have “very low” axial stiffness with beam bending stiffness and are not capable of delivering an actuation force. Whenever a telescoping member has an associated actuation force, the element is classified as an active telescope. An actuator is simply an element with equal and opposite nodal forces at its nodes. In other words, the primary difference between a simple actuator and an active telescope is that the latter one is capable of carrying bending loads internally. Both telescoping members and actuators have axial stroke limits that prohibit them from extending more than a predefined length, thereby preventing these elements from having unrealistically large strokes. In addition, actuator forces are limited to a certain predefined value. Whenever “very low” stiffness is present in all degrees of freedom, the element is considered as structurally or mechanically non-contributing and selected to be nonexistent or void. In the figure, arrows indicate the

available degrees of freedom for each configuration and the directions without arrows are considered as spurious modes that provides no resistance or stiffness.

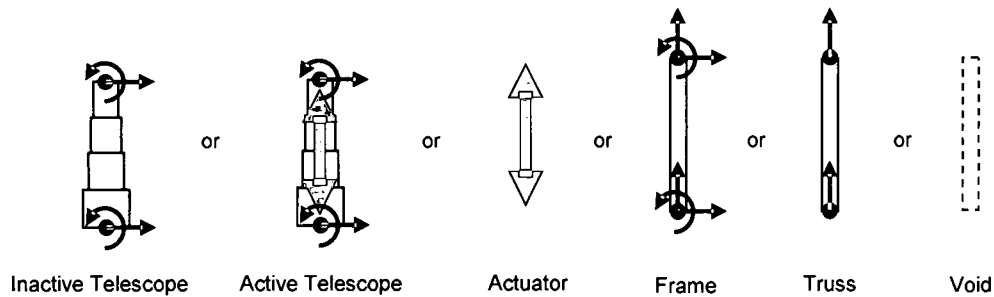


Figure 5 Line Element Configurations

### 3.4 Joint Element

Joint elements can be classified into the following types: revolute, compliant, or semi-rigid, as shown in Figure 6. These joints are analogous to rotational springs with variable rotational stiffness. Revolute joints can be considered as rotating hinges simulated by “very low” rotational stiffness and “very high” stiffness in all other directions. Conversely, semi-rigid joints have “very high” stiffness in rotational and all other directions. Compliant joints have intermediate rotational stiffness that can be physically interpreted as friction joints or high-strain joints. In addition to motions around these defined joints, rotations about truss elements are also possible as in the case of implicitly defined pinned joints in truss structures.

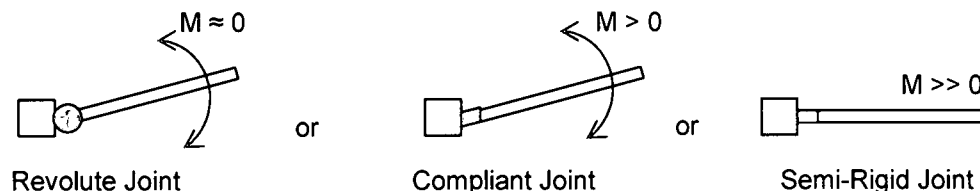
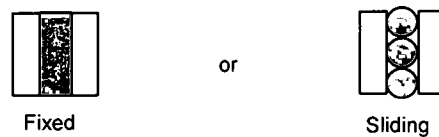


Figure 6 Joint Element Configurations

### 3.5 Attachment Element

Among several possible configurations for an attachment element, two primary ones, as shown in Figure 7, are considered in the model presented here. The attachments are modeled as linear springs with variable translational stiffness. The sliding boundary condition allows corresponding attachments to slide in a single translational direction along the fuselage, which is numerically represented by “very low” stiffness in a sliding direction and “very high” stiffness in other directions. The fixed boundary condition prohibits any motions by “very high” stiffness in entire degrees of freedom. Whenever a fixed or sliding boundary condition is connected to the structure through a revolute or compliant joint, it can be regarded as a pinned or sliding revolute attachment, respectively.



**Figure 7 Attachment Element Configurations**

The terms, “very low” and “very high”, are relative to the full stiffness of a frame element. Therefore, rigid-body motions are a result of relatively “soft” elements and, at the same time, structural strains are carried to the load resisting structure through relatively “stiff” elements. Evidently, “very low” and “very high” values must be chosen carefully to ensure numerical stability.

### 3.6 Flexible Skin Model

In addition to line, joint, and attachment elements, the model contains flexible skin elements. As reliable representation of a flexible morphing vehicle skin is not

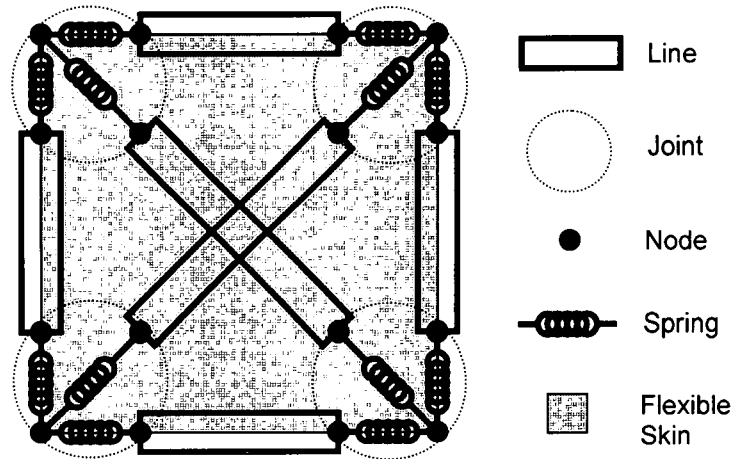


available at the moment, four-node rectangular elements with very compliant membrane stiffness are applied over each 'cell' to represent the flexible skin. Although the importance of reliable skin model is well understood, "pillowing" effect that arises from out-of-plane pressure loading is not a concern for the problem presented in this paper and, therefore, such a simple representation of flexible skin is considered to be sufficient.

This investigation deals only with linear FEM to keep the analysis at the conceptual level, but the model discussed above should be equally applicable to geometrically/materially nonlinear finite element cases, where stiffness and force boundary conditions are functions of displacement, with significant increase in computational costs.

### **3.7 Cell Nodal Connectivity and Degrees of Freedom**

The analysis model is composed of cells that contain line, joint, and flexible skin elements as shown in Figure 8. In the figure, the dashed circle denotes joint elements and every node located within this circle is coincident in physical space. One should notice that the joint element itself is a network of translational and rotational springs. As mentioned previously, these translational springs have relatively high stiffness and they do not allow detachment or separation of nodes within the joint. The rotational stiffness of springs can be varied to achieve desired characteristics of the structure and mechanism. Both ends of line elements are connected to one another through joint elements. Therefore rigid body rotations of line elements can be accomplished through rotational joints. In addition to line and joint elements, each cell contains a flexible skin element that is connected through center nodes of joints.



**Figure 8 Cell Nodal Connectivity**

Figure 9 illustrates the degrees of freedom of a single cell. The translational degrees of freedom within a cell are dependent of each other through stiffness. In other words, translational displacements of nodes within the joint are identical due to its connectivity with high stiffness translational spring. Although one may argue that such applications of high stiffness may cause numerical instability and that the same effect can be obtained by directly formulating the dependent degrees of freedom for these connections, such as the rigid-body elements that can be seen in the commercial program, the joint modeling technique employed in the research is considered ideal for the initial investigation and to keep the flexibility in modeling concept. In addition, numerical values of these high stiffness springs are kept at reasonable range approximately 10-100 times the maximum stiffness of the line element, depending on the problem, to avoid numerical ill conditioning of the global stiffness matrix.

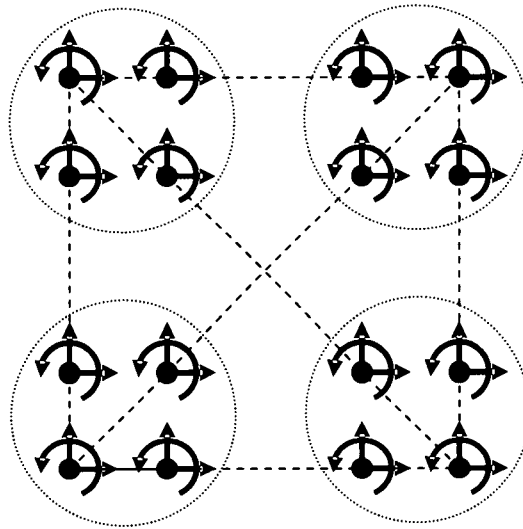


Figure 9 Cell degrees of freedom

### 3.8 Model Kinematics

In this section, the shape changing capability of the analysis model is discussed. In general, joint and line element combinations can make several fundamental motions, as shown in Figure 10. The figure reveals that the joint can be fully rotational (10a), fully semi-rigid (10d), or any combinations in between (10b, 10c). Though the figure shows only three line elements, any number of line elements can be connected through the joint.

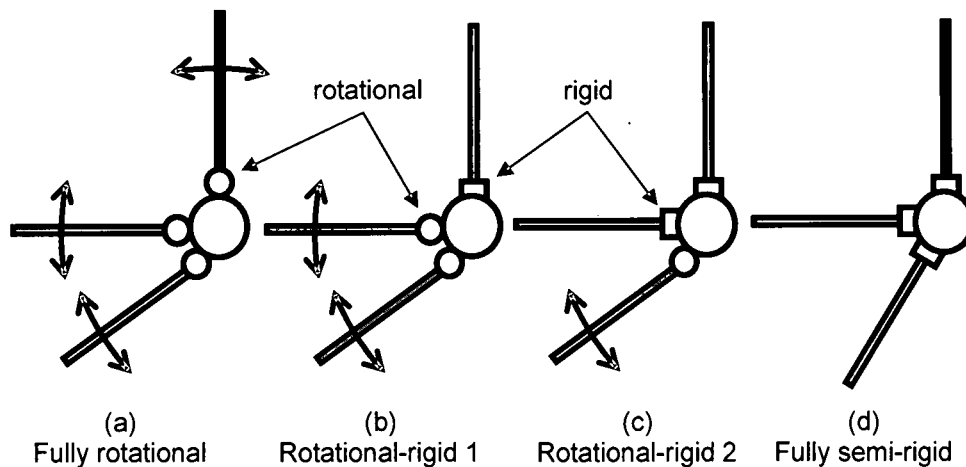
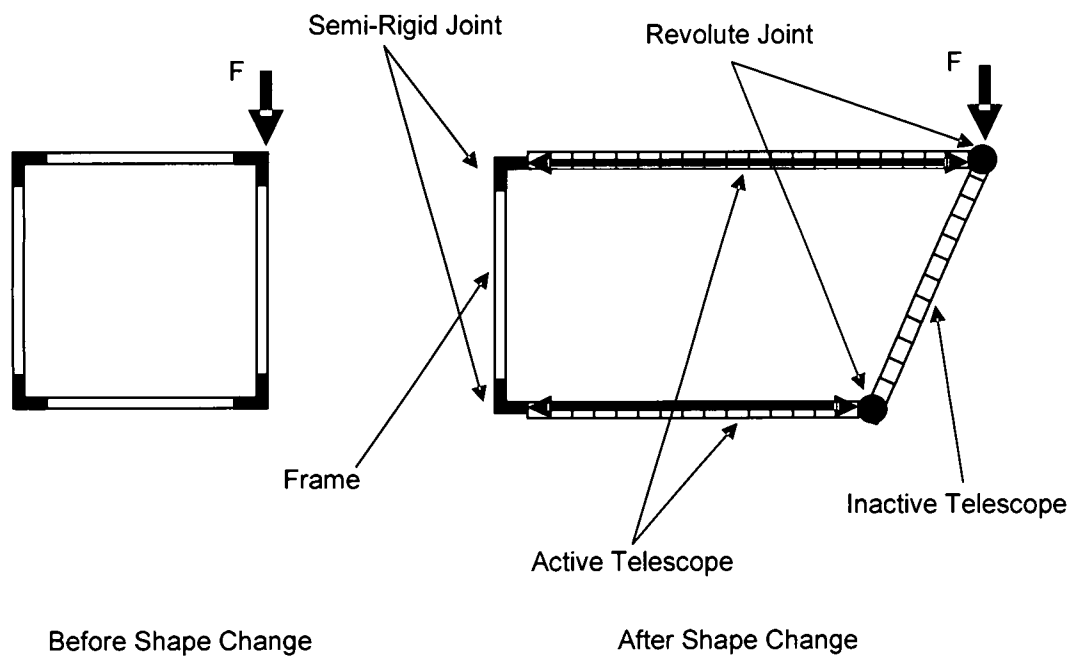


Figure 10 Joint and line element kinematics

For kinematics of the entire model, one can consider the effect of telescope and actuator elements as shown in Figure 11. There is an advantage and an associated disadvantage to this modeling concept. The primary advantage of the model is its absolute feasibility in attaining the target displacement. With the combinations of telescope and rotational joints, any nodal displacements of any magnitudes and directions can be attained. Therefore, there is no necessity for feasibility check before an analysis if the line stroke constraints are set to reasonable values and the mesh resolution is acceptable. Due to this shape adaptive capability of the model, there are also possibilities of trivial solutions. For instance, the structure made entirely of active telescope and/or actuators can attain any target shapes while it is also possible to resist any loading conditions. Clearly, morphing structure that is solely made of actuator or active telescopes is physically not desirable, though such a design is numerically feasible. Therefore, it is important to formulate the valid problem tailored to this modeling concept to avoid these trivial solutions. Application of valid design constraints, such as actuator limitations and structural volume constraints, is extremely critical in the problem formulation, which will be discussed in following chapters.



**Figure 11 Model kinematics**

## **CHAPTER 4**

### **SINGLE CONFIGURATION FORMULATION**

#### **4.1 Introduction**

In order to perform a topology optimization on the finite element model introduced in chapter 3, appropriate problem definitions and formulations must be made. For design of morphing wing structures, the topology optimization problem should be solved to determine a structural layout with consideration of shape achievement and actuator utilization minimization. In addition, appropriate design constraints, such as structural volume, element stroke limit, and allowable actuator utilization should be defined and included in the formulation.

Three different optimization problem formulations are introduced in this chapter. The first formulation involves a multi-objective function to minimize shape-matching error and actuator utilization simultaneously. The second and third formulations consist of a single objective with extra constraints to avoid notoriously weighting-dependent multi-objective formulation. Additionally, the sequential combinations of these formulations are considered. At the end of this chapter, an example problem is solved to demonstrate the potential effectiveness of the methodology presented in the chapter.

## 4.2 Multiple Objective Minimization

The multi-objective formulation (4.1)-(4.8) involves an objective function (4.1) with weighted sum of shape-matching error and actuator utilization terms. The constraints include the satisfaction of the static equilibrium condition (4.2), line element stroke limit (4.3), volume limit (4.4)-(4.5), attachment placement limit (4.6), and appropriate design variable limit (4.7)-(4.8). Although the multi-objective formulation is often discredited as unreliable, potential benefits of this formulation are not to be discounted here. The approach can be stated as:

Minimize:

$$f_0 = W_1 \sum_{i \in T} (U_i^{TGT} - U(\rho)_i)^2 + W_2 \sum_{j \in A} \rho_j^2 W_A^{(i)} \quad (4.1)$$

Subject to:

$$f_{eq} = KU - F = 0 \quad (4.2)$$

$$f_m = E_m^2 - E_{\max}^2 \leq 0 \quad m = 1, \dots, N_L \quad (4.3)$$

$$f_{+V} = \sum_{i \in L1} \rho_i + \sum_{i \in L2} \rho_i - V_{\max} \leq 0 \quad (4.4)$$

$$f_{-V} = -\sum_{i \in L1} \rho_i - \sum_{i \in L2} \rho_i + V_{\min} \leq 0 \quad (4.5)$$

$$f_F = \sum_{i \in B} \rho_i - N_F \leq 0 \quad (4.6)$$

$$\rho_{\min} \leq \rho_i \leq 1.0 \quad i \in J, L1, L2, B \quad (4.7)$$

$$-1.0 \leq \rho_j \leq 1.0 \quad j \in A \quad (4.8)$$

where  $K$  is the global stiffness matrix and  $F$  is the global load vector:

$$K = \sum_{i \in J} (\rho_i^\beta K_i^{(R)} + K_i^{(NR)}) + \sum_{i \in L1} (\rho_i^p K_i^{(AX)}) + \sum_{i \in L2} (\rho_i^p K_i^{(NAX)}) + \sum_{i \in B} (\rho_i^\alpha K_i^{(S)} + K_i^{(NS)}) + K_{skin} \quad (4.9)$$

$$F = \sum_{j \in A} \rho_j^q F_j^0 + F_{ext} \quad (4.10)$$

$f_0$  is the multi-objective function with shape-matching and actuator utilization terms. The static equilibrium condition is  $f_{eq}$  and it must be satisfied identically at every iteration. The design variables ( $\rho_i$ ) control the corresponding stiffness of each element as indicated in (4.9). Axial stroke constraints for line elements ( $f_m$ ) are expressed as the sum of the differences of squares of actual stroke length and maximum allowable stroke length. The “volume” range constraints ( $f_{+v}$  and  $f_{-v}$ ) do not represent the actual volume of the structure, but they instead correspond to the allowable range of the sum of line element design variables, where  $V_{max}$  is the upper limit and  $V_{min}$  is the lower limit. The attachment constraint ( $f_F$ ) defines the maximum allowable number of fixed attachments to a non-morphing structure or fuselage. The actuator utilization is the second term in the objective function which is expressed as the sum of squared actuator variables.

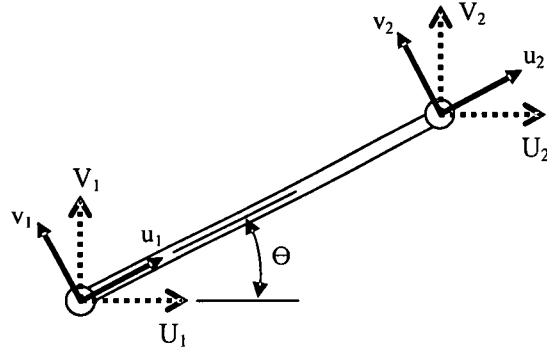
Figure 12 shows local and global translational degrees of freedom of a line element. The line stroke length  $E_m$  of the  $m^{\text{th}}$  line element is represented by a difference of local displacements in the line axial displacement:

$$E_m = u_2 - u_1 \quad (4.11)$$

The above equation can be converted to the global level by introducing the rotational transformation:

$$E_m = (U_2 \cos \theta + V_2 \sin \theta) - (U_1 \cos \theta + V_1 \sin \theta) \quad (4.12)$$





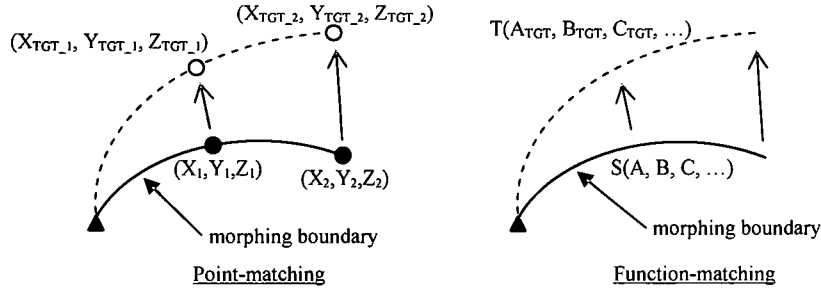
**Figure 12 Line Stroke Length Definition**

One may notice that local displacements in the transverse direction (i.e.  $v_1$  and  $v_2$ ) are not considered in the line stroke constraint. Since the only relevant elements for this constraint are telescope and actuator elements that are capable of making large elongation (or shrinkage) only in its axial direction, small relative displacements in the transverse direction are not expected to cause a significant effect in the solution. In addition, the constraints in transverse deformation is neglected to minimize the effect of this constraint on the void elements that should be capable of making any displacement in any direction.

The first term of the objective function is a shape-matching objective that is ideally zero when the actual displacements match the target displacements at the target points. In many cases, this type of point-wise shape matching may not be the best representation as it “forces” predefined target points in the structure to move to certain assigned locations. Instead, the target shape can be represented as a function, such as a spline or polynomial function, and let points along morphing boundary to position along a target function as shown in Figure 13. The function-wise shape matching term can be written as the sum of squared differences of actual and target shape function coefficients:

$$f_{shape} = (A(U) - A_{TGT})^2 + (B(U) - B_{TGT})^2 + (C(U) - C_{TGT})^2 + \dots \quad (4.13)$$

where the actual shape function is  $S(A,B,C,\dots)$  and target shape function is  $T(A_{TGT},B_{TGT},C_{TGT},\dots)$ . For the sake of simplicity and to minimize computational costs, point-wise matching is utilized in this research.



**Figure 13 Shape Matching Definitions**

Depending on optimization techniques, an appropriate scaling scheme can be applied to the above formulation to make the problem more suitable or numerically stable. The obvious disadvantage of this formulation is its dependency on objective weighting constants. Therefore, it is imperative to investigate other formulations that do not contain multiple objectives.

#### 4.3 Actuator Utilization Minimization with Shape-matching Constraints

This formulation has a single objective and an extra shape-matching constraint. Since the shape-matching can be considered as a requirement, instead of an objective, the following minimization problem can be solved along with constraints (4.2)-(4.8):

Minimize:

$$f_0 = \sum_{j \in A} \rho_j^2 \quad (4.14)$$

Subject to:

$$f_n = (U_n^{TGT} - U_n)^2 - \varepsilon_{\max}^2 \leq 0 \quad n = 1, \dots, N_T \quad (4.15)$$

Here,  $f_0$  is the objective function that aims to minimize the total squared actuator utilization.  $f_n$  is the shape-matching constraint for  $n^{\text{th}}$  target point and  $\varepsilon_{\max}$  is the maximum allowable displacement error for each point. One must note that this formulation has the disadvantage in the starting condition due to the fact that the optimization process must start with large shape constraint violation. Therefore, in order to solve this problem, optimization techniques must include means to treat large constraint violations. In such optimization techniques, constraint violation minimization may be performed prior to the minimization of supplied objective until the satisfaction of all violated constraints is achieved.

#### 4.4 Shape Error Minimization with Actuator Utilization Constraints

Another formulation that is worth investigating involves an objective function to achieve minimum shape-matching error and constraints to maintain the total squared actuator utilization within a defined range. This optimization problem, in conjunction with constraints (4.2)-(4.8), can be written as follows:

Minimize:

$$f_0 = \sum_{i \in T} (U_i^{TGT} - U(\rho)_i)^2 \quad (4.16)$$

Subject to:

$$f_{+A} = \sum_{j \in A} \rho_j^2 - A_{\max} \leq 0 \quad (4.17)$$

$$f_{-A} = -\sum_{j \in A} \rho_j^2 + A_{\min} \leq 0 \quad (4.18)$$

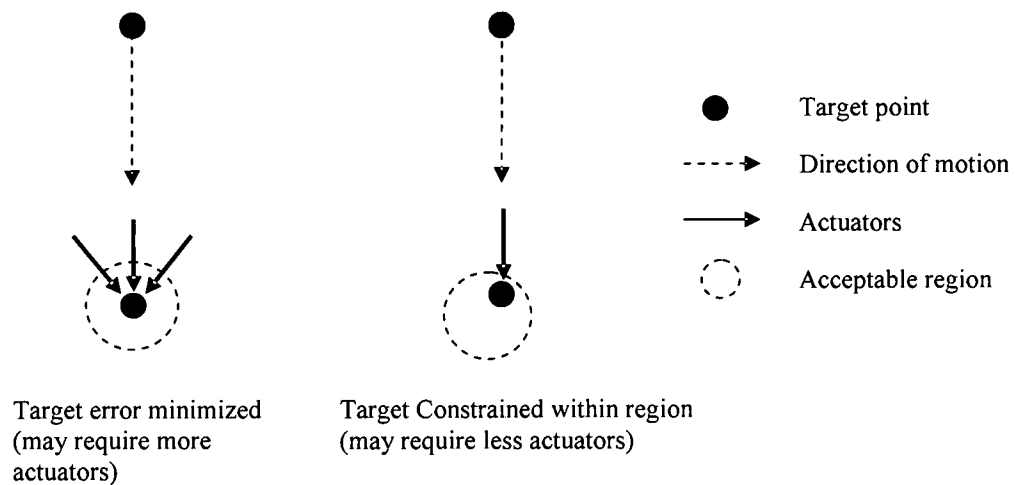
where the total squared actuator utilization constraints ( $f_{+A}$  and  $f_{-A}$ ) are defined as the maximum and minimum of the sum of squares of actuator variables.  $A_{\max}$  and  $A_{\min}$  are

constants that represent the allowable actuator utilization range. In addition, it should be noted that “utilization” does not indicate the “quantity” of actuators since the square of actuator variables are not necessarily discrete zero or one as they are often desired to be continuous in value.

#### 4.5 Combination of Formulations

Each formulation has advantages and disadvantages over one another. As previously mentioned, the multi-objective formulation has a disadvantage of being dependent on weighting constants. The actuator minimization formulation has large shape constraint violation at the initial iterations. Moreover, the total squared actuator utilization range must be known and assigned *a priori* in case of the shape error minimization formulation. Therefore, it may be beneficial to incorporate a process to execute the formulations in sequential fashion to cover the disadvantage of one formulation by the advantage of another formulation. For instance, one can consider the two-step process involving the multi-objective or shape error minimization formulation followed by the actuator utilization formulation, thereby avoiding the large shape constraint violation while the initial formulation is in effect. As soon as the shape error becomes small enough that target points are within the maximum allowable target point error or  $\epsilon_{\max}$ , one can change the formulation to that of actuator utilization minimization. At that moment, the balance between weighting constants or the assigned actuator value, whichever applicable, becomes irrelevant to the solution and the optimization process would find an optimal utilization of actuators while maintaining the acceptable target shape.

In terms of formulation definitions, the shape error minimization formulation may favor the “bull’s eye” target shape satisfaction because its sole objective is to minimize the shape error. The multi-objective formulation can consider both shape and actuator utilization simultaneously, though the shape objective should generally dominate the process at initial iterations in the process. The actuator minimization formulation may be able to find an optimum actuator utilization while maintaining the acceptable shape, but its large constraint violation at the initial stage in the process may prevent the solution from converging to the desired optimum, as the procedure to correct the constraint violation may not be reliable. The combined formulation may possess both the shape preciseness of multi-objective or shape error minimization formulations and the shape relaxation characteristics of actuator minimization formulation as shown in Figure 14.



**Figure 14 The Effect of Target Definitions**

#### 4.6 Sensitivity Analysis

Sensitivities of the objective function with respect to design variables are computed by the adjoint variable method, where equilibrium conditions are satisfied  $a$

*priori*. The displacement at the  $i^{\text{th}}$  degree of freedom can be expressed in terms of the global displacement:

$$U_i = I_i^T \mathbf{U} \quad (4.19)$$

Here,  $I_i$  is the vector with 1 in  $i^{\text{th}}$  component and 0 in all other components. Equivalently, one can write the above system with addition of a zero term:

$$U_i = I_i^T \mathbf{U} + \lambda_i^T (\mathbf{KU} - \mathbf{F}) \quad (4.20)$$

where  $\lambda_i$  is the multiplier that can assume any arbitrary values and the expression can still be valid. The sensitivity of this displacement component can be written as,

$$\frac{\partial U_i}{\partial \rho_e} = I_i^T \frac{\partial \mathbf{U}}{\partial \rho_e} + \lambda_i^T \frac{\partial \mathbf{K}}{\partial \rho_e} \mathbf{U} + \lambda_i^T \mathbf{K} \frac{\partial \mathbf{U}}{\partial \rho_e} - \lambda_i^T \frac{\partial \mathbf{F}}{\partial \rho_e} \quad (4.21)$$

The equation above can also be rearranged:

$$\frac{\partial U_i}{\partial \rho_e} = (I_i^T + \lambda_i^T \mathbf{K}) \frac{\partial \mathbf{U}}{\partial \rho_e} + \lambda_i^T \frac{\partial \mathbf{K}}{\partial \rho_e} \mathbf{U} - \lambda_i^T \frac{\partial \mathbf{F}}{\partial \rho_e} \quad (4.22)$$

Since the derivative of the global displacement vector cannot be obtained directly, one can set the first term to vanish by applying the following condition:

$$(I_i^T + \lambda_i^T \mathbf{K}) = 0 \quad (4.23)$$

The above condition is analogous to the simple static problem with an unit load applied to the  $i^{\text{th}}$  target degree of freedom and therefore should not cause any numerical instability, assuming that the global stiffness matrix is non-singular. By rearranging (4.23), one can obtain the following adjoint problem:

$$\mathbf{K} \lambda_i = -I_i \quad (4.24)$$

where  $\lambda_i$  can be solved and applied to (4.22) along with (4.23) to obtain manageable displacement sensitivity:

$$\frac{\partial U_i}{\partial \rho_e} = \lambda_i^T \frac{\partial K}{\partial \rho_e} \mathbf{U} - \lambda_i^T \frac{\partial F}{\partial \rho_e} \quad (4.25)$$

The gradient of objective function can be expressed as,

$$\frac{\partial f_0}{\partial \rho_e} = -2W_1 \sum_{i \in T} (U_i^{TGT} - U_i) \frac{\partial U_i}{\partial \rho_e} \quad e \notin A \quad (4.26)$$

$$\frac{\partial f_0}{\partial \rho_e} = -2W_1 \sum_{i \in T} (U_i^{TGT} - U_i) \frac{\partial U_i}{\partial \rho_e} + 2W_2 \rho_e \quad e \in A \quad (4.27)$$

By applying (4.25) to (4.26) and (4.27) along with the gradient of (4.9), one can obtain the objective sensitivity:

$$\frac{\partial f_0}{\partial \rho_e} = \begin{cases} -2W_1 \beta \rho_e^{\beta-1} \sum_{i \in T} [(U_i^{TGT} - U_i) \lambda_i^T K_e^{(R)} \mathbf{U}] & e \in J \\ -2W_1 p \rho_e^{p-1} \sum_{i \in T} [(U_i^{TGT} - U_i) \lambda_i^T K_e^{(AX)} \mathbf{U}] & e \in L1 \\ -2W_1 p \rho_e^{p-1} \sum_{i \in T} [(U_i^{TGT} - U_i) \lambda_i^T K_e^{(NAX)} \mathbf{U}] & e \in L2 \\ -2W_1 \alpha \rho_e^{\alpha-1} \sum_{i \in T} [(U_i^{TGT} - U_i) \lambda_i^T K_e^{(S)} \mathbf{U}] & e \in B \\ 2W_1 q \rho_e^{q-1} \sum_{i \in T} [(U_i^{TGT} - U_i) \lambda_i^T F_e^0] + 2W_2 \rho_e & e \in A \end{cases} \quad (4.28)$$

The sensitivity of stroke limit constraints (4.3) can be obtained in the same fashion. Let,  $\psi_m$  be the vector of positive and negative of sine and cosine of  $m^{\text{th}}$  line element coordinate as defined by (4.12):

$$\mathbf{E}_m = \boldsymbol{\psi}_m^T \mathbf{U} \quad (4.29)$$

Using the adjoint method, one can express (4.29) as the following form:

$$\mathbf{E}_m = \boldsymbol{\psi}_m^T \mathbf{U} + \boldsymbol{\eta}_m^T (\mathbf{K} \mathbf{U} - \mathbf{F}) \quad (4.30)$$

where  $\boldsymbol{\eta}_m$  is a  $m$ -vector of arbitrary numbers. As in the objective sensitivity case, the gradient of (4.30) can be written as,

$$\frac{\partial E_m}{\partial \rho_e} = (\psi_m^T + \eta_m^T K) \frac{\partial U}{\partial \rho_e} + \eta_m^T \frac{\partial K}{\partial \rho_e} U - \eta_m^T \frac{\partial F}{\partial \rho_e} \quad (4.31)$$

From the above equation, one can obtain the adjoint problem for the stroke constraint sensitivity,

$$K \eta_m = -\psi_m \quad (4.32)$$

where  $\eta_m$  is the solution to the adjoint problem for the  $m^{\text{th}}$  stroke limit constraint. Using the solution, one can evaluate (4.31) analytically as,

$$\frac{\partial E_m}{\partial \rho_e} = \eta_m^T \frac{\partial K}{\partial \rho_e} U - \eta_m^T \frac{\partial F}{\partial \rho_e} \quad (4.33)$$

The gradient of the stroke limit constraint (4.3) can be obtained:

$$\frac{\partial f_m}{\partial \rho_e} = 2E_m \frac{\partial E_m}{\partial \rho_e} \quad (4.34)$$

By applying (4.33) and (4.29) along with gradient of (4.9) and (4.10) to (4.34), one can obtain the following stroke limit constraint sensitivity:

$$\frac{\partial f_m}{\partial \rho_e} = \begin{cases} 2\beta \rho_e^{\beta-1} \psi_m^T U \eta_m^T K_e^{(R)} U & e \in J \\ 2p \rho_e^{p-1} \psi_m^T U \eta_m^T K_e^{(AX)} U & e \in L1 \\ 2p \rho_e^{p-1} \psi_m^T U \eta_m^T K_e^{(NAX)} U & e \in L2 \\ 2\alpha \rho_e^{\alpha-1} \psi_m^T U \eta_m^T K_e^{(S)} U & e \in B \\ -2q \rho_e^{q-1} \psi_m^T U \eta_m^T F_e^0 & e \in A \end{cases} \quad (4.35)$$

The sensitivities of volume and attachment constraints (4.4)-(4.6) are straight forward and they can be expressed as follows:

$$\frac{\partial f_{+V}}{\partial \rho_e} = \begin{cases} 1.0 & e \in L \\ 0.0 & e \notin L \end{cases} \quad \frac{\partial f_{-V}}{\partial \rho_e} = \begin{cases} -1.0 & e \in L \\ 0.0 & e \notin L \end{cases} \quad (4.36)$$

$$\frac{\partial f_F}{\partial \rho_e} = \begin{cases} 1.0 & e \in B \\ 0.0 & e \notin B \end{cases} \quad (4.37)$$



The objective function (4.14) of the actuator utilization minimization formulation has a compact objective sensitivity:

$$\frac{\partial f_0}{\partial \rho_e} = \begin{cases} 2.0\rho_e & e \in A \\ 0.0 & e \notin A \end{cases} \quad (4.38)$$

The sensitivities of shape constraint functions (4.15) are identical to that of the shape term of the multi-objective formulation. The gradient of (4.15) can be written as,

$$\frac{\partial f_n}{\partial \rho_e} = -2U_n \frac{\partial U_n}{\partial \rho_e} \quad (4.39)$$

By applying the gradient of displacement components (4.25) into the above equation, one can obtain the following shape constraint sensitivity:

$$\frac{\partial f_n}{\partial \rho_e} = \begin{cases} -2\beta\rho_e^{\beta-1}(U_n^{TGT} - U_n)\lambda_n^T K_e^{(R)}\mathbf{U} & e \in J \\ -2p\rho_e^{p-1}(U_n^{TGT} - U_n)\lambda_n^T K_e^{(AX)}\mathbf{U} & e \in L1 \\ -2p\rho_e^{p-1}(U_n^{TGT} - U_n)\lambda_n^T K_e^{(NAX)}\mathbf{U} & e \in L2 \\ -2\alpha\rho_e^{\alpha-1}(U_n^{TGT} - U_n)\lambda_n^T K_e^{(S)}\mathbf{U} & e \in B \\ 2q\rho_e^{q-1}(U_n^{TGT} - U_n)\lambda_n^T F_e^0 & e \in A \end{cases} \quad (4.40)$$

In the shape error minimization formulation, the objective function sensitivities are determined as in the multi-objective case and are identical for line, joint, and attachment variables. For actuator variables, the objective function sensitivity can be written as follows:

$$\frac{\partial f_0}{\partial \rho_e} = 2q\rho_e^{q-1} \sum_{i \in T} [(U_i^{TGT} - U_i)\lambda_i^T F_e^0] \quad e \in A \quad (4.41)$$

The sensitivities of the constraint functions are identical to those of the multi-objective case, except that the formulation has additional actuator constraint sensitivities:

$$\frac{\partial f_{+A}}{\partial \rho_e} = \begin{cases} 2.0\rho_e & e \in A \\ 0.0 & e \notin A \end{cases} \quad \frac{\partial f_{-A}}{\partial \rho_e} = \begin{cases} -2.0\rho_e & e \in A \\ 0.0 & e \notin A \end{cases} \quad (4.42)$$

## **4.7 Solution Techniques**

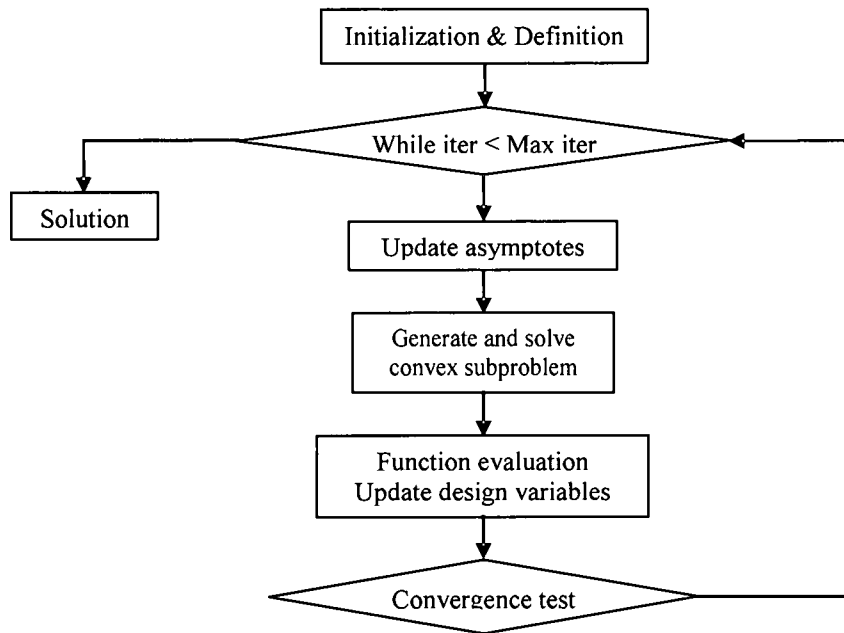
The topology optimization problems that were formulated in the earlier sections must be solved using an appropriate numerical optimization technique. Though there are two major categories of numerical optimization, gradient and non-gradient based techniques, the first one is considered exclusively in this research due to its obvious advantage of fast convergence to a local optimum. In addition, the optimality of solution can be assured in many cases using KKT optimality criteria. There are many types of gradient based method, but a few common techniques that are considered ideal for solving topology optimization problems will be discussed in this section.

### **4.7.1 Sequential Quadratic Programming**

The Sequential Quadratic Programming (SQP) is one of the widely used gradient based techniques for nonlinear constrained problems. It is efficient and accurate in the case of highly nonlinear and non-convex problems [26]. In addition, it is considered one of the standard nonlinear programming tools due to its robustness and reliability. In this method, a direction-finding sub-problem is solved first. Using the determined direction, one-dimensional search is then performed to minimize the objective function. The design variables are updated accordingly and the process continues until the convergence criterion is satisfied. Although SQP is considered one of the most robust and well behaved techniques for structural optimization, the technique failed to provide a converged solution for a large topology optimization problem encountered in the research.

#### **4.7.2 Method of Moving Asymptotes**

The Method of Moving Asymptotes (MMA) is one of the most extensively-used methods for structural optimization. This gradient based method is based on the approximation of the objective function and constraints with convex functions about the design point. In MMA algorithm, original implicit functions are written in terms of upper and lower asymptotes to transform them into explicit convex approximations. As the optimization process progresses to the optimum point, upper and lower asymptotes move closer to each other. The biggest advantage of convex approximation is that a local optimum is guaranteed as long as there is a feasible design domain. In addition, MMA is very stable for problems with many design variables and constraints. Over the past several years, several investigations have shown that a convex approximation method, such as MMA, is especially effective for topology optimization [27]. In this research, the predecessor of MMA (GCMMA) is selected to be utilized in solving topology optimization problems for a reason that will be discussed next. Further discussion of MMA is provided in Appendix A. Figure 15 shows a flow chart of MMA.



**Figure 15 Method of Moving Asymptotes**

#### **4.7.3 Globally Convergent Method of Moving Asymptotes**

In some cases, the classic Method of Moving Asymptotes (MMA) algorithm has a tendency to oscillate about an optimum point. The classic MMA is particularly susceptible to oscillation in least-square problems, such as the node-wise shape-matching problem in this research. To overcome this potentially troublesome behavior, Svanberg [28] introduced the globally convergent version of the classic MMA algorithm. In every iteration of Globally Convergent Method of Moving Asymptotes (GCMMA), the evaluation of conservatism of sub-problem is performed and convexity of approximation is adjusted accordingly. With all the advantages of MMA and additional features to ensure convergence, GCMMA is the technique of choice in this research. Further details of GCMMA are provided in Appendix B for interested readers. Figure 16 shows a flow chart of GCMMA.

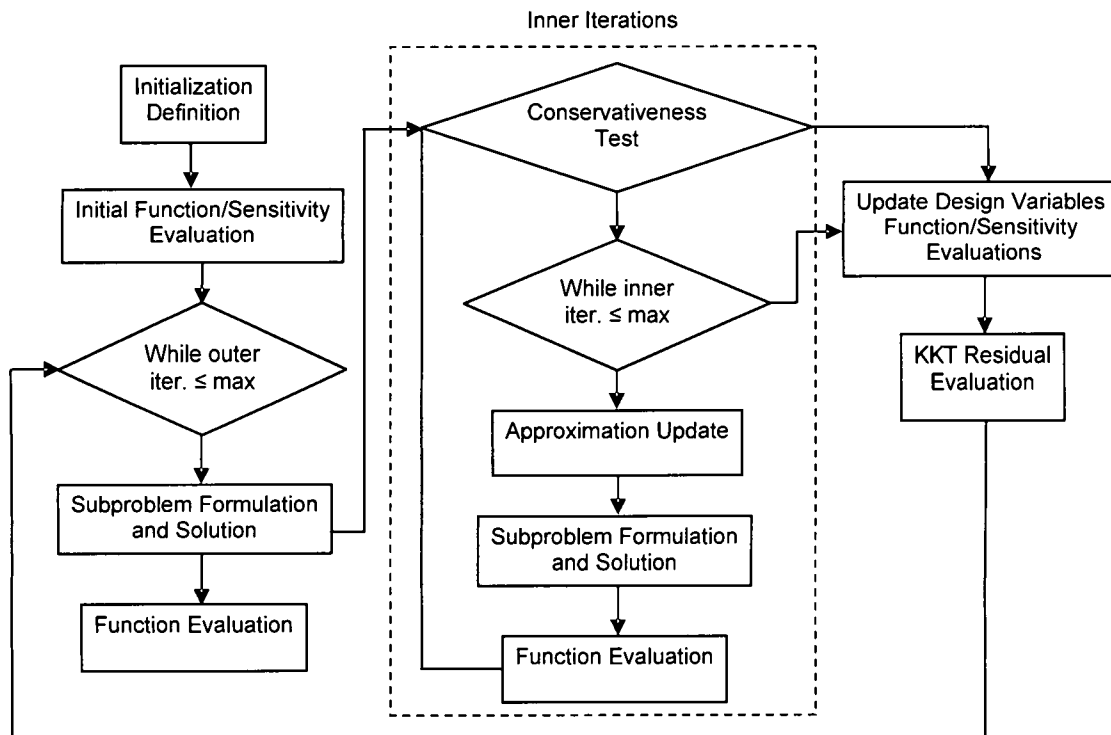
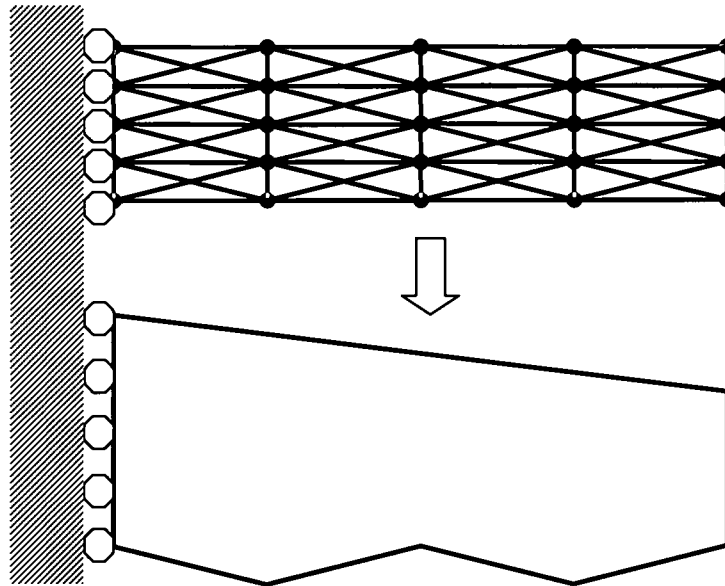


Figure 16 Globally Convergent Method of Moving Asymptotes

#### 4.8 Example In-plane Problems and Results

The sample problem provided here includes the main characteristics of an in-plane morphing wing as shown in Figure 17. First, it involves a large rigid-body rotation that results from a sweeping motion of the wing. In addition, it includes a dramatic variation in a planform shape with 37.5 percent increase in wing area. The initial configuration of the model is a rectangular semi-ground structure of 4 x 4 cells with evenly distributed initial design variables. The outer line of the structure is assigned as a morphing boundary which ideally matches the target boundary shape after the optimization process. Solutions are obtained using all problem formulations introduced in the previous sections. For all cases, predefined parameters are assigned identically to facilitate the valid comparison.

The physical and material properties of the full frame element are chosen to resemble a frame with 1 inch x 1 inch square cross-section that is made of a common aluminum alloy. The beam and truss elements are decompositions of the frame structure with the same physical and material properties. Consequently, the elasticity modulus of these line elements is allowed to vary between  $1e7$  and  $1e-5$  psi. The membrane stiffness of the skin elements is selected to be 100 psi with Poisson's ratio of 0.3 and a thickness of 0.1 inch. Although one may argue that the skin stiffness is excessively low, the artificial shear stiffness that may present in the linear rectangular element must be considered. In other words, such an artificial stiffness is compensated by intentionally applying the low elastic modulus value. As noted previously, further investigations are required to model the flexible skin more effectively.



**Figure 17 Example Single-Configuration Problem Definition**

#### **4.8.1 Multi-Objective Case**

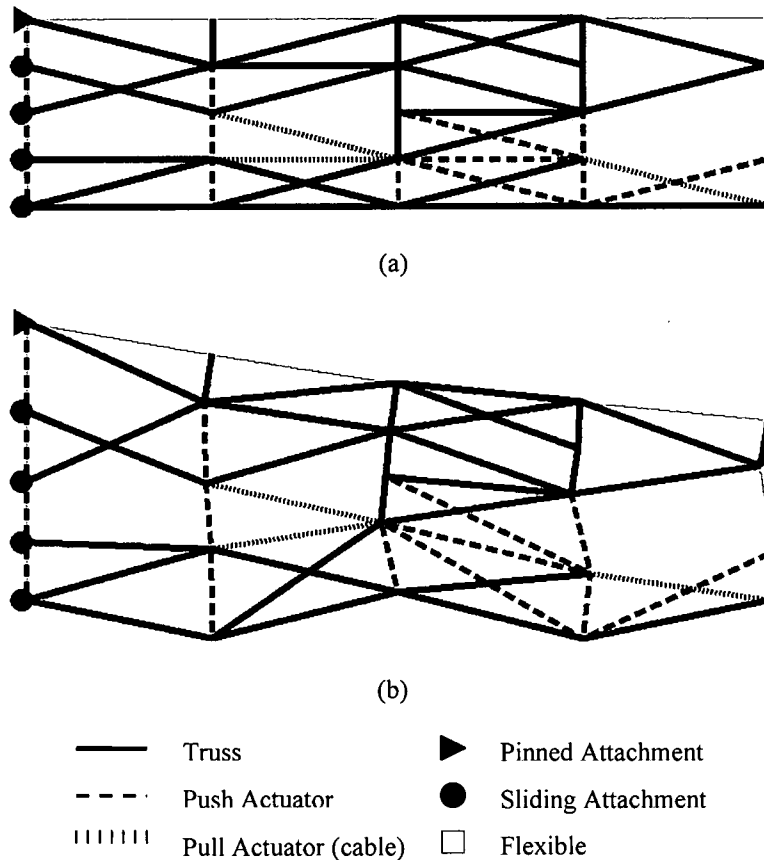
In this particular problem, the desired relative volume parameter is selected to be 0.25 or below. This relative volume parameter value prevents the total number of

structural elements (i.e. frame, telescope, truss) in the converged solution from exceeding 50 percent of the initial volume. As a consequence, all line element design variables are initially assigned at or below this value in order to avoid a volume constraint violation. The initial values of the actuator variables are somewhat arbitrary unless the utilization value is constrained to fall within a specific range, but some initial values may be better than others as in any other optimization problem. The weighting constant for the actuator minimization term is chosen not to be excessively underweighted, as the shape-matching term tends to dominate in initial iterations.

In Figures 18a and 18b, it is clearly visible that the initial wing design (semi-ground structure in Figure 17) that consists of 72 line elements has been reduced to a more compact morphing structure. In addition, the optimization process has determined 17 actuator positions (3 pull and 14 push actuators) among 72 possible locations. The solution only contains truss elements, though capabilities to select beam or frame elements with bending stiffness are provided in the program. This is an understandable outcome, especially for the in-plane problem selected for this demonstration, as the best direction to transfer or resist loads for any bar-type element is along its axial coordinate. The configuration of the joint elements, in this all-truss solution, is through the rotational characteristics of truss element as described in Chapter 3. This is not necessarily the case for other problems with different target shape and loading conditions. The figures also reveal larger accumulations of structural components in the leading-edge section and lesser in the trailing-edge section. One can hypothesize that this structural build-up at the leading-edge is essential to handle the simulated external loads and to transform the loads into the sweeping moment to cause a large rotational wing motion, minimizing the use of

actuators for the purpose. As the aft section lacks the assistance of external loads, it requires actuators to cause small shape changes and expand the wing area. In addition, an actuator appears in a somewhat unorthodox location, where the actuator pushes onto the wing tip against the flexible skin. The cause of this phenomenon is probably inherent to the optimization process and correlated to the modeling deficiency of a flexible skin. As the structure at the leading edge sweeps backward, it compresses the skin and creates a “fishtail” shape at the wing tip. The ideal skin design should not cause any motions that require an independent actuator to counteract. Instead, the flexible skin should flow naturally into the target shape as it deforms. Although this is clearly an undesirable characteristic of the flexible skin model, the optimization program strives to correct the situation as the shape error minimization is one of its main objectives. For this particular instance, the optimization process outweighs the shape match and determines that it is more beneficial to use actuators to correct this shape error. The displacement behavior of the skin can possibly be modified to correct the situation. The total absolute actuator utilization (i.e. sum of absolute value of actuator design variables) for the case has been found to be 4.267 with the total normalized shape error (i.e. total shape error / total target shape change) of 0.0784, indicating that the target shape is met with approximately 93 percent accuracy with reasonable actuator utilizations. At the attachment section, it is clearly visible that the optimization process determined the proper configuration to accommodate the desired shape change. In terms of accuracy and reliability of this result, one can observe that some parts of the structure may not be physically correct to make such motions. One main reason for this defect can be traced to linear FEM used in this large-displacement analysis.





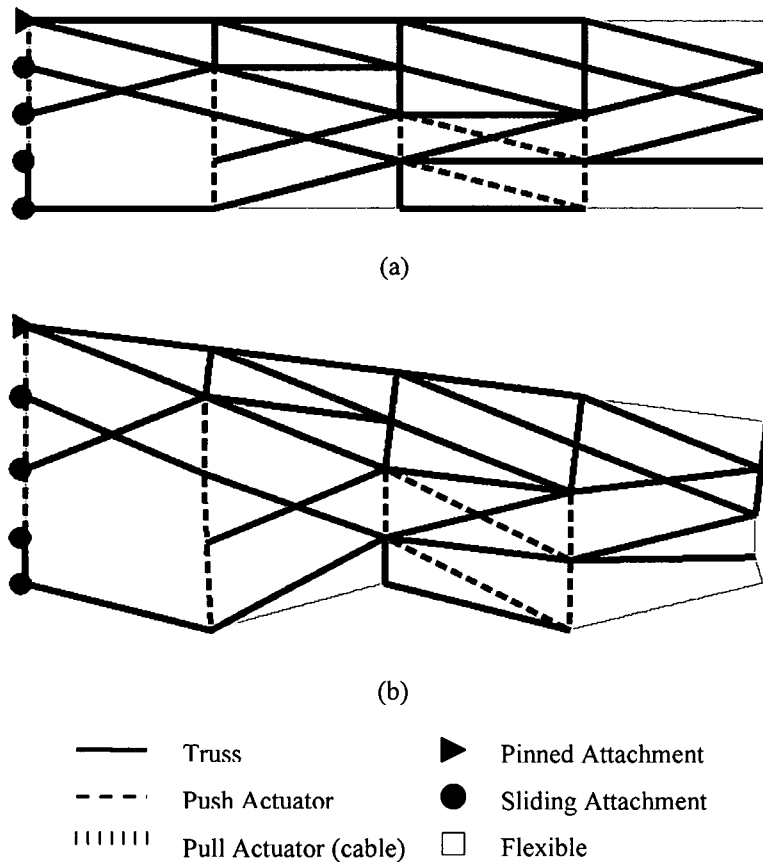
**Figure 18 Multiple Objective Problem (a) Position 1 (b) Position 2**

#### **4.8.2 Actuator Utilization Minimization with Shape Constraint Case**

Since the shape-matching is treated as constraints for this particular case, the problem essentially turns into the combination of constraint violation and actuator minimizations at initial iterations in the process. Therefore, this problem cannot be solved by optimization schemes that do not incorporate constraint violation measures. Since constraint violations are generally penalized severely, it is expected that the initial phase of the optimization process would be dominated by the constraint violation minimization. Consequently, the magnitude of constraint violation penalty may make a significant difference in the solution. Here, the initial condition is identical to that of the multi-objective case.

Figures 19a and 19b reveal that the shape objective has been met quite acceptably as in the last case. Although the normalized total shape error of 0.1589 is somewhat higher than the last case, the resultant shape seems acceptable. This shape error is explicable as the shape-matching is included in constraints with point-wise relaxation that allow each target point to have the maximum normalized displacement error of approximately 0.015. For that reason, one may notice that the fishtail effect at the wing tip is no longer corrected by an actuator as the formulation is essentially more tolerant of shape errors. Consequently, the total absolute actuator utilization value is smaller for this case as the optimization process does not have to sacrifice large actuator utilization for the relatively insignificant shape accuracy. Additional computations has revealed that the actuator work ratio of multi-objective result to the present result is approximately 1.0 to 0.793, indicating that the present result is approximately 21 percent superior in terms of actuator work. Furthermore, structural topologies, as well as joint configurations, for both cases are fundamentally similar with rigid structures at the leading-edge. The attachment configuration has been determined to be the same as in the last case.

Despite the fact that the actuator minimization formulation has provided a superior result for this particular problem, it is not indicative that the formulation will work better for other problems. Certainly, one can imagine the situation where shape accuracy is significantly more critical than the amount of actuator utilization. Moreover, this formulation, as mentioned, has very large shape constraint violations at the initial phase of optimization process and it is often difficult to attain convergence.



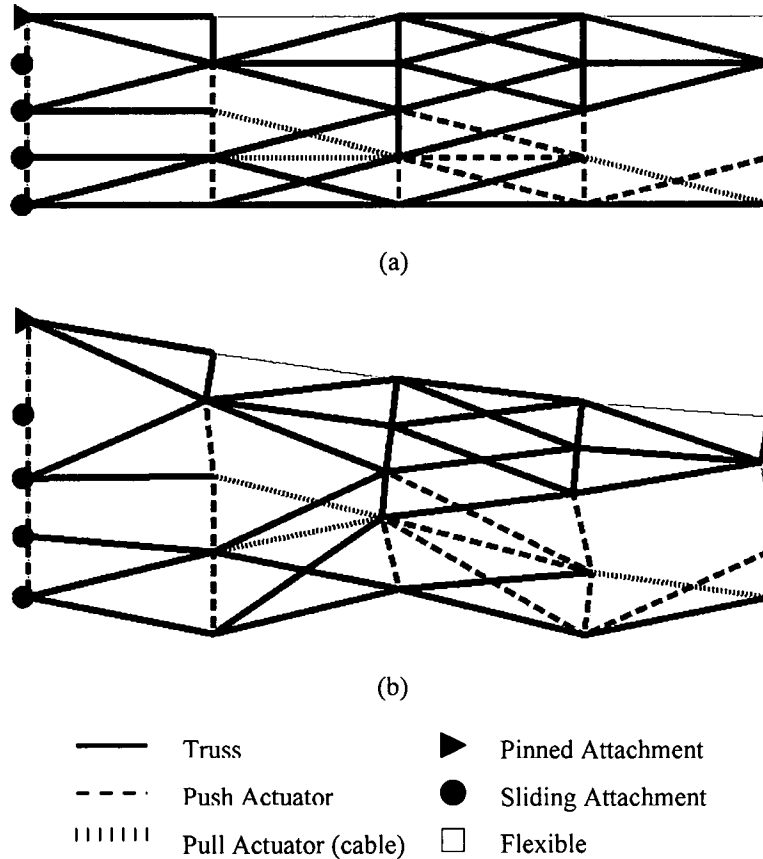
**Figure 19 Actuator Utilization Minimization Problem (a) Position 1 (b) Position 2**

### 4.8.3 Shape Error Minimization with Actuator Constraint Case

In this case, the assumption must be made that the desired actuator utilization value is known a priori. To facilitate the valid comparison, the total squared actuator value obtained from the previous case is applied to the problem. For instance, the multi-objective case provides the value of approximately 1.0. The problem is solved with the constraint to match this actuator parameter along with conditions identical to those of multi-objective case.

As one can observe from Figures 20a and 20b, the multi-objective case and the present case have provided strikingly similar results. This similarity may be plausible as

these two formulations share the similar objective and the optimizations have been performed with nearly identical conditions and parameters. The total absolute actuator utilization is 4.410, which is only fractionally different from that of multi-objective case. One may notice that the total absolute actuator value is different from that of multi-objective case, though both cases have the same total squared actuator utilization value. This is due to the difference in definition between “sum of squares” and “sum of absolute values.” In other words, the same total squared actuator utilization (sum of squares) does not necessarily imply the same total absolute actuator utilization (sum of absolute values). The total normalized shape error for the case is 0.0802, indicating that the shape objective has been met rather precisely. The work ratio of the multi-objective case to the present case is approximately 0.956 to 1.0, which can be considered as a negligible difference. Again, this is not a surprising conclusion as dominant actuators for both cases are positioned in similar locations to achieve the same shape change.

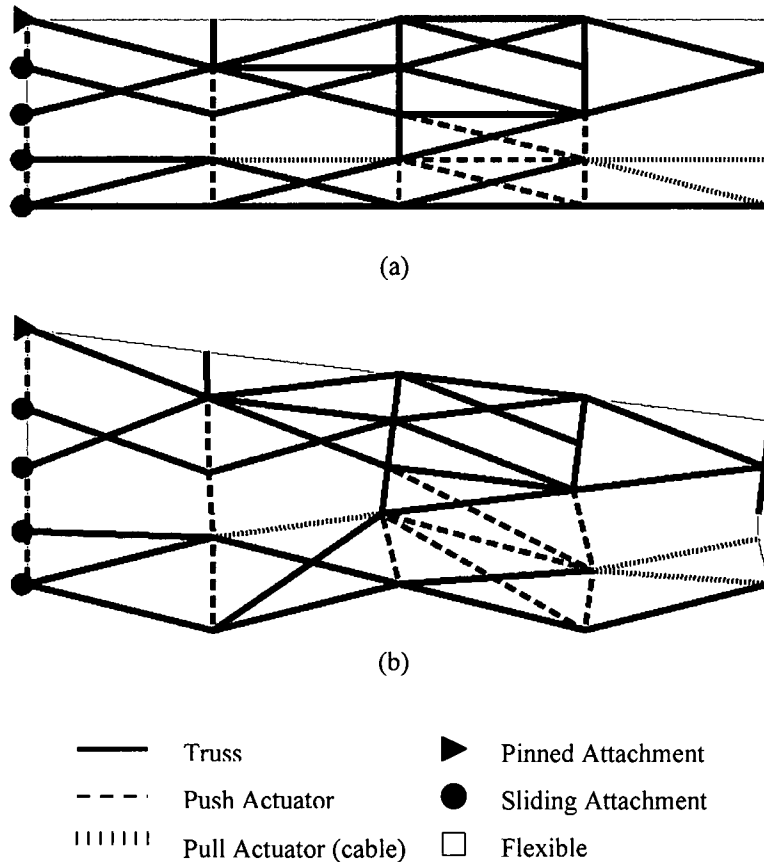


**Figure 20 Shape Error Minimization Problem (a) Position 1 (b) Position 2 for the Shape**

#### 4.8.4 Combinations of Formulations

In this section, the potential benefit of using a combination scheme has been demonstrated. The solution from multi-objective case is applied to the actuator minimization formulation. Figures 21a and 21b reveal that the actuator minimization reduces the actuator usage without changing the shape or the topology of the structure significantly. Otherwise stated, the actuator minimization followed by the solution of multi-objective case may result in a favorable “tightening” effect on the actuator utilization, assuming that the slight loss in the shape accuracy is not a major concern. The total normalized shape error is 0.1525 with the total absolute actuator utilization of

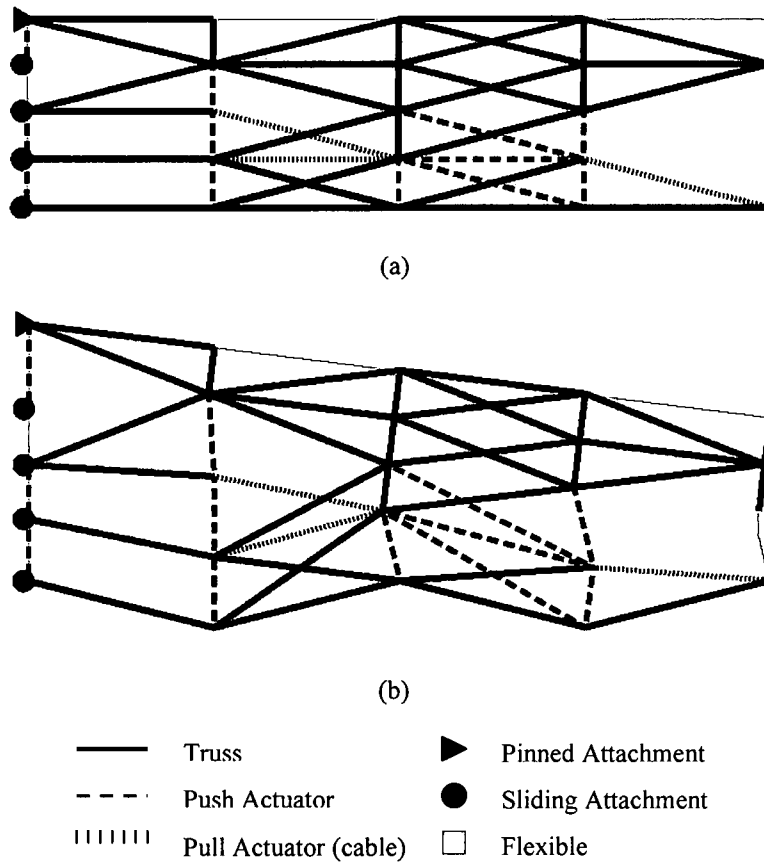
3.8198, indicating that the actuator requirement has been reduced at the expense of shape preciseness. The total actuator work is 13.34 percent less than that of the non-combination case. At the wing tip, the fishtail effect is clearly visible as the latter formulation is set to be more resilient to shape errors to reduce the actuator utilization.



**Figure 21 Combination of Multi-objective and Actuator Utilization Minimization Problems (a) Position 1 (b) Position 2**

The same process has been applied to the shape error minimization solution from section 3.3. Figures 22a and 22b illustrate the similar tightening effect as that of the previous case. The total normalized shape error and absolute actuator utilization are 0.1508 and 3.9103, respectively. The total actuator work has been reduced 13.09 percent

compared with the non-combination case. One may notice that an actuator to hold the fishtail effect has vanished and the fishtail effect is clearly visible for the same reason as the last case.



**Figure 22 Combination of Shape Error and Actuator Utilization Minimization Problems (a) Position 1 (b) Position 2**

#### 4.9 Conclusion

The results of the sample problem have revealed distinct characteristics of the presented formulations. The multiple objective formulation has provided a solution with acceptable actuator utilization and shape error values. It is observed that the formulation has a characteristic of minimizing both actuator utilization and shape error proportionally as defined by its objective weight constants. This formulation is ideal if both actuator

minimization and shape achievements are considered critical in the design. The actuator utilization minimization formulation has provided a solution with a less accurate shape and a superior actuator utilization value. It is noted that the actuator minimization formulation is beneficial if the precise shape target achievement is not as important as the actuator minimization. The combination scheme seems to possess an advantage in terms of solution controllability. The sequential solution of the shape or multiple objective formulations followed by the actuator formulation has the benefit of further minimizing the actuator utilization, provided that the shape errors within the defined shape boundaries are acceptable. The abovementioned differences in the characteristics of formulations may benefit one formulation from another in a certain problem. In other words, each formulation has its unique characteristics and it is premature to state which of these formulations works the best for any given instances. One must decide which formulation might provide the benefit to a particular problem according to design requirements.

Formulation \ Quantity	Push Actuator	Pull Actuator	Truss	Pin Attachment	Sliding Attachment
Multi-Objective	14	3	30	1	4
Actuator Minimize	11	0	33	1	4
Shape Error Minimize	14	3	33	1	4
Combination Multi-Objective/Actuator	12	3	32	1	4
Combination Shape Error/Actuator	12	3	33	1	4

**Table 1 A Comparison of Solutions from Various Problem Formulations**



## **CHAPTER 5**

### **MULTIPLE CONFIGURATION FORMULATION**

#### **5.1 Introduction**

The previous chapter demonstrated the potential capability of the topology optimization methodology for determination of distributed actuation systems for in-plane morphing structures. The chapters 3 and 4 presented the fundamental modeling concept, various topology optimization formulations, and solution procedures for a single configuration in-plane morphing wing structure with simulated flexible skin elements. Though the basic concept and formulations cover all the fundamental requirements of a morphing wing, the investigation still lacks the consideration to accommodate multiple shape changes that are one of the most ideal capabilities for a morphing air vehicle. Moreover, the earlier chapters introduced a novel approach in the design of morphing structures through an optimization technique, but the problem formulation is rather imprecise and did not contain clear definitions to accommodate more specific conditions that are applicable to morphing structures, such as reversibility and external load-dependent issues. Therefore, the primary emphasis of this chapter is to introduce improvement and extension of the concept and problem formulations developed for the single configuration case to those capable of accommodating multiple-configuration definitions.

## 5.2 Basic Multiple Configuration Problem Formulation

One important aspect that must be considered in the topology problem formulation with a multiple-configuration definition is that a single structure must be capable of satisfying multiple target shapes. That is, there should be no variation in structural components between one configuration to another. In such a problem formulation, the cost function will essentially be multi-objective. For instance, the weighted sum of shape error terms and actuator utilization terms can be minimized to allow simultaneous satisfaction of shape achievement and actuator placement:

$$\text{Minimize: } f_0(\rho) = \sum_i^{N_{shape}} \left[ W_S^{(i)} \sum_{j \in T_{gt}} (T_j^{(i)} - U(\rho)_j^{(i)})^2 \right] + \sum_i^{N_{shape}} \left[ W_A^{(i)} \sum_{j \in A_i} \rho_j \right] \quad (5.1)$$

The multi-objective function shown above contains shape error terms and actuator utilization terms for each target configuration. As in the single configuration case, topology design variables  $\rho$  control the stiffness of corresponding line, joint, attachment or actuator elements. The important point to note here is that the actual displacement vector for the  $i^{\text{th}}$  target configuration is independent of actuator loads that do not correspond to that particular configuration (i.e. each target configuration is satisfied by its own load set). In addition, the displacements for all configurations are a function of the same structural and joint design variables, thereby not allowing inter-configuration variation in structural topology. In the objective function, the perfect shape satisfaction is indicated when the difference between a target displacement ( $T_j^{(i)}$ ) and an actual displacement ( $U_j^{(i)}$ ) vanishes for all target degrees of freedom in every configuration. The square of each shape error term is necessary to ensure a positive quantity as optimization techniques in general can only accommodate either maximizing or

minimizing problem. The actuator utilization term is simply a summation of entire actuator variables in every configuration. The relative importance of shape and actuator terms is controlled by weight/scale constants,  $W_S^{(i)}$  and  $W_A^{(i)}$  respectively. The intuition points out that the shape objectives must dominate the problem, since the minimization of actuator utilization can be considered as a secondary or less significant objective. In other words, the shape satisfaction should be weighed much more than the actuator placement, since the solution is physically meaningless without a reasonable attainment of shape targets.

The topology optimization problem must include equilibrium constraints at multiple configurations. Therefore, the problem must contain a minimum of  $N_{shape}$  equilibrium conditions to be satisfied identically and simultaneously. If the shape morphing path must be generated, more than  $N_{shape}$  equilibriums along the path must be satisfied. In addition, the actuator definition is composed of  $N_{shape}$  load sets to represent different actuator loading conditions to attain  $N_{shape}$  configurations. As in the single configuration formulation, the line element stroke length must be constrained for all displacement sets, in order to avoid unrealistically large actuator or telescope stroke length. The corresponding topology optimization problem can be written in the standard Non-Linear Programming (NLP) form:

Minimize:

$$f_0(\rho) \tag{5.2}$$

Subject to:

$$\mathbf{S}^{(i)} = \mathbf{K}\mathbf{U}^{(i)} - \mathbf{F}^{(i)} = 0 \quad i = 1 \dots N_{shape} \tag{5.3}$$

$$f_m^{(i)} = E_m^{(i)2} - E_{\max}^{(i)2} \leq 0 \quad , \quad i = 1 \dots N_{shape} \quad m = 1 \dots N_L \tag{5.4}$$

$$\sum_{i \in L1} \rho_i - V_{\max 1} \leq 0 \quad (5.5)$$

$$\sum_{i \in L2} \rho_i - V_{\max 2} \leq 0 \quad (5.6)$$

$$\sum_{i \in L1} \rho_i + \sum_{i \in L2} \rho_i - V_{\max} \leq 0 \quad (5.7)$$

$$\sum_{j \in A_i} \rho_j - A_{\max}^{(i)} \leq 0 \quad (5.8)$$

$$\sum_{j \in A} \rho_j - A_{\max} \leq 0 \quad (5.9)$$

$$\sum_{i \in B} \rho_i - N_F \leq 0 \quad (5.10)$$

$$\rho_{\min} \leq \rho \leq 1.0 \quad (5.11)$$

where

$$K = \sum_{i \in J} (\rho_i^\beta K_i^{(R)} + K_i^{(NR)}) + \sum_{i \in L1} (\rho_i^p K_i^{(AX)}) + \sum_{i \in L2} (\rho_i^p K_i^{(NAX)}) + \sum_{i \in B} (\rho_i^\alpha K_i^{(S)} + K_i^{(NS)}) + K_{skin} \quad (5.12)$$

$$F^{(i)} = \sum_{j \in A_i} (\rho_j F^0) + F_{ext}^{(i)} \quad i = 1 \dots N_{shape} \quad (5.13)$$

The superscript  $i$  ranges from one to the total number of target configurations, denoting the multiple of conditions that must be satisfied simultaneously. The volume constraints (5.5)-(5.7) do not contain the superscript as there is no inter-configuration variation in the structural variables. Yet, the multiple expressions for a volume constraint indicate that the allowable volume of each structural component, as well as the total volume, should be constrained individually to prevent excessive utilization of a single component. One should also notice that the equilibrium equations (4.9) and (5.12) are identical, indicating that there is no physical variation in the analysis model used for both

single and multiple configuration formulations. The maximum actuator utilization values,  $A^{(i)}$  and  $A_T$ , limit the actual actuator utilization to the certain allowable values and are intra- and inter-position quantities, respectively. The attachment constraint is applied to limit the number of fixed attachments in a solution. Finally, side constraints are applied to design variables as in the standard topology optimization problem, where every design variables are allowed to vary from a small positive number,  $\rho_{min}$ , to a unity.

In the formulation, one may notice that actuator variables are unidirectional due to the positive value requirement placed by a side constraint (5.11), unlike bi-directional actuator variables used in the single configuration formulation. If the bi-directional characteristic of actuators is desired, a natural choice is to apply two opposing actuator variables to each potential actuator location. The contradiction in these coincident design variables should not be a concern as such a condition is seen as inefficient or expensive by the actuator utilization minimization term in the objective function. Another possible bi-directional implementation is to use squared actuator variables with negative lower bounds as in (4.8) of the single configuration formulation. Though the technique involves only a single actuator variable per actuator, the squared sum of actuator variables in the objective and/or constraint functions can possibly create artificial actuator distributions due to the false numerical advantage that the sum of products of fractions may present.

The objective function (5.1) can be reduced in terms by setting a set of weight constants to zero. As in the single configuration formulation case, other separate problem formulations can be devised: shape error and actuator utilization minimization formulations. For instance, the problem can be solved using only shape objective by

setting actuator weights to zero. This shape error minimization problem can be solved by specifying the desired value of actuator utilization as a constraint. As mentioned previously, the primary disadvantage of this formulation is that the desired value of actuator utilization for each configuration must be known *a priori*, while these utilization values are often difficult to predict. Additionally, since the actuator variables are not minimized in this case, opposing-coinciding actuator variables may become coexistent if the maximum actuator utilization values are improperly assigned. Since it is especially difficult to predict actuator utilization values for a multiple configuration problem, the shape error minimization formulation is not a good choice.

The actuator minimization problem results when weighting factors for the shape terms are set to zero. For this case, one may apply the following shape constraint in addition to (5.3)-(5.11):

$$\left(T_j^{(i)} - U_j^{(i)}\right)^2 - \varepsilon_{\max}^2 \leq 0 \quad i = 1 \dots N_{shape}, j = 1 \dots N_{tgt} \quad (5.14)$$

This shape constraint defines target shapes by constraining the target degrees of freedom on the morphing boundary within a certain error  $\varepsilon_{\max}$ . In other words, the target shape is defined using a constraint that effectively applies a “cage” or a target error limitation around each target point, although such a constraint generally creates a rather large constraint violation at the initial iteration in the optimization process. In order to avoid this large constraint violation, one may solve the shape error minimization problem first and then solve the actuator minimization problem. The potential benefit of such a sequential solution procedure is discussed in the previous chapter. In addition, one should remember that the constraint (5.14) introduces  $N_{shape}$  times  $N_{tgt}$  amount of constraints to be satisfied and therefore the problem may become excessively large and

complex for some optimization techniques to solve if the morphing boundary contains numerous target points. One should remember that the ability of an optimization technique to provide a converged solution is generally influenced by the problem size.

### 5.3 Sensitivity Analysis

The sensitivity analysis of the multiple configuration formulation is nearly identical to that of the single configuration formulation described in section 4.6. Therefore, only primary differences are highlighted in this section to avoid redundancies in content. The sensitivity of the objective function can be obtained analytically using the adjoint method, where the static equilibrium condition (5.12) is implicitly satisfied upon computation of sensitivities. The gradient of  $j^{\text{th}}$  degrees of freedom for  $i^{\text{th}}$  configuration can be written as,

$$U_j^{(i)} = I_j^T \mathbf{U}^{(i)} \quad i = 1 \dots N_{shape} \quad j = 1 \dots N_{tgt} \quad (5.15)$$

Since the formulation utilizes the same model as in the single configuration case,  $I_j$  is essentially identical to that of (4.19) and it is the unit vector defined by a displacement of  $j^{\text{th}}$  degree of freedom. As mentioned previously, one should note that, for each degree of freedom, there exist  $N_{shape}$  independent displacements. As in the single configuration case, one can add the residual of equilibrium equations (5.3) to the above equation as a zero term:

$$U_j^{(i)} = I_j^T \mathbf{U}^{(i)} - \mathbf{a}_j^{(i)T} (\mathbf{K} \mathbf{U}^{(i)} - \mathbf{F}^{(i)}) \quad (5.16)$$

Notice that the zero term is subtracted from (5.15) instead of an addition as demonstrated in the single configuration case. These differences in signs will not cause any problems

as long as signs are consistent in the analysis. The gradient of (5.16) with respect to design variables can be written as follows:

$$\frac{\partial U_j^{(i)}}{\partial \rho_e} = I_j^T \frac{\partial \mathbf{U}^{(i)}}{\partial \rho_e} - \mathbf{a}_j^{(i)T} \frac{\partial \mathbf{K}}{\partial \rho_e} \mathbf{U}^{(i)} - \mathbf{a}_j^{(i)T} \mathbf{K} \frac{\partial \mathbf{U}^{(i)}}{\partial \rho_e} + \mathbf{a}_j^{(i)T} \frac{\partial \mathbf{F}^{(i)}}{\partial \rho_e} \quad (5.17)$$

After collecting the gradient terms and rearranging, one can obtain the adjoint problem:

$$\mathbf{K} \mathbf{a}_j^{(i)} = I_j \quad (5.18)$$

Notice that index  $i$  is irrelevant in (5.18), indicating that the solution of adjoint problem is identical for each configuration:

$$\mathbf{a}_j^{(i)} = \mathbf{a}_j \quad (5.19)$$

and,

$$\mathbf{K} \mathbf{a}_j = I_j \quad (5.20)$$

After canceling out zero terms and applying the solution of adjoint problem (5.20), the gradient (5.17) can be written in more compact form:

$$\frac{\partial U_j^{(i)}}{\partial \rho_e} = -\mathbf{a}_j^{(i)T} \frac{\partial \mathbf{K}}{\partial \rho_e} \mathbf{U}^{(i)} + \mathbf{a}_j^{(i)T} \frac{\partial \mathbf{F}^{(i)}}{\partial \rho_e} \quad (5.21)$$

The gradient of objective function (5.1) with respect to structural design variables can be written as,

$$\frac{\partial f_0}{\partial \rho_e} = -2 \sum_i^{N_{shape}} \left[ W_S^{(i)} \sum_{j \in T_{gt}} \left( \Delta T_j^{(i)} \frac{\partial U_j^{(i)}}{\partial \rho_e} \right) \right] \quad e \notin A_k \quad (5.22)$$

The gradient with respect to actuator design variables can be written as,

$$\frac{\partial f_0}{\partial \rho_e} = -2 W_S^{(i)} \sum_{j \in T_{gt}} \left( \Delta T_j^{(i)} \frac{\partial U_j^{(i)}}{\partial \rho_e} \right) + W_A^{(i)} \quad e \in A_i \quad (5.23)$$

where



$$\Delta T_j^{(i)} = T_j^{(i)} - U_j^{(i)} \quad (5.24)$$

By applying (5.21) to (5.22) and (5.23), one can obtain the following objective sensitivity:

$$\frac{\partial f_0}{\partial \rho_e} = 2 \sum_{i=1}^{N_{shape}} \left[ W_s^{(i)} \sum_{j \in T_{gt}} \left( \Delta T_j^{(i)} \mathbf{a}_j^T \frac{\partial K}{\partial \rho_e} \mathbf{U}^{(i)} \right) \right] \quad e \notin A_k \quad (5.25)$$

$$\frac{\partial f_0}{\partial \rho_e} = -2 W_s^{(i)} \sum_{j \in T_{gt}} \left[ \Delta T_j^{(i)} \mathbf{a}_j^T \frac{\partial F^{(i)}}{\partial \rho_e} \right] + W_A^{(i)} \quad e \in A_i \quad (5.26)$$

The gradient of stiffness matrix and force vector can be obtained easily as demonstrated in the single configuration case. The sensitivities of stroke limit constraint (5.4) can also be obtained analytically. One can express the stroke length of a line element in its axial direction as,

$$E_m^{(i)} = \Psi_m^T \mathbf{U}^{(i)} \quad (5.27)$$

where  $\Psi_m$  is the rotational transformation vector that defines the degrees of freedom and orientation of  $m^{\text{th}}$  line element and was introduced previously in (4.29). Using the adjoint procedure, one can obtain the following equation:

$$E_m^{(i)} = \Psi_m^T \mathbf{U}^{(i)} - \Lambda_m (\mathbf{K} \mathbf{U}^{(i)} - \mathbf{F}^{(i)}) \quad (5.28)$$

By following the same procedure as the objective function sensitivity, the following line stroke sensitivity can be obtained:

$$\frac{\partial E_m^{(i)}}{\partial \rho_e} = -\Lambda_m^T \frac{\partial K}{\partial \rho_e} \mathbf{U}^{(i)} + \Lambda_m^T \frac{\partial F^{(i)}}{\partial \rho_e} \quad (5.29)$$

where  $\Lambda_m$  is the solution of the adjoint problem:

$$\mathbf{K} \Lambda_m = \Psi_m \quad (5.29)$$

The gradient of (5.4) is written simply as,

$$\frac{\partial f_m^{(i)}}{\partial \rho_e} = 2E_m^{(i)} \frac{\partial E_m^{(i)}}{\partial \rho_e} \quad (5.30)$$

By applying (5.29) into (5.30), the following stroke limit constraint sensitivity can be obtained. For structural design variables,

$$\frac{\partial f_m^{(i)}}{\partial \rho_e} = -2\Psi_m^T \mathbf{U}^{(i)} \Lambda_m^T \frac{\partial \mathbf{K}}{\partial \rho_e} \mathbf{U}^{(i)} \quad e \notin A_k \quad (5.30)$$

and, for actuator design variables,

$$\frac{\partial f_m^{(i)}}{\partial \rho_e} = 2\Psi_m^T \mathbf{U}^{(i)} \Lambda_m^T \frac{\partial \mathbf{F}^{(i)}}{\partial \rho_e} \quad e \in A_i \quad (5.31)$$

For the actuator utilization minimization problem, the sensitivity of shape constraint (5.14) must also be obtained. Since the first term of the multi-objective function (5.1) is essentially the same as the shape constraint, the sensitivity will be identical to (5.25) for the structural variables and (5.26) without the second term for the one that corresponds to actuator variables. The sensitivities for other constraints (5.5)-(5.10) are straight-forward and contain only ones and zeros.

#### 5.4 Effect of Weight Constants

The objective function (5.1) contains multiple terms to simultaneously minimize shape error and actuator utilization for every configuration. One must note that the solution may be significantly influenced by a balance between shape error and actuator weight/scale constants,  $W_S^{(i)}$  and  $W_A^{(i)}$ . Therefore, it is imperative to analyze and understand the effect of these constants. The choice of these weight constants must result from a comparison of the initial shape error and actuator utilization values. Suppose the objective is to achieve a shape-matching of a single point and if the shape error term is

scaled to 100.0 for the initial shape error function value of 100.0 units (i.e. 10 units of displacement error), the total actuator utilization that is scaled to 10.0 may cause the optimization process to be less capable of attaining a shape accuracy better than 1.0 unit of displacement error. That is apparent as the actuator and shape-error terms must find a compromise at some point in the process according to the proportion of these constants. Consequently, the convergence criterion is dependent on these factors.

### 5.5 External-load Dependency and Reversibility

The solution of the basic formulation above is external load-dependent and therefore special attention should be given to the effect of external loads. The external load dependency is evident since the displacement of a structure at target points will be dependent on applied external-loads and the resulting displacements will not be the same if the loads vary or completely vanish:

$$U_j(\boldsymbol{\rho}, \boldsymbol{\rho}_A, \mathbf{F}_{ext}) \neq U_j^*(\boldsymbol{\rho}, \boldsymbol{\rho}_A) \quad (5.32)$$

where  $\boldsymbol{\rho}$  and  $\boldsymbol{\rho}_A$  are the structural and actuator partitions of design variables, respectively. The ideal scenario may permit actuator variables to be varied to allow the structure to morph into desired configurations precisely as in (5.33), though neither reliability nor feasibility can be assured:

$$U_j(\boldsymbol{\rho}, \boldsymbol{\rho}_A, \mathbf{F}_{ext}) = U_j^*(\boldsymbol{\rho}, \boldsymbol{\rho}_A^*) \quad (5.33)$$

The load dependency of the solution is clearly undesirable if the structure is to be capable of morphing independently of external loads (for example, morphing when the vehicle is on the ground). Although one may argue that the solution should be obtained without applied external loads to eliminate the load dependency issue, a consideration of

such external loads in the problem is indeed essential. These external loads provide a desirable problem definition that encourages structures, along with actuators, to have a capability to work against the loads. Additionally, actuation energy can possibly be extracted from the applied external loads if they are considered in the problem. Such an energy extraction is certainly ideal as its characterization may parallel the energy extraction from an air-stream. In order to deal with abovementioned problem characteristics, external load independency strategies must be developed.

As the external load independency and reversibility are essential characteristics of morphing structures, the basic formulation must be modified to address these issues. In addition, there must be a requirement that the reversible structure must be stiff enough to work against external loads. The method devised in this investigation involves the introduction of an artificially-defined condition that encourages the initial or reference configuration, which is one of the target configurations, to be held rigidly, thereby providing the structure with ability to work against the external loads using few artificially-placed actuators at the wing root. These actuators are determined through the optimization process and, by reversing the actuation direction, possess the ability to “mimic” the external loads in case these loads are diminished or vanished:

$$U_j(\rho, \rho_A, F_{ext}) = U_j^*(\rho, F^*(\rho_{artificial}^*)) \quad (5.34)$$

where  $\rho_{artificial}$  is the control parameter that determines the utilization of artificially-placed actuators and the asterisk (\*) denotes the reversed actuation direction. The above condition can be replicated when the objective function below approaches zero, indicating no displacements at the morphing boundary for the reference configuration:

$$\text{Minimize: } f_{0R}(\rho) = \sum_{j \in Tgt} (U(\rho, \rho_{artificial}, F_{ext})_j^{(1)})^2 \quad (5.35)$$

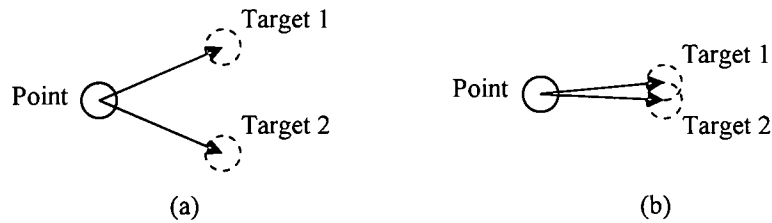
The objective function (5.35) replaces the first or reference shape term in the original objective function (5.1). Although one may argue that the objective above is nearly identical to that of the original shape term, the introduction of (5.35) provides a more distinct problem definition that the external loads must be handled via rigid structures using few actuators at the wing root. The sensitivity of this objective term can be obtained in the same fashion as the original formulation and is similar to that of the shape term in (5.1), where target displacements are assigned to be zero in this case.

The reference configuration should be chosen according to the design requirement. The reasonable choice is to select the most essential configuration to be the reference. For instance, if the vehicle is to be designed to spend most of its mission duration in a certain configuration, that particular configuration should be chosen to be the reference. Though such a selection technique is certainly not a requirement, it makes the best sense as such a reference implies the resting shape of a morphing structure and, consequently, indicate that compliant components in the structure carry the least amount of strain at that configuration.

## **5.6 Actuator Distribution Control**

The second term in the multi-objective function (5.1) represents the actuator utilization of the system. This actuator utilization is simply the sum of all actuator variables for every configuration, which is equivalent to the sum of actuator forces in the system. Though this expression of actuator utilization may be sufficient for a two-configuration system that only requires two actuator load sets, it is impractical for a multiple-configuration case due to its distribution characteristics. A simple explanation can be devised from Figure 23. Suppose there is a point and it must be delivered to two

separate locations as shown in Figure 23a, the best and most efficient way, in terms of actuator utilization in (5.1), is to use multiple force vectors that are aligned closely with the directions of motion. In fact, such an actuator distribution is probably necessary if the targets are sufficiently apart. Alternatively, if the targets are located in the close proximity (Figure 23b), the optimization shall still favor an actuator distribution for the same reason, as the optimization process tries to minimize the utilization without any consideration of the quantity of actuator locations. Although the resulting distributed actuation may be the most efficient form, excessive distribution is generally not desirable in the physical context. Therefore, the basic formulation must be modified to accommodate the actuator distribution control.



**Figure 23 Actuator Distribution Characteristics: (a) Far apart targets; (b) Close targets**

Among several methods that can be devised to control actuator distribution, the one studied in this investigation involves a modification to the actuator term in the objective function (5.1):

$$\text{Minimize: } f_{0A} = W_{A1}f_{A1} + W_{A2}f_{A2} \quad (5.36)$$

where  $f_{A1}$  is the actuator utilization term from the original formulation (5.1),  $f_{A2}$  is the actuator distribution control term. The actuator distribution term is there to maximize the concentration of inter-configuration actuator variables in a single physical location, which can be expressed as the following maximizing problem:

$$\text{Maximize: } f_{A2+} = \sum_{i=1}^{N_{\Omega}} \left( \prod_{j \in \Omega_i} \rho_j \right) \quad (5.37)$$

where  $\Omega_i$  is the set of actuator variables at  $i^{\text{th}}$  physical location and  $N_{\Omega}$  is the maximum number of physical locations available for actuators to occupy. In order to solve this maximizing problem in the minimization form of (5.36), one well-known technique is a weighted summation form that adds a negative of the maximizing term,  $f_{A2+}$ , to the minimizing problem:

$$\text{Minimize: } f_{0A} = \sum_{i=1}^{N_{\text{shape}}} \left( W_{A1}^{(i)} \sum_{j \in A_i} \rho_j \right) - W_{A2} \sum_{i=1}^{N_{\Omega}} \left( \prod_{j \in \Omega_i} \rho_j \right) \quad (5.38)$$

This actuator objective function replaces an actuator minimization term in the original objective function (5.1). The proportion of weight constants,  $W_{A1}^{(i)}$  and  $W_{A2}$  determines the magnitude of actuator distribution or concentration. One must remember that the actuator distribution control term may cause an opposing effect on the actuator utilization term if it is weighted excessively. Therefore, careful consideration should be given upon choosing a weight proportion.

Another possible way to treat such contradictory terms is to use a ratio form, where minimizing and maximizing terms are placed on numerator and denominator, respectively:

$$\text{Minimize: } f_{0A} = \frac{\sum_{i=1}^{N_{\text{shape}}} \left( W_{A1}^{(i)} \sum_{j \in A_i} \rho_j \right)}{\sum_{i=1}^{N_{\Omega}} \left( \prod_{j \in \Omega_i} \rho_j \right)} \quad (5.39)$$

The primary disadvantage of the ratio form is that the balance between actuator distribution and utilization cannot be controlled as the weight proportion is irrelevant for

this case. Therefore, the weighted summation form (5.38) is the preferred technique in this research.

### 5.7 Modified Relative Volume Constraint

The relative volume constraint (5.7) in the basic formulation is a simple sum of line variables and does not represent the physical volume that can be occupied by line elements. This imprecise volume definition is primarily due to the multiple structural design variables that are assigned to a line element in any particular location. More specifically, the root of this ill-defined volume comes from two design variables for a line element that separately control axial and bending stiffness (i.e.  $L1$  and  $L2$  set of variables). A frame element that expends two units of volume, instead of a unit volume for a truss or telescoping element, will likely be disfavored by the optimization process. Consequently, the ideal volume definition for such a case, therefore, should be based on the physical existence of a line element, instead of the total quantity of line variables.

In order to accomplish such a task, the volume constraint can be modified to count a single unit of volume for each line element, regardless of whether it is a frame, a truss, or a telescope:

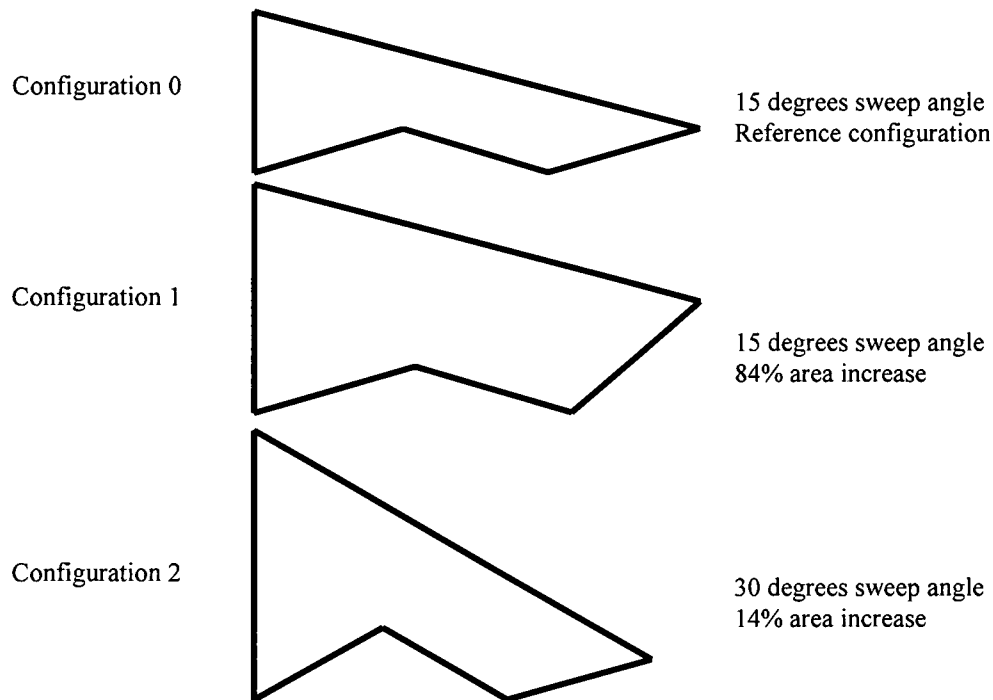
$$f_v = \sum_{i \in L1} \rho_i + \sum_{i \in L2} \rho_i - \sum_{i=1}^{N_\Phi} \left( \prod_{j \in \Phi_i} \rho_j \right) - V_{\max} \leq 0 \quad (5.40)$$

where  $\Phi_i$  is the set of structural variables at the  $i^{\text{th}}$  physical location and  $N_\Phi$  corresponds to the number of available physical locations that line elements can occupy. The volume constraint above enhances the volume definition as the sum of products term ensures that the frame usage is unbiased. One may also notice that the volume constraint becomes analogous to OR-logic as the solution approaches 0-1 design.



## 5.8 Three-configuration Example Problem and Results

The example problem provided here involves a three-configuration morphing wing design, including loiter (surveillance), high-lift (landing), and climb (takeoff) configurations as shown in Figure 24. The problem portrays the generic surveillance UAV mission that requires the majority of its flight time in a loiter configuration. Therefore, configuration 0 or the reference configuration should be the loiter configuration that must be held rigidly using a minimum amount of artificial actuators at the wing root section. Configuration 1 is the high-lift configuration with a large wing planform area increase of approximately 84 percent. One should notice that the motion between configurations 0 and 1 is solely an area expansion and does not involve any sweeping motions. The third configuration is the climb configuration and has 30 degrees (i.e. 15 degrees with respect to the reference) sweep with a slight area increase of 14 percent. For the entire target shapes, the leading-edge length remains the constant, implying that the leading-edge must make a rigid-body rotation around the wing root. Although such a problem definition fixes the optimization solution in the manner equivalent to the pre-assignment of a leading-edge spar, the explicit definition of the structural components is avoided in the investigation to observe the characteristics of the problem formulation.

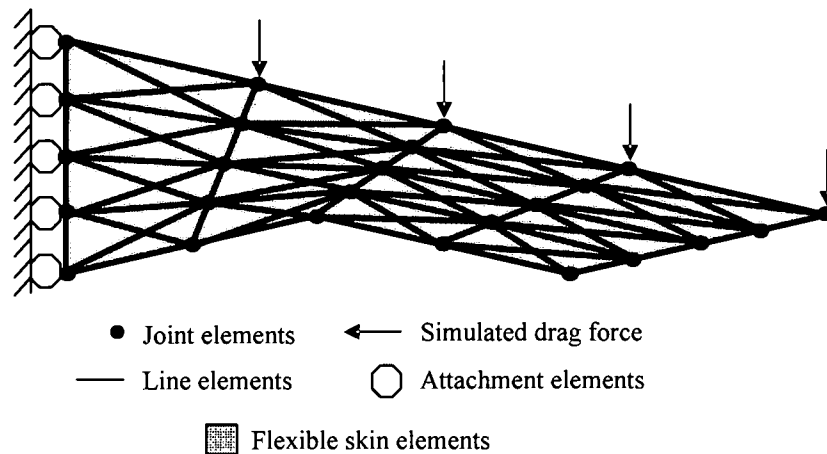


**Figure 24 Example Problem Description**

The semi-ground structure with 4 x 4 cells, as shown in Figure 25, with evenly distributed initial design variables is selected to be the starting point in the optimization process. The structure has 72 line elements with definitions that each location can be occupied by frame, truss, telescope, or actuator elements. Among these line elements, there are 64 potential locations with 262 design variables for actuators and active telescopes. In addition, the model contains 144 joint elements and 5 potential fuselage attachments. Overall, the problem contains 555 design variables. The problem is solved using the globally convergent version of Method of Moving Asymptotes (GCMMA) developed by Svanberg [27,28].

The physical dimensions of the wing are also selected to simulate the generic UAV. The reference configuration has a wingspan of 10 feet. The physical and material properties of the full frame element are chosen to resemble a frame with 1 inch x 1 inch

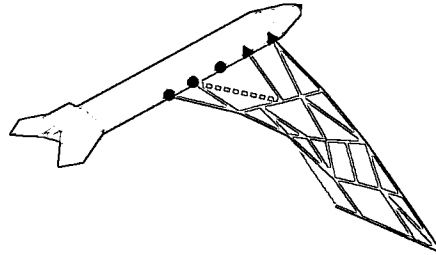
square cross-section that is made of common aluminum alloy. The beam and truss elements are the decomposition of a full-frame structure with the same physical and material properties. The maximum allowable actuator force per actuator is set to 1000 pounds. In order to simulate the in-plane drag loads experienced during the flight, nodal forces of 100 pounds are applied to four leading edge locations as shown in Figure 1(a). The element stroke limit is set to 15 inches, regardless of its original length. The skin element has small membrane stiffness, yet it provides some resistance to relative motions and itself does not act as a load-bearing structure.



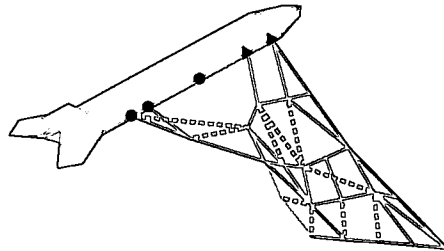
**Figure 25 Semi-ground Structure for the Example Problem**

### 5.8.1 Base Solution

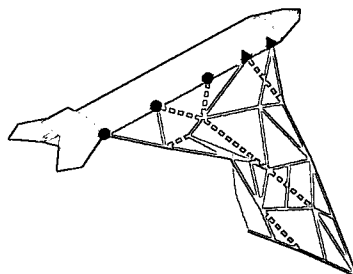
The solution shown in Figure 26 is regarded as the base solution since no actuator distribution control and modified volume control measures are applied to the problem. The total normalized shape error for the case is 0.1216, indicating that approximately 88 percent of the desired total target displacement was met. The highest actuator utilization value (i.e. sum of actuator variables for a configuration) of 5.5367 has been observed in



(a)



(b)



(c)

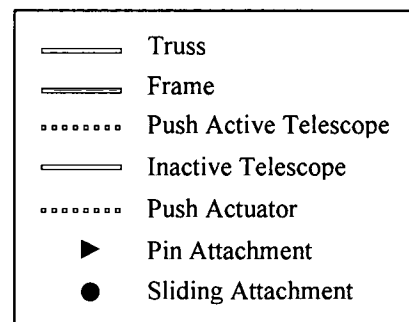


Figure 26 Base Solution: (a) Configuration 0 (b) Configuration 1 (c) Configuration 2

configuration 1. The maximum useful actuator work value, which occurs in the configuration, is 30619 in-lbs. The number represents the peak actuator energy in transition to the strain energy in flexible skin, compliant joints, and residual compliant members and it probably can be regarded as an indication of how compliant or articulate the structure/mechanism might be.

One may notice that structural components in the solution are dominantly truss elements with 22 trusses, 7 inactive telescopes, and only 2 frames. As explained previously, this truss-dominant solution may be a resultant of the biased volume definition in (5.7). The leading edge section has a rather concentrated formation of truss elements, indicating that the spar is required to resist the simulated drag loads. The structure is mainly composed of a spar at the leading edge and combination of linkages in various orientations. The spar formation is connected to a fuselage through a pin joint, while other attachments along the wing root are sliding connections. The inactive telescopes are more prevalent in the trailing-edge section. This is probably due to the change in length of the trailing-edge as the structure moves from one configuration to another.

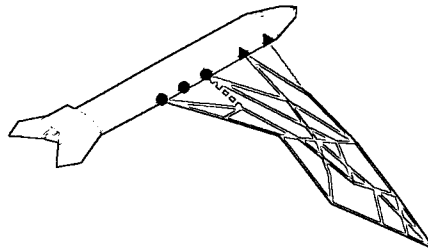
Following the reversibility and external load independency definition in the problem formulation, the optimization has determined an appropriate artificial actuator to hold the reference configuration rigidly against the simulated drag loads, as clearly indicated in Figure 26a. Configuration 1 has 8 active actuators and 2 active telescopes. Configuration 2 has 9 active actuators and an active telescope. The total number of actuator locations in the solution is 16 and they appear to be excessively distributed. In addition, it is clearly evident that sweeping motion and root section shape is controlled

mainly at the wing root section with actuators through a mechanism that somewhat resembles a four-bar-linkage. The local shape changes seem to be accomplished by combination of rectangular-shaped linkages along with corresponding distributed actuators that are placed across the wing.

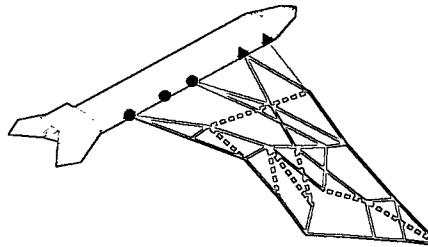
### **5.8.2 Solution with Modified Volume Constraints**

The solution shown in Figure 27 has resulted from the problem with all the same parameters and conditions as in the previous case, but it has the modified volume constraint definition that does not bias frame usage. The normalized total shape error is 0.0972, which is slightly better than that of the previous case. The maximum actuator utilization value of 5.4479 occurs in configuration 1 and the corresponding maximum useful actuator work is 30919 in-lbs, indicating the similarities between the current and previous cases in the actuation energy requirement and the structural compliance. Although the topology may appear significantly different from that of the previous case, close examinations and comparisons reveal that the fundamental characteristics and kinematics of the structures are nearly identical.

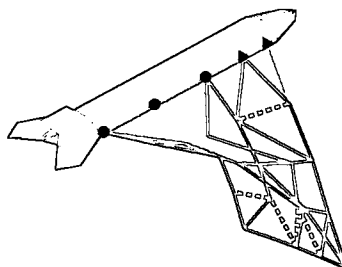
In the figure, the expected effect of the modified volume constraint can be observed. It is clearly visible that the amount of frame in the solution has been increased as compared with the previous solution. The structural partition of the solution is composed of 12 trusses, 6 frames, and 13 inactive telescopes. For the same reason as the previous case, the optimization process creates a spar-like structure at the leading-edge that is connected to the fuselage through a pin joint. One may notice the absence of a line element at the leading edge at the root and that the load-bearing structure is connected to the second pin joint instead of the first one. This is reasonable, since the model does not



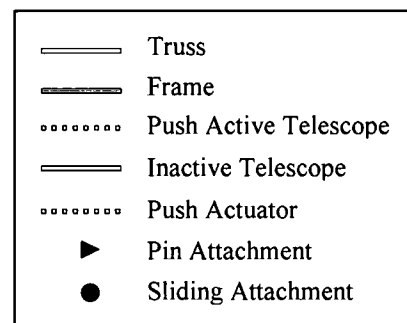
(a)



(b)



(c)



**Figure 27 Solution with Modified Volume Constraint: (a) Configuration 0 (b) Configuration 1 (c) Configuration 2**

contain a simulated drag load at the root and an independent fixed joint at the leading edge is more than capable of holding the flexible skin in position.

Similarly to the previous case, the structure attains its local motions through a combination of linkages, along with corresponding actuators placed along the entire span. Overall, there are 3 active telescope and 14 actuator locations. The configuration 1 utilizes 5 active actuators and 3 active telescopes. The configuration 2 has 5 active actuators and no active telescopes. Additionally, it is worthwhile to point out that the position of active actuator and active telescopes are the only inter-configuration variations and the structural topology remains the constant over the entire configuration, as clearly indicated in the figures.

### **5.8.3 Actuator Distribution Controlled Solution with Modified Volume Constraint**

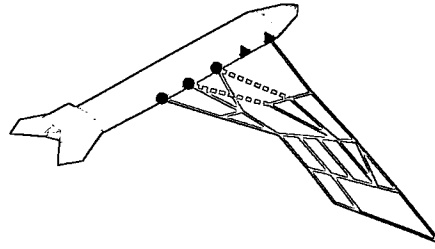
Although the distributed actuation system is often considered to be energy efficient, the excessive distribution of active elements (i.e. actuators and active telescopes) is physically impractical for numerous reasons. In fact, the actuator distribution in Figure 26 and 27 seems rather excessive. In order to promote the concentration of actuation forces at fewer locations, the actuator distribution control strategy in (5.38) is applied to the problem that is identical in definitions and conditions to the previous cases.

The solution in Figure 28 shows the favorable effect of the actuator distribution control. The total number of active element locations for the case is 8 (5 actuator and 3 active telescope locations), which is dramatically less than that of the previous cases. The total normalized shape error of 0.1807 and the maximum actuator utilization of 5.2152 have been observed. Though the actuator utilization has improved, the shape

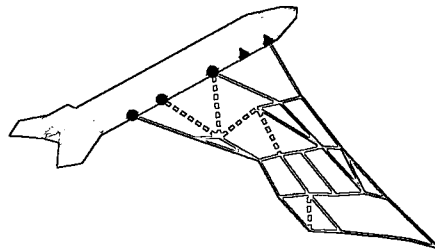


accuracy has decreased to approximately 82 percent. The outcome is somewhat explicable as the optimization has to compromise the shape objective to achieve the solution with lesser actuator locations. The structural components in the solution are composed of 16 trusses, 11 frames, and 5 inactive telescopes. Furthermore, the clear distinction between the load-bearing frame structure at the leading-edge and the rectangular mechanisms can be made from the figure. The active components are 5 actuators and 3 active telescopes with the maximum useful actuator work value of 27154 in-lbs. Among these locations, configuration 1 utilizes 4 active actuators and 2 active telescopes. Configuration 2 has 5 active actuators and an active telescope.

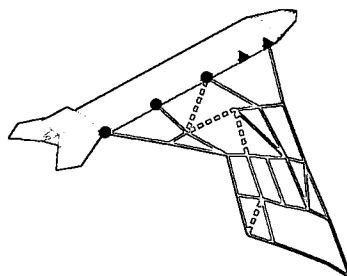
The actuator distribution control parameter can be further increased to possibly allow the solution with lesser actuator distributions. The solution in Figure 29 has 7 actuator locations with the higher distribution parameter. That is not a significant reduction, but one may hypothesize that the amount of actuator distribution is necessary to meet the reasonable shape-match objective value. The shape objective is generally weighted much heavier than the actuator objective, since it is the primary importance in the problem. For the structural part, there are 23 trusses, 6 frames, and 3 inactive telescopes. It is also noteworthy that the maximum actuator utilization of 5.0111 and the corresponding maximum usable work value of 21341 in-lbs has been observed. The lower utilization and work value may indicate that the solution employs less elastic motions, compared with the previous solutions. The total normalized shape error is 0.1775, which is similar to the one obtained in the lower distribution parameter case.



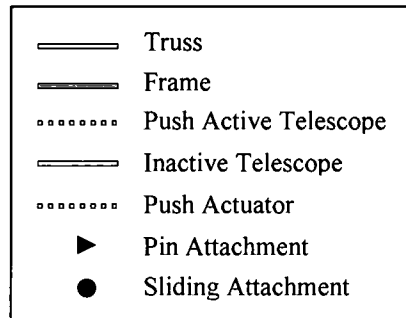
(a)



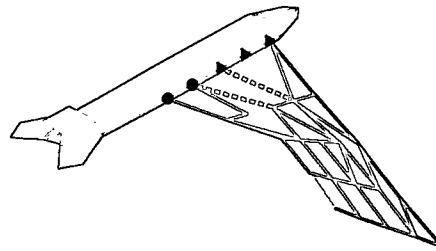
(b)



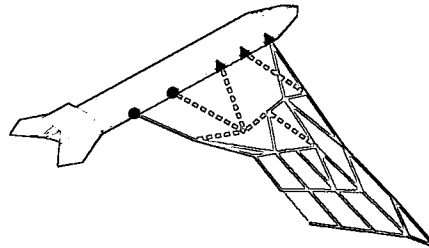
(c)



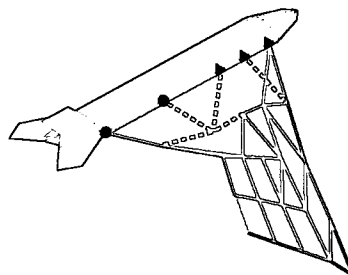
**Figure 28 Actuator Distribution Controlled Solution with Modified Volume Constraint: (a) Configuration 0 (b) Configuration 1 (c) Configuration 2**



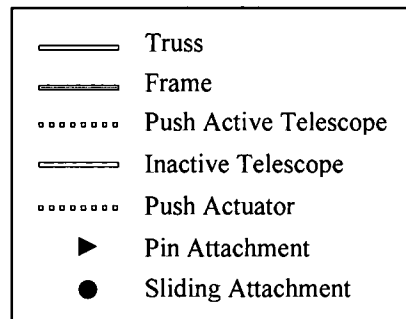
(a)



(b)



(c)



**Figure 29 Actuator Distribution Controlled Solution with Modified Volume Constraint and Higher Distribution Control Parameter: (a) Configuration 0 (b) Configuration 1 (c) Configuration 2**

## 5.9 Two-configuration Example and Results

In order to facilitate the valid comparison with the single-configuration formulation introduced in the previous chapter, the same example problem that is portrayed in section 4.8 is solved again to demonstrate the improvements and enhancements made to the problem formulation in this chapter. It is important to note here that the single configuration solution from the previous chapter does not have the definition of the reference configuration, reversibility, and external load independency. Therefore, the resulting morphing structure has no guarantee of reversing the position or being able to function without the external loads. Using the formulation introduced in this chapter, one should be able to obtain a superior solution with reversibility and external load independency, as discussed earlier in the chapter. One should note that the actuator distribution control may appear ineffective in this particular problem, since the strategy is specifically developed to benefit the problem with more than two configurations.

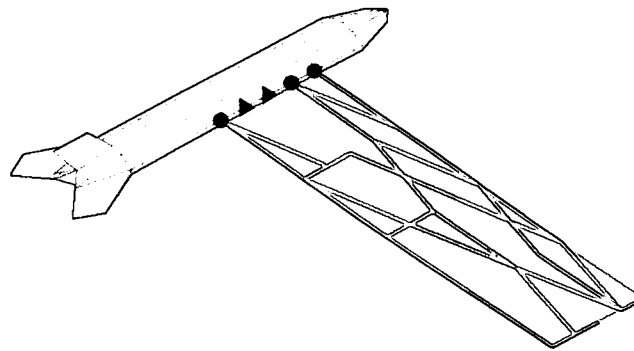
In this example, the reference configuration has been chosen to be the rectangular shaped wing shown in Figure 17. The new solution in Figure 30 reveals many similarities with the solution obtained in the previous chapter. One can observe a spar formation at the leading edge and a mechanism formation at the trailing edge section as seen before. There is also a concentration of actuators at the wing root section to cause a sweeping motion.

There are several improvements that can be observed. First, the truss dominance that was prevalent in solutions from the previous chapter is significantly reduced using the modified volume constraint. As expected, the effect of actuator distribution control is

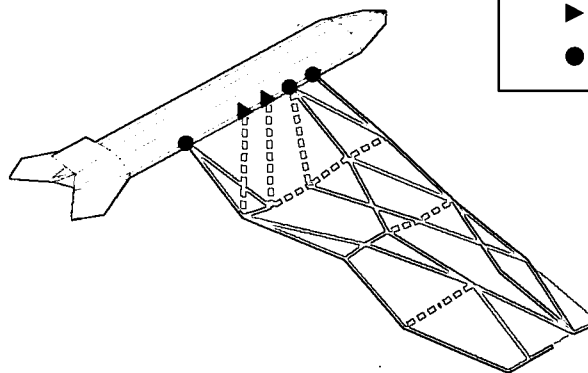
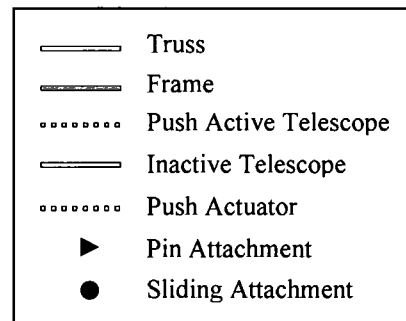
not readily visible as the definition of actuator distribution or concentration for this problem is somewhat irrelevant. However, the total amount of actuators has been reduced by the new actuator definition that does not contain any squared actuator terms in the objective or constraint function. One should also note that the solution from the new formulation is also reversible in position. It is interesting to observe that the reference configuration does not have a single reversing actuator. This indicates that the optimization has chosen a compliant structure for this particular problem. That is, the structure shown in the figure is spring loaded to the reference configuration by a series of compliant joints and actuators are used only to morph the structure (i.e. actuators are not used to maintain the reference configuration).

Quantity Formulation	Push Actuator	Pull Actuator	Active Telescope	Inactive Telescope	Truss	Frame	Pin/Fixed Attachment	Sliding Attachment
Multi-Objective (Old)	14	3	0	0	30	0	1	4
Actuator Minimize (Old)	11	0	0	0	33	0	1	4
Shape Error Minimize (Old)	14	3	0	0	33	0	1	4
Multiple Configuration (New)	9	0	1	3	15	13	2	3

**Table 2 Comparison of solutions: previous and new problem formulations**



(a)



(b)

**Figure 30** Solution of Two configuration example with modified volume constraints and actuator distribution control (a) reference (b) morphed configurations

## 5.10 Conclusion

In this chapter, several important modifications and enhancements have been made to the multi-objective formulation introduced in the previous chapter to accommodate multiple configuration definitions and other ideal characteristics of morphing structures. First, the basic formulation for the multiple configuration problem has been introduced. The actuator distribution control and modified volume constraints are subsequently applied to the formulation to improve the formulation quality, physical meaningfulness of the problem, and solution controllability.

The three configuration example problem has clearly revealed that actuator distribution control and modified volume strategies introduced in this chapter are effective and indeed improve the solution quality. The basic formulation has provided a truss-dominant structure with excessive actuator distributions. This truss-dominant solution is understandable as the original volume constraint has the tendency to bias frame usage. In order to reduce the truss dominance and encourage frame usage in the solution, the problem has been solved with modified volume constraints. The solution clearly shows that the modified volume constraints have a favorable effect of reducing the truss dominance, though slight distortions in structural topology are visible. In order to provide a more reliable solution, actuator distribution control is applied to the problem. The solution shows the dramatic improvement in both structural topology and actuator distribution. It is evident from the solution that the best solution can be obtained by applying both modified volume constraints and actuator distribution control. Further reduction in actuator distribution has been attempted, but the optimization does not respond to the tightened actuator distribution parameter. One can hypothesize that the

actuator concentration at that point has peaked and no further reduction in distribution can be made without sacrificing the shape objective. The table that summarizes the solutions of the example problem is shown in Table 3 below.

Formulation	Push Actuator	Pull Actuator	Active Telescope	Inactive Telescope	Truss	Frame	Pin/Fixed Attachment	Sliding Attachment
Basic Formulation	14	0	2	7	22	2	2	3
Modified Volume	11	0	3	13	12	6	2	3
Modified Vol. and Act. Dist. Control 1	5	0	3	5	16	11	2	3
Modified Vol. and Act. Dist. Control 2	4	0	3	3	23	6	3	2

**Table 3 Solution comparison for the three configuration example problem**

Finally, a comparison between the formulations from the last chapter and the current chapter has been made. The comparison clearly reveals that the formulation developed in this chapter is superior with reversibility and load independency definitions. In addition, similarities in solutions from new and old formulations have been discussed.



## **CHAPTER 6**

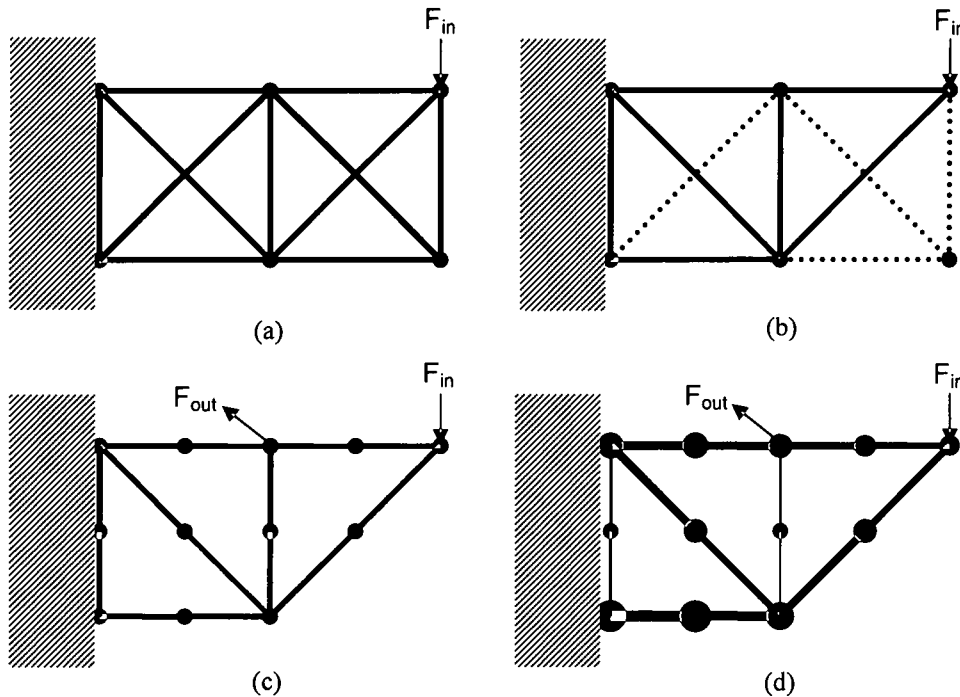
### **SIZE OPTIMIZATION**

#### **6.1 Introduction**

In order to provide a further realization, one may perform size optimization to apply dimensionality to the solution obtained from a topology process. Size optimization is an important part of design process because topology optimization is generally not capable of including stress constraints in the problem formulation. Therefore, the topology solution may contain structural members that are stressed beyond yield stress. It is essential to detect such over-stress conditions and correct the solution using size optimization. In this research, another purpose of size optimization is to ensure that the structure conceived by topology optimization is actually capable of withstanding out-of-plane aerodynamics loads. One should note that the strategy demonstrated in this chapter is an implementation of size optimization process to a morphing structure and therefore the material covered in this chapter should not be considered as a new study on theoretical details of size optimization.

The general approach to this multiple optimization process is portrayed in Figure 31. First, the topology synthesis is performed on the ground structure (Figure 31a), as explained in the earlier chapters. Figure 31b shows the representative topology solution with void elements (dotted lines are void elements). Then, the solution from topology

optimization is post-processed and applied to the sizing optimization as an input (Figure 31c). In the regenerated model, one can see the additional out-of-plane loading. The size optimization that minimizes the supplied objective function is then performed, as shown in Figure 31d, to determine the optimum cross sectional area of each line element, given an additional set of boundary conditions.

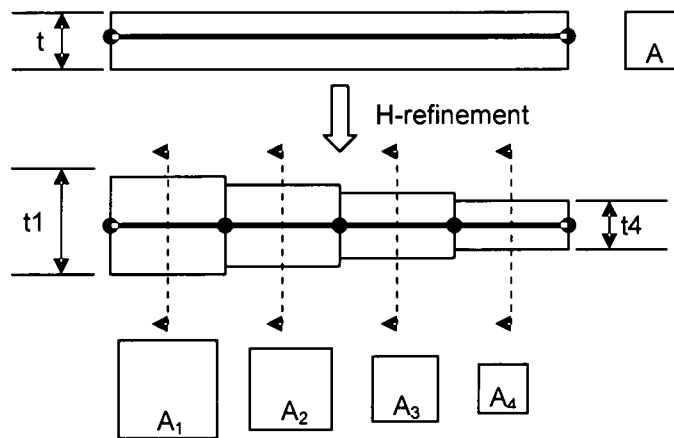


**Figure 31 Multiple Stage Optimization Process (a) Analysis model (b) Topology optimization solution (c) Analysis model regeneration (d) Size optimization solution**

## 6.2 Analysis Model Generation

The analysis model used in the size optimization is obtained from the topology synthesis process. The same model used for the topology synthesis should not be used for the sizing problem, since non-existent or void elements still retains its degrees of freedom and it is numerically inefficient to keep these elements. Therefore, the analysis model is reorganized and re-meshed to remove non-existent members and their degrees

of freedoms as shown in Figure 31c. Each existent line elements are also sub-sectioned to allow more precise sizing of element cross-sectional areas. By applying the sub-sections, one may be able to observe the geometric pattern of line elements, as shown in Figure 32. In addition to regeneration of the analysis model, it is necessary to apply the out-of-plane degrees of freedoms to the model. The flexible skin element that was previously represented by a 4-node membrane element is replaced with a 4-node Mindlin ( $C^0$ ) plate element to accommodate out-of-plane bending. The membrane stiffness of the plate is directly transferred from the topology solution and the bending stiffness is assigned an insignificant value to prevent the flexible skin from behaving as a load bearing structure.



**Figure 32 Line element sub-sectioning**

The aerodynamic loads for each configuration are obtained using a Vortex Lattice Method (VLM). The aerodynamic forces are translated to the structure using the infinite plate spline technique commonly employed in commercial analysis programs, such as NASTRAN and ASTROS [29,30]:

$$F_a = G^T P \quad (6.1)$$

where  $\mathbf{G}$  is the spline matrix. The force vector  $\mathbf{F}_a$  is the vector of aerodynamic forces translated to the structural degrees of freedom and the vector  $\mathbf{P}$  is the aerodynamic loads on aerodynamic panels. Figure 34 illustrates the spline technique.

In this research, aerodynamic influences from both of symmetric flying surfaces are considered, as shown in Figure 33. One may notice that wing tips in the aerodynamics model are straightened to preserve the numerical accuracy of VLM, while the wing area is kept constant to maintain geometric consistencies. In addition, the aerodynamic contribution of a non-morphing structure (i.e. fuselage and tail) is assumed to be insignificant. One should also note that the out-of-plane aerodynamic load obtained from VLM is used only for the sizing problem and applied to each configuration in quasi-steady manner. In future investigations, simultaneous topology and sizing problem should be solved with fully coupled aeroelastic equilibrium.

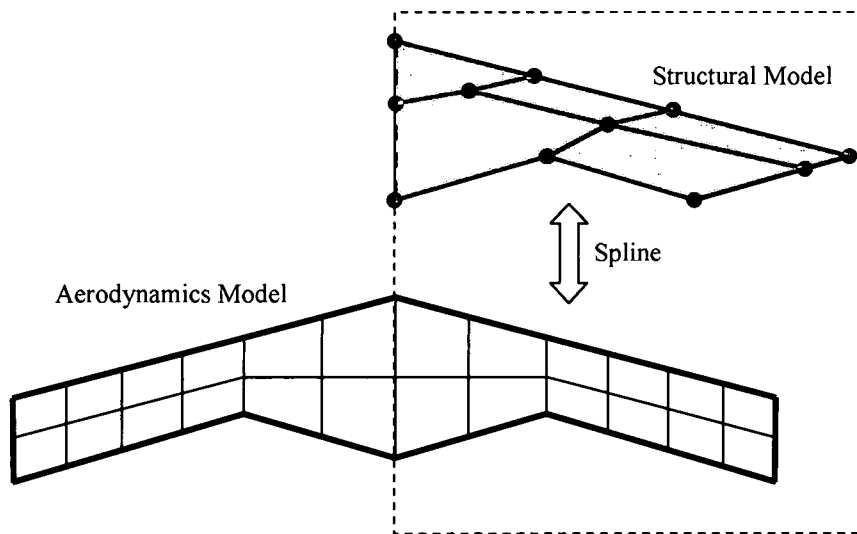


Figure 33 Structural and aerodynamic model integration

### 6.3 Problem Formulation

Among numerous cost functions that can be devised for a thickness or cross-sectional area optimization of structural members, a suitable objective for air vehicle

design is to minimize the total structural weight. Such a weight-minimization problem can be written in the following format:

Minimize:

$$g_0(\mathbf{A}) = \sum_{i=1}^{N_L} \gamma A_i l_i \quad (6.2)$$

Subject to:

$$\mathbf{S}_3^{(i)} = \mathbf{K}\mathbf{U}^{(i)} - \mathbf{F}^{(i)} = \mathbf{0} \quad i = 1 \dots N_{shape} \quad (6.3)$$

$$(T_j^{(i)} - U_j^{(i)})^2 - \varepsilon_{\max}^2 \leq 0 \quad i = 1 \dots N_{shape} \quad j = 1 \dots N_{tgt} \quad (6.4)$$

$$f_{\sigma-j}^{(i)} = \frac{|\sigma_j^{(i)}|}{\sigma_{\max}} - 1 \leq 0 \quad i = 1 \dots N_{shape} \quad j = 1 \dots N_L \quad (6.5)$$

$$A_{\min} \leq \mathbf{A} \leq A_{\max} \quad (6.6)$$

The objective function (6.2) represents the sum of each line element weight, where  $\gamma$  is the specific weight of the material,  $A_i$  is the cross-sectional area of  $i^{\text{th}}$  line element, and  $l_i$  is the length of  $i^{\text{th}}$  line element. For the sizing problem, out-of-plane aerodynamics loads must be considered. Therefore, the equilibrium equations (6.3) represent the steady state of a structure under in-plane and out-of-plane aerodynamics and actuation loads for  $i^{\text{th}}$  configuration. In this research, topology synthesis is performed by considering only in-plane loads with assumption that the actuation of a mechanized structure is independent of out-plane loads. This is a reasonable assumption for an in-plane morphing problem where induced structural displacements occur only in planer directions. In addition, it should be noted that the structural and mechanism layout determined from the topology synthesis must not be disturbed to preserve the morphing capability of the structures. In this investigation, the morphing shape is sustained using the shape constraints (6.4)

during the size optimization process. (6.5) is the mean stress constraint, which will be discussed in the subsequent section. The minimum cross-sectional area and allowable stress of each structural member must be assigned an appropriate value to maintain its in-plane and out-of-plane structural integrities. In addition to constraints (6.3) to (6.6), one may need to employ supplementary measures or other provisions to further ensure the preservation of morphing characteristics, depending on the problem.

### 6.3.1 Mean Positive Stress Constraint

The stress constraint (6.5) is the mean positive stress constraint used by Hetrick et. al. in their investigation [24]. This stress definition only considers the maximum value of normal stress in a line element at the middle point along its length. Although such a representation may not be the most reliable measure of element stress, its simplicity is especially beneficial in achieving reductions in the amount of design constraints that the problem contains, as one will observe in this section. In addition, such an expression of normal stress allows significant reduction in computational cost. In general, one can express the normal stress in a line element as a combination of normal and bending components:

$$\sigma_j^{(i)} = \frac{N_j^{(i)}}{A_j} - \frac{M_{z-j}^{(i)} y_j}{I_z} - \frac{M_{y-j}^{(i)} z_j}{I_y} \quad (6.7)$$

In order to reduce the number of displacement components in the stress definition, one can consider the stress only at the mid-length. The further simplification in the stress expression can be made by considering  $y_j = z_j = A_j^{1/2}$ :

$$\sigma_j^{(i)} = \frac{E}{l_j} \Delta u_j^{(i)} - \frac{EA_j^{1/2}}{2l_j} \Delta \theta_j^{(i)} \quad (6.8)$$

where

$$\Delta u_j^{(i)} = u_{2-j}^{(i)} - u_{1-j}^{(i)} \quad (6.9)$$

$$\Delta \theta_j^{(i)} = \theta_{z2-j}^{(i)} - \theta_{z1-j}^{(i)} + \theta_{y1-j}^{(i)} - \theta_{y2-j}^{(i)} \quad (6.10)$$

One may notice from (6.9) and (6.10) that the new stress expression (6.8) only contains 6 out of 12 degrees of freedom. This indicates that only a half of the entire displacement gradients are necessary upon sensitivity computations. This is beneficial, since the displacement gradients are computationally expensive to obtain. Additionally, in order to eliminate the necessity to constrain both positive and negative stresses, one can take the absolute value of the stress expression above:

$$|\sigma_j^{(i)}| = \frac{E}{l_j} \sqrt{(\Delta u_j^{(i)})^2} + \frac{EA_j^{1/2}}{2l_j} \sqrt{(\Delta \theta_j^{(i)})^2} \quad (6.11)$$

This is the mean stress expression that appears in the stress constraint (6.5). One may notice that a subtraction in (6.7) is changed to an addition in (6.11). Consequently, the value of (6.11) is greater than or equal to the real stress value and it can be considered as an overestimate of the real stress. One may argue that such an expression of normal stress is inaccurate and the real stress should be considered instead. It is important to remember that the ability of optimization techniques to attain convergence is greatly affected by the size of optimization problem and it is almost always a good practice to keep variables and constraints at minimally required quantities. The mean stress expression reduces the amount of constraints into half and also sensitivity generation cost into half, as described above.

It is important to note that displacement components in the stress expression are in the local level. In order to express (6.9) and (6.10) in the global level, one can consider the following transformation:

$$\Delta u_j^{(i)} = (U_{2-j}^{(i)} \cos \theta_j + V_{2-j}^{(i)} \sin \theta_j) - (U_{1-j}^{(i)} \cos \theta_j + V_{1-j}^{(i)} \sin \theta_j) \quad (6.12)$$

One should note that (6.12) does not contain out-of-plane translational terms since the global and local out-of-plane coordinates coincide for an in-plane problem. In matrix form,

$$\Delta u_j^{(i)} = [\dots, -\cos \theta_j, -\sin \theta_j, \dots, \cos \theta_j, \sin \theta_j, \dots] \mathbf{U}^{(i)} = \mathbf{\Gamma}_{u-j}^T \mathbf{U}^{(i)} \quad (6.13)$$

For the rotational counterpart,

$$\Delta \theta_j^{(i)} = \Theta_{22-j}^{(i)} - \Theta_{21-j}^{(i)} + (\Theta_{y1-j}^{(i)} \cos \theta_j - \Theta_{x1-j}^{(i)} \sin \theta_j) - (\Theta_{y2-j}^{(i)} \cos \theta_j - \Theta_{x2-j}^{(i)} \sin \theta_j) \quad (6.14)$$

In matrix form,

$$\Delta \theta_j^{(i)} = [\dots, -\sin \theta_j, \cos \theta_j, -1, \dots, \sin \theta_j, -\cos \theta_j, 1, \dots] \mathbf{U}^{(i)} = \mathbf{\Gamma}_{\theta-j}^{(i)} \mathbf{U}^{(i)} \quad (6.15)$$

Using (6.13) and (6.15), the mean stress (6.11) can be written in the global form:

$$|\sigma_j^{(i)}| = \frac{E}{l_j} \sqrt{(\mathbf{\Gamma}_{u-j}^T \mathbf{U}^{(i)})^2} + \frac{EA_j^{1/2}}{2l_j} \sqrt{(\mathbf{\Gamma}_{\theta-j}^T \mathbf{U}^{(i)})^2} \quad (6.16)$$

#### 6.4 Sensitivity Analysis

The sensitivities of objective and constraint functions can be obtained analytically. The sensitivity of objective function (6.2) is straight forward:

$$\frac{\partial g_0}{\partial A_e} = \gamma l_e \quad (6.17)$$



For the stress constraint (6.5), one must first obtain the gradient of mean stress (6.11) with respect to design variables,

$$\frac{\partial |\sigma_j^{(i)}|}{\partial A_e} = \frac{E}{l_j} \frac{\partial}{\partial A_e} \left( \sqrt{(\Delta u_j^{(i)})^2} \right) + \frac{E}{2l_j} \frac{\partial}{\partial A_e} \left( A_j^{1/2} \sqrt{(\Delta \theta_j^{(i)})^2} \right) \quad (6.18)$$

After performing differentiation and several algebraic manipulations, one can express the above gradient in the following form:

$$\frac{\partial |\sigma_j^{(i)}|}{\partial A_e} = \frac{E}{l_j} \frac{1}{\sqrt{(\Delta u_j^{(i)})^2}} \Delta u_j^{(i)} \frac{\partial \Delta u_j^{(i)}}{\partial A_e} + \frac{\delta_{ej} E}{4l_j A_j^{1/2}} \sqrt{(\Delta \theta_j^{(i)})^2} + \frac{E A_j^{1/2}}{2l_j} \frac{1}{\sqrt{(\Delta \theta_j^{(i)})^2}} \Delta \theta_j^{(i)} \frac{\partial \Delta \theta_j^{(i)}}{\partial A_e} \quad (6.19)$$

where  $\delta_{ej}$  is Kronecker delta that gives 1 only when subscripts  $e$  and  $j$  are equal and 0 when the subscripts are not equal. The gradient of (6.13) and (6.15) can be obtained by the adjoint method:

$$\Delta u_j^{(i)} = \Gamma_{u-j}^T \mathbf{U}^{(i)} - \zeta_{u-j}^T (\mathbf{K} \mathbf{U}^{(i)} - \mathbf{F}^{(i)}) \quad (6.20)$$

$$\frac{\partial \Delta u_j^{(i)}}{\partial A_e} = \Gamma_{u-j}^T \frac{\partial \mathbf{U}^{(i)}}{\partial A_e} - \zeta_{u-j}^T \frac{\partial \mathbf{K}}{\partial A_e} \mathbf{U}^{(i)} - \zeta_{u-j}^T \mathbf{K} \frac{\partial \mathbf{U}^{(i)}}{\partial A_e} \quad (6.21)$$

Notice that the force term is not a function of the size variables. As discussed previously for the sensitivity analysis for topology problem, one can collect gradient terms and obtain the following sensitivity expression:

$$\frac{\partial \Delta u_j^{(i)}}{\partial A_e} = -\zeta_{u-j}^T \frac{\partial \mathbf{K}}{\partial A_e} \mathbf{U}^{(i)} \quad (6.22)$$

where one can obtain  $\zeta_{u-j}$  can be obtained by solving the adjoint problem:

$$\mathbf{K} \zeta_{u-j} = \Gamma_{u-j} \quad (6.23)$$

Similarly for (6.15),

$$\frac{\partial \Delta \theta_j^{(i)}}{\partial A_e} = -\zeta_{\theta-j}^T \frac{\partial K}{\partial A_e} \mathbf{U}^{(i)} \quad (6.24)$$

where  $\zeta_{\theta-j}$  can be obtained by solving,

$$K \zeta_{\theta-j} = \Gamma_{\theta-j} \quad (6.25)$$

Now, one can obtain the gradient of mean stress constraint using (6.19) along with (6.22) and (6.24):

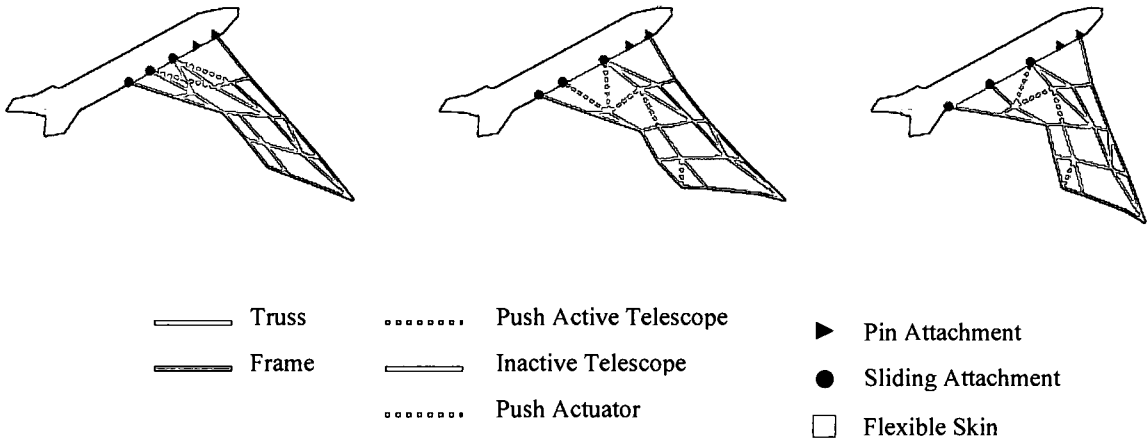
$$\frac{\partial f_{\sigma-j}^{(i)}}{\partial A_e} = \frac{1}{\sigma_{\max}} \frac{\partial |\sigma_j^{(i)}|}{\partial A_e} \quad (6.26)$$

The sensitivity of shape constraint (6.4) was already discussed in section 4.6 and 5.3 for the topology problem.

## 6.5 Example Problem and Results

The size optimization is performed on the structure determined by the topology optimization. The selected topology solution shown in Figure 34 is very similar to the one presented in the previous chapter. This topology solution contains 17 trusses, 14 frames, 2 inactive telescopes, 3 push active telescopes, 6 push actuators, 2 pinned/fixed attachments and 3 sliding attachments. The topology solution is first post-processed and re-meshed to remove void elements and associated degrees of freedom. The resulting input model to the sizing optimization is created by applying out-of-plane degrees of freedom and dividing the line elements into segments. Each line element is divided into two separate segments. All line elements have initial 1 inch x 1 inch square cross section with material property of Aluminum.

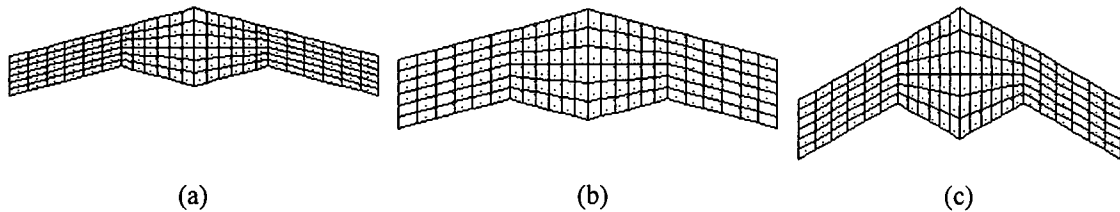
In this example problem, the maximum and minimum line cross-sectional area is set to 9 square inch and 0.5 square inch, respectively. The upper bound of the normal stress constraint is set to 30 ksi, assuming the safety factor of approximately 1.5 for the high-strength aluminum (i.e. 2024-T4) with yield strength of 47 ksi. The initial stress computation reveals that most structural members are within the stress limit of 30 ksi. There are few members at the inboard trailing edge section, where some inactive telescopes are stressed beyond its yield strength. In addition, there are several elements at the root section that are stressed beyond the constraint upper bound, but still below the yield stress. It is expected that size optimization will reinforce the root section to alleviate these stress constraint violations. As in the topology synthesis, GCMMA is used to perform the size optimization.



**Figure 34 Topology data for the example size optimization problem**

The aerodynamic forces are determined using VLM and translated to the structure as described previously. The quasi-steady aerodynamic models, as shown in Figure 35, are created for each configuration and applied individually to the structural model. In this particular case, the air vehicle is assumed to be in symmetric flight at an altitude of 15,000 feet in the U.S. standard atmosphere, and an air speed of 250 feet per second

(approximately 170 miles per hour) with constant 3 degrees angle of attack for all configurations.



**Figure 35 Aerodynamics Models (a) loiter (b) high-lift (c) climb configurations**

The size optimization solution is provided in Figure 36. As expected, the high strength section has formed at the inboard section where highly stressed structural members are prevalent before the size optimization. The structural members that exceed the normal stress limit of 30 ksi are strengthened to satisfy the stress constraint at the beginning of the process as such constraint violations are severely penalized in the optimization. In addition to correcting the stress constraint violations due to in-plane actuation loads, it is possible that the in-board section of the wing has higher strength requirements due to the out-of-plane bending and torsional moments that the section must withstand. The high strength section is characterized by a formation of active and inactive telescopes and trusses with 5.98 to 7.16 square inch in cross sectional area. The maximum size of 7.16 and 7.02 square inch appears in two telescopes that form the morphing boundary at the trailing-edge.

The solution also reveals the mid strength section along the wing leading edge where the structure must carry in-plane drag loads and resist out-of-plane bending and torsional loads. It appears that this leading edge spar is acting as a primary load path that transfers actuation and aerodynamics loads to the high strength section. This section is

characterized by frame and truss elements with all cross sectional areas in vicinity of 1.60 square inch, which is higher, though not significantly, than the initial 1.0 square inch.

The figure also shows the tapered beam at the tip section. One can hypothesize that the tip section needs to be reinforced against bending due primarily to actuation loads, since the aerodynamic loads are generally not very intensive around the tip section. The thickest part of this tapered beam is 5.77 square inch and the thinnest part has 0.91 square inch cross section.

The optimization has reduced all other components in the structure to approximately 0.70 square inch. The original structural weight (it does not include the weight of flexible skin and attachments) of 83.76 pounds is actually increased to 114.2 pounds after the optimization, although the objective is to minimize the structural weight. This is a reasonable outcome since the optimization has been performed on the structure that initially violates stress constraints, as mentioned previously. In order to satisfy the stress constraints, the optimization has to reinforce the structure and, consequently, increase the total structural weight. One should note that the first priority in optimization is to meet the design constraints, regardless of what the objective function indicates. In addition, the initial constraint violation causes very erratic behavior in the optimization process and GCMMA has wandered without a clear indication of convergence in a solution process. While such an instability has been observed in the optimization process, the result reveals a surprisingly logical structure. Further investigations are probably necessary to improve the solution.

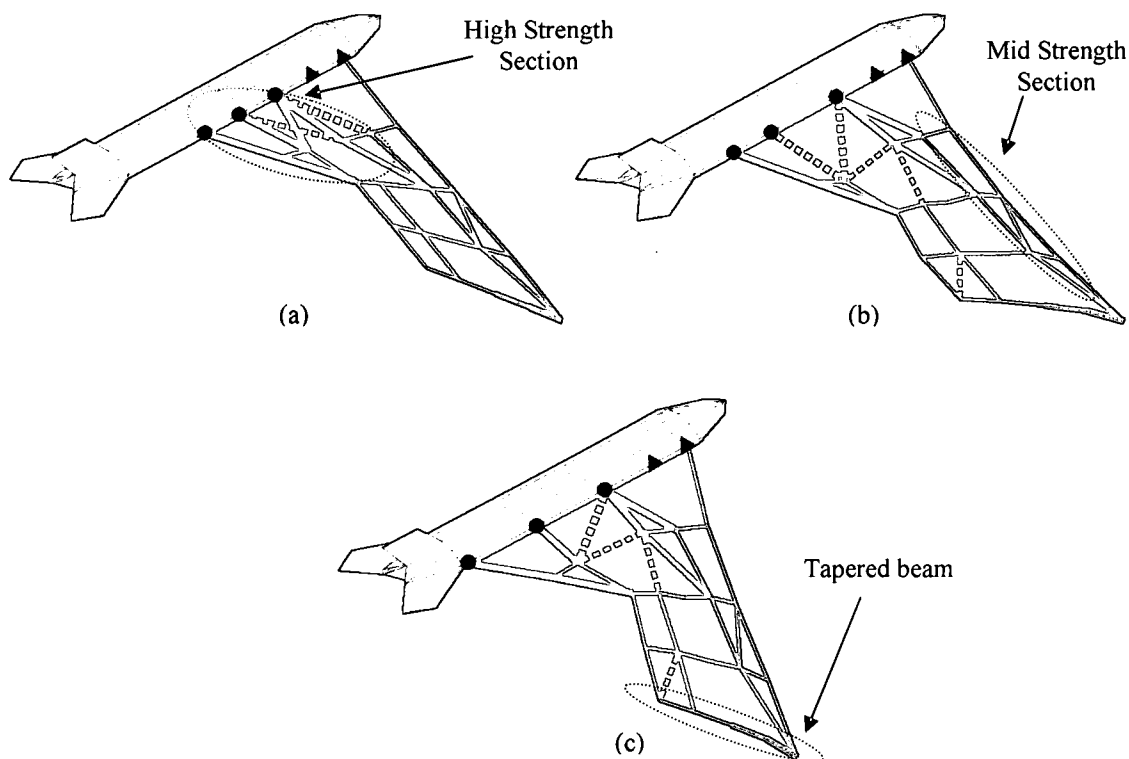


Figure 36 Solution of the Example Problem (a) loiter (b) high-lift (c) climb configurations

## 6.6 Conclusion

In this chapter, the size optimization has been demonstrated on the structural layout obtained from the topology synthesis. The strategy to effectively transfer topology solution as an input to the size optimization has been developed. The topology solution is first post-processed and the analysis model is modified and re-meshed to remove degrees of freedom associated with void elements. In addition, the out-of-plane degrees of freedom are added to the model and aerodynamic loads obtained from Vortex Lattice Method is translated to the structural nodes using the infinite plate spline technique.

During the optimization process, the convergence characteristic has been observed to be somewhat irregular and erratic. This is questionable as the GCMMA generally converges monotonically to the optimum solution with a strictly lower

objective value in every iterative step. Though such a numerical glitch may have been experienced, the solution of an example problem reveals a surprisingly logical structure. In the solution, one can observe the clear load-path from wing tip to wing root. The optimization process has reinforced the highly stressed in-board section. The leading edge spar is clearly indicated and the wing tip has been reinforced against actuation and aerodynamic loads.

## **CHAPTER 7**

### **SUMMARY AND RECOMMENDATIONS**

#### **7.1 Summary**

In this research, the topology and size optimization methodology for determination of a mechanized actuated structure is investigated. The in-plane morphing wing model has been selected for demonstration purposes. The modeling concept incorporates a variety of active and inactive elements (i.e. frame, truss, telescopes, actuator, attachment, and joint) to effectively produce rigid-body shape changes in a morphing structure. Moreover, several optimization problem formulations has been discussed and investigated to observe the formulation dependency on numerical solutions, as well as meaningfulness of the formulation itself. The primary contributions of the research have been (1) the development of an effective finite element model of morphing structures, (2) topology synthesis of multiple configuration morphing structures, and (3) an implementation of size optimization process to provide a further realization to the existing structural topology.

In chapter 4, topology optimization formulations for the single configuration problem have been discussed. The first formulation involves the multiple objective function. Other cases are single objective formulation with either actuator utilization or shape error minimization as an objective and an appropriate set of constraints. The



combination of these formulations is also investigated. The results of an example in-plane morphing problem showed interestingly similar structures with a leading edge spar formation and an actuator concentration at the root section for all problem formulations. In addition to such a similarity, distinct characteristics of each problem formulation were observed. The multiple objective formulation has characteristics of minimizing both actuator utilization and shape error proportionally as defined by its objective weight constants. The multiple objective formulation is especially beneficial when both actuator and shape objectives are considered as critical design parameters. The actuator utilization minimization formulation provided a result with superior actuator utilization with less accurate shape. Such a solution was expected, since the formulation has a sole objective to minimize actuator utilizations. In addition, large shape constraint violations at the initial iteration that naturally occur in this formulation caused instability in optimization process, though the converged solution was eventually attained. The shape error minimization formulation also provided a result with an acceptable target shape achievement, though actuator utilization was fixed as a constraint. The combinations of these formulations are considered and demonstrated that such sequential solutions of the shape and multiple objective problem followed by the actuator minimization have an advantage in solution controllability and improving the result. Finally, the concluding remark was made to emphasize that a choice of which formulation to be used is very much problem dependent and one must decide according to his/her design requirements.

In chapter 5, many enhancements and extensions were introduced to the topology problem formulation by considering more realistic design requirements and descriptions. In addition to redeveloping the problem formulation into the one that is capable of

accommodating multiple-configuration definitions, several important improvements were made in the formulation to provide more precise definitions of a structural volume and a means to control actuator distribution. The important issues on the external-load dependency and the reversibility of a structural design, as well as the appropriate selection of the reference configuration, are also addressed in the research. The results of an example multiple configuration problem reveal that these improvements indeed have the effect of enhancing the solution quality in terms of physical meaningfulness. The basic formulation has provided a solution with a truss-dominated structure with an excessive actuator distribution. This basic solution is improved by a modified volume constraint that eliminates bias towards utilization of frame elements. The formulation is further augmented by the actuator distribution control objective term. It is observed that the combination of these volume and actuator distribution definitions drastically improve the solution quality and provided a means to tailor a solution in accordance with design requirements. Finally, the single and multiple configuration problem formulations are compared through an additional example problem. The comparison has revealed that the improvements and enhancements made to the problem formulation are indeed valid and the new formulation introduced in the chapter is superior to the previous ones.

The size optimization strategy was developed and demonstrated in chapter 6. The topology solution is used as an input to the size optimization. The topology solution is first post-processed and the analysis model is modified to remove degrees of freedom associated with void elements. The out-of-plane degrees of freedom are applied to the model and aerodynamic loads from aerodynamic panels are translated to the structural nodes using the infinite plate spline technique. The example size optimization problem

that minimizes the total structural weight has been solved to demonstrate the methodology. The result has revealed reasonably well constructed structure with a clear load path from the wing tip to the root, although some technical anomalies have been observed during the optimization process.

Although more investigations are required to further validate the computational design methodology presented in this research, it is sufficiently demonstrated via sample in-plane morphing problems that the methodology may provide a viable solution. While numerous simplifications are employed in this research, this preliminary investigation serves as important evidence that the methodology, with further extensions and improvements, can potentially be utilized for determination of a practicable morphing aircraft structure.

## **7.2 Future Research Direction and Recommendations**

While the outcome of the research appears favorable and promising, there are several subjects that were purposely not included in the research due to the imposed time constraint. Although these subjects are given careful consideration at the beginning of the research, the decision was made to leave them as a future research task. Though, the importance of these subjects should not be overlooked and is discussed below with brief research directions and recommendations.

### **7.2.1 Material and Geometric Nonlinearity**

In this research, linear finite element analysis has been employed exclusively to keep the research at conceptual level. However, the general motions of a morphing structure typically involve large rigid-body displacements and elastic deformations that

cannot be accurately portrayed by the small displacement assumption and linear elastic material characteristics that are integrated in the linear FEA formulation. For the morphing mechanism and structure that undergo large rigid-body displacement, stiffness and force directions should be updated in the analysis iteratively to obtain a truly accurate result. The material nonlinearity is probably not a significant concern as the morphing structural concept in the research does not anticipate the primary structural members to have large elastic deformations. Nonetheless, the material nonlinearity may have to be considered for a flexible skin model that could be based on an innovative polymer based material with highly nonlinear characteristics. The effect of such nonlinearities in topology synthesis of compliant mechanisms is well documented in the text by Bendsoe and Sigmund [2], though the compliance based mechanism may be more susceptible to material nonlinearity than the rigid-body based mechanism presented in the research.

### **7.2.2 Simultaneous Topology Synthesis and Size Optimization**

In this research, the topology synthesis and size optimization has been performed in sequential manner. First, topology of the structure is determined using the synthesis technique described in the previous chapters. Then, the size optimization is performed on the existent structural layout. Such a multiple stage optimization approach is perfectly logical and probably the only feasible way, since the contradictions in topology and sizing problem definitions preclude integrations of solution procedures effectively. That is, the size variables are generally continuous and topology variable are discrete 0-1 and they cannot be easily mixed in the optimization problem without seriously jeopardizing one or another. However, a better solution can probably be obtained if both topology and elemental size of the structure could be considered simultaneously in the optimization.

As observed in this research, the topology solution contains structural members that are stressed beyond the yield strength of the material. Though the size optimization corrects the situation by reinforcing these members, such overstressed conditions may raise uncertainties in the optimality of the topology solution. In addition, the size optimization has to start the iteration from the outside of design feasible region due to initially existent stress constraint violations. Although simultaneous topology and dimensional optimization has been investigated by Lu, et. al. in their research of compliant mechanism synthesis [18,19], the applicability of such a methodology to the morphing structural concept presented in this research is somewhat doubtful. The new and innovative methodology that is tailored to this research must be developed to perform the simultaneous topology and size optimization effectively.

### **7.2.3 Shape Optimization**

The topology synthesis is performed using the mesh orientation and node locations that are predefined. That is, the elements can occupy only where the mesh exists, regardless of how finely the design domain could be meshed. Since the structural mesh is predefined, it will make the topology solution mesh-dependent. In order to improve the topology solution, the shape optimization can be performed. The design variables in shape optimization are generally a parametric representation of nodal coordinates of each structural member. As the nodal coordinates of elements vary with a certain objective to optimize, a highly refined structural layout may be revealed. The sensitivity analysis of the shape optimization problem is generally much more involved than those of topology and sizing problems. The shape and size optimization can be performed simultaneously as described in the investigation by Hetrick et. al. [24].

Though the integration of simultaneous size and shape optimization for a morphing structure will require further investigations, the development of effective dimensional optimization strategy is the next logical extension to this research.

#### **7.2.4 Aeroelastic Equilibrium**

In this research, rigid-aerodynamics and structural mechanics are considered individually and interfaced using the infinite plate spline technique without an introduction of coupled influence terms in the governing equations. That is, the coupled influence of fluid-structure interaction was not considered in the research. However, the aerodynamics loads and structural responses are dependent of one another and it is often impractical to consider them separately. In addition, the degree of influence of such fluid-structure interactions becomes more significant as the flight dynamic pressure increases. Therefore, one should certainly consider the aeroelastic equilibrium condition in the problem formulation. Although the application of static aeroelastic equilibriums to the optimization problem may not be an impossible task as other researchers in the field have demonstrated in the past, the multiple configuration definition in this research will require multiple aeroelastic equilibriums to be satisfied simultaneously. Such a simultaneous solution is probably computationally intensive and difficult especially if the nonlinear analysis is considered. Finally, dynamics and flutter characteristics of the structure should also be considered in the future research.

## APPENDIX A

### METHOD OF MOVING ASYMPTOTES

The Method of Moving Asymptotes developed by Svanberg [27] is discussed in this appendix. The Method of Moving Asymptotes or MMA is based on a type of convex approximation. In this method, a convex approximating sub-problem is generated and solved iteratively. In general, we can write an optimization problem in the form:

$$\begin{aligned}
 &P: \text{Minimize} \\
 &\quad f_0(\mathbf{x}) \quad \mathbf{x} \in R^n \\
 &\text{Subject to:} \\
 &\quad f_i(\mathbf{x}) \leq \hat{f}_i \quad i = 1 \dots m \\
 &\quad \tilde{x} \leq x_j \leq \bar{x} \quad j = 1 \dots n
 \end{aligned} \tag{A-1}$$

As in many other sequential optimization techniques, MMA follows the well-established general solution procedure:

- Step 1 Define an initial point  $\mathbf{x}(0)$
- Step 2 Given  $\mathbf{x}(k)$ , calculate  $f_i(\mathbf{x}(k))$  and its gradient for  $i=0 \dots m$ .
- Step 3 Generate a sub-problem  $P(k)$  by replacing the original objective and constraint functions by a convex approximation.
- Step 4 Solve the sub-problem and obtain  $\mathbf{x}(k+1)$ .
- Step 5 Update the design variables and repeat the process until the convergence is attained.

In MMA, each approximating function is obtained by a linearization of the original function in variables that are defined by upper or lower asymptotes, depending on the signs of the derivatives at that particular design point. We start from the first order Taylor approximation of  $f_i$  at design point  $k$ :

$$f_i^{(k)}(\mathbf{X}) = f_i(\mathbf{X}^{(k)}) + \sum_{j=1}^n \frac{\partial f_i}{\partial X_j}(\mathbf{X}^{(k)}) (X_j - X_j^{(k)})$$

where,

$$\mathbf{X} = [X_1, X_2, \dots, X_n]^T$$

$$\mathbf{X}^{(k)} = [X_1^{(k)}, X_2^{(k)}, \dots, X_n^{(k)}]^T$$
(A-2)

Now, we transform those design variables in the form:

$$X_j = \frac{1}{U_j^{(k)} - x_j} \quad X_j^{(k)} = \frac{1}{U_j^{(k)} - x_j^{(k)}}$$

OR

$$X_j = \frac{1}{x_j - L_j^{(k)}} \quad X_j^{(k)} = \frac{1}{x_j^{(k)} - L_j^{(k)}}$$
(A-3)

By applying the upper asymptote variables in (A-3) to the Taylor approximation in (A-2), one can write the following approximation:

$$f_i^{(k)}(\mathbf{x}) = f_i(\mathbf{x}^{(k)}) + \sum_{j=1}^n \frac{\partial f_i}{\partial X_j}(\mathbf{x}^{(k)}) \left( \frac{1}{U_j^{(k)} - x_j} - \frac{1}{U_j^{(k)} - x_j^{(k)}} \right)$$
(A-4)

Considering the chain rule,

$$\frac{\partial f_i}{\partial X_j} = \sum_{k=1}^n \frac{\partial f_i}{\partial x_k} \frac{\partial x_k}{\partial X_j}$$
(A-5)

And,



$$\frac{\partial x_k}{\partial X_j} = 0 \quad \text{for } k \neq j \quad (\text{A-6})$$

Here, one can write the variable transformation at  $k^{\text{th}}$  design point as,

$$\frac{\partial x_j}{\partial X_j}(x_j^{(k)}) = \frac{dx_j}{d\left(\frac{1}{U_j^{(k)} - x_j}\right)} \bigg|_{x_j^{(k)}} = \frac{dx_j}{\frac{dx_j}{(U_j^{(k)} - x_j)^2}} \bigg|_{x_j^{(k)}} = (U_j^{(k)} - x_j^{(k)})^2 \quad (\text{A-7})$$

Using this transformation,

$$\frac{\partial f_i}{\partial X_j}(\mathbf{x}^{(k)}) = \frac{\partial f_i}{\partial x_j}(\mathbf{x}^{(k)}) (U_j^{(k)} - x_j^{(k)})^2 \quad (\text{A-8})$$

Applying the above function

$$f_i^{(k)}(\mathbf{x}) = f_i(\mathbf{x}^{(k)}) + \sum_{j=1}^n \frac{\partial f_i}{\partial x_j}(\mathbf{x}^{(k)}) (U_j^{(k)} - x_j^{(k)})^2 \left( \frac{1}{U_j^{(k)} - x_j} - \frac{1}{U_j^{(k)} - x_j^{(k)}} \right) \quad (\text{A-9})$$

The above approximating function can be simplified as,

$$f_i^{(k)}(\mathbf{x}) = r_i^{(k)} + \sum_{j=1}^n \left( \frac{p_{ij}^{(k)}}{U_j^{(k)} - x_j} \right) \quad (\text{A-11})$$

where

$$r_i^{(k)} = f_i(\mathbf{x}^{(k)}) - \sum_{j=1}^n \left( \frac{p_{ij}^{(k)}}{U_j^{(k)} - x_j^{(k)}} \right) \quad (\text{A-12})$$

$$p_{ij}^{(k)} = \frac{\partial f_i}{\partial x_j}(\mathbf{x}^{(k)}) \left( U_j^{(k)} - x_j^{(k)} \right)^2 \quad (\text{A-13})$$

Now, considering only the lower asymptote variables in (A-3) and following the same procedure, one can obtain the following approximating function based on the lower asymptote variables:

$$f_i^{(k)}(\mathbf{x}) = r_i^{(k)} + \sum_{j=1}^n \left( \frac{q_{ij}^{(k)}}{x_j^{(k)} - L_j^{(k)}} \right) \quad (\text{A-14})$$

where

$$r_i^{(k)} = f_i(\mathbf{x}^{(k)}) - \sum_{j=1}^n \left( \frac{q_{ij}^{(k)}}{x_j^{(k)} - L_j^{(k)}} \right) \quad (\text{A-15})$$

$$q_{ij}^{(k)} = -\frac{\partial f_i}{\partial x_j}(\mathbf{x}^{(k)}) \left( x_j^{(k)} - L_j^{(k)} \right)^2 \quad (\text{A-16})$$

Since we want to use upper asymptote approximation when  $\partial f_i / \partial x_j > 0$  and lower asymptote approximation when  $\partial f_i / \partial x_j < 0$ , we can create the convex approximation based on a combination of (A-11) to (A-16):

$$f_i^{(k)}(\mathbf{x}) = r_i^{(k)} + \sum_{j=1}^n \left( \frac{p_{ij}^{(k)}}{U_j^{(k)} - x_j} + \frac{q_{ij}^{(k)}}{x_j - L_j^{(k)}} \right)$$

where,

$$p_{ij}^{(k)} = \begin{cases} \frac{\partial f_i}{\partial x_j}(\mathbf{x}^{(k)}) (U_j^{(k)} - x_j^{(k)})^2 & \text{if } \frac{\partial f_i}{\partial x_j} > 0 \\ 0 & \text{if } \frac{\partial f_i}{\partial x_j} \leq 0 \end{cases}$$

$$q_{ij}^{(k)} = \begin{cases} 0 & \text{if } \frac{\partial f_i}{\partial x_j} \geq 0 \\ -\frac{\partial f_i}{\partial x_j}(\mathbf{x}^{(k)}) (x_j^{(k)} - L_j^{(k)})^2 & \text{if } \frac{\partial f_i}{\partial x_j} < 0 \end{cases} \quad (\text{A-18})$$

$$r_i^{(k)} = f_i(\mathbf{x}^{(k)}) - \sum_{j=1}^n \left( \frac{p_{ij}^{(k)}}{U_j^{(k)} - x_j^{(k)}} + \frac{q_{ij}^{(k)}}{x_j^{(k)} - L_j^{(k)}} \right)$$

This is the convex approximation used in the MMA algorithm. Now, we can write an approximation of the standard problem (A-1) using the convex approximation (A-18):

$P^{(k)}$  : Minimize

$$r_0^{(k)} + \sum_{j=1}^n \left( \frac{p_{0j}^{(k)}}{U_j^{(k)} - x_j} + \frac{q_{0j}^{(k)}}{x_j - L_j^{(k)}} \right)$$

Subject to :

$$r_i^{(k)} + \sum_{j=1}^n \left( \frac{p_{ij}^{(k)}}{U_j^{(k)} - x_j} + \frac{q_{ij}^{(k)}}{x_j - L_j^{(k)}} \right) \leq \hat{f}_i \quad i = 1 \dots m \quad (\text{A-19})$$

and

$$\max\{\tilde{x}_j, \alpha_j^{(k)}\} \leq x_j \leq \min\{\hat{x}_j, \beta_j^{(k)}\} \quad j = 1 \dots n$$

Here,  $\alpha$  and  $\beta$  are move limits for  $j^{\text{th}}$  variable at  $k^{\text{th}}$  iteration. In general, these move limits are chosen to avoid the possibility of any divide-by-zero while solving the sub-problem (A-19).  $\alpha$  and  $\beta$  should be chosen such that,

$$L_j^{(k)} < \alpha_j^{(k)} < x_j^{(k)} < \beta_j^{(k)} < U_j^{(k)} \quad (\text{A-20})$$

Svanberg mentions that a good choice of these move limits may be,

$$\alpha_j^{(k)} = 0.9L_j^{(k)} + 0.1x_j^{(k)} \quad \beta_j^{(k)} = 0.9U_j^{(k)} + 0.1x_j^{(k)} \quad (\text{A-21})$$

Now, we need to discuss how to choose values for asymptote parameters, L and U. The general rule for updating U and L is the following:

- Move the asymptotes closer to the current design point if the process oscillates. This will give more curvature to the approximation and, therefore, more conservative the sub-problem becomes (stabilization).
- If the process is monotone and slow, move the asymptote away from the current design point. (less curvature to the approximation, less conservative, moves quicker from one point to another)

This rule can be expressed numerically as follows:

For  $k=0$  and  $k=1$ ;

$$L_j^{(k)} = x_j^{(k)} - \left( \bar{x}_j - \tilde{x}_j \right) \quad U_j^{(k)} = x_j^{(k)} + \left( \bar{x}_j - \tilde{x}_j \right) \quad (\text{A-22})$$

For  $k \geq 2$ ;

(a) If the signs of  $x(k) - x(k-1)$  and  $x(k-1) - x(k-2)$  are not consistent, an oscillatory condition may be detected. Then,

$$\begin{aligned} L_j^{(k)} &= x_j^{(k)} - s \left( x_j^{(k-1)} - L_j^{(k-1)} \right) \\ U_j^{(k)} &= x_j^{(k)} + s \left( U_j^{(k-1)} - x_j^{(k-1)} \right) \end{aligned} \quad (\text{A-23})$$

where  $s$  is a constant between 0 to 1.

(b) If the signs of  $x(k) - x(k-1)$  and  $x(k-1) - x(k-2)$  are consistent, asymptotes may be too close to each other and may be slowing the process. Then,

$$\begin{aligned} L_j^{(k)} &= x_j^{(k)} - \frac{\left( x_j^{(k-1)} - L_j^{(k-1)} \right)}{s} \\ U_j^{(k)} &= x_j^{(k)} + \frac{\left( U_j^{(k-1)} - x_j^{(k-1)} \right)}{s} \end{aligned} \quad (\text{A-24})$$

Of course, this is not a hard-set rule and any updating scheme that satisfies the general rule can be utilized.

The sub-problem (A-19) is generated and solved iteratively. The primary advantage of this convex approximation is that the solution always exists and it can be solved using the standard constrained optimization techniques. Svanberg considers the dual method to solve the sub-problem. The dual method is explained in many optimization texts, such as the one written by Vanderplaats [26].

## **APPENDIX B**

### **GLOBALLY CONVERGENT MMA**

In this appendix, the brief explanation of the Globally Convergent Method of Moving Asymptotes (GCMMA) algorithm that was developed by Svanberg [28] is provided. Globally Convergent MMA or GCMMA has few favorable properties that the previous version of MMA did not possess:

- The problem formulation is more robust and versatile. It contains definitions of least-squares problem and min-max problem within the formulation. The original MMA tends to oscillate around a solution for these types of problems.
- GCMMA is more stable around the optimum solution and is capable of attaining the solution much closer to the true optimum than its non-globally-convergent counterpart. From an initial point, the solution converges monotonically towards the KKT points.

The primary difference between the original MMA and GCMMA is that the latter one consists of ‘outer’ and ‘inner’ iterations. Within each outer iteration, the process may have zero, one, or several inner iteration. As we will observe later in the appendix, outer iterations are almost the same as the original MMA and inner iterations sequentially modify the convex approximation (i.e. conservativeness of approximation) of a sub-

problem, if needed, within each outer iterations. In general, we can write an optimization problem in the standard format:

$$\begin{aligned}
 P: \text{ Minimize} \\
 & f_0(\mathbf{x}) \quad \mathbf{x} \in R^n \\
 \text{Subject to:} \\
 & f_i(\mathbf{x}) \leq 0 \quad i = 1 \dots m \\
 & \tilde{x}_j \leq x_j \leq \hat{x}_j \quad j = 1 \dots n
 \end{aligned} \tag{B-1}$$

In GCMMA, we solve the following form of optimization problems:

$$\begin{aligned}
 P: \text{ Minimize} \\
 & f_0(\mathbf{x}) + a_0 z + \sum_{i=1}^m \left( c_i y_i + \frac{1}{2} d_i y_i^2 \right) \quad \mathbf{x} \in R^n \quad \mathbf{y} \in R^m \quad z \in R \\
 \text{Subject to:} \\
 & f_i(\mathbf{x}) - a_i z - y_i \leq 0 \quad y_i \geq 0 \quad z \geq 0 \quad i = 1 \dots m \\
 & \tilde{x}_j \leq x_j \leq \hat{x}_j \quad j = 1 \dots n
 \end{aligned} \tag{B-2}$$

Here,  $f_0 \dots f_m$  are given real valued objective and constraint functions.  $a_0, a_i, c_i$ , and  $d_i$  are given real numbers such that  $a_0 > 0$ ,  $a_i \geq 0$ ,  $c_i \geq 0$ ,  $d_i \geq 0$ , and  $c_i + d_i > 0$  for all  $i$ . Also,  $a_i c_i > a_0$  for all  $i$  with  $a_i > 0$ . For instance, if we want to solve an optimization problem in the standard NLP form, we let  $a_0 = 1$  and  $a_i = 0$  for  $i > 0$ . Then,  $z = 0$  will be true for any optimal solution of the problem (B-2). For each  $i$ , let  $d_i = 0$  and  $c_i$  to be a large number, so that the artificial variable  $y_i$  becomes very expensive to be retained in the objective function. Thus, in most cases,  $y_i$  must vanish in any optimal solutions of the considered problem (B-2) and the corresponding  $\mathbf{x}$  will be an optimal solution of the standard problem (B-1).

The considered problem (B-2) may seem very awkward, but it should be noted that the problem in this form always has feasible solutions. That is, the artificial variable

$y_i$  can always be used to satisfy the constraints, though these variables should vanish in any optimal solutions of the considered problem. This absolute feasibility holds true even if the supplied standard problem does not have any feasible solutions. In such a case, some  $y_i$  is not going to vanish. As in the original MMA, we use a convex function to approximate the original problem:

$$\begin{aligned}
g_i^{(k,v)}(\mathbf{x}) &= \sum_{j=1}^n \left( \frac{p_{ij}^{(k,v)}}{u_j^{(k)} - x_j} + \frac{q_{ij}^{(k,v)}}{x_j^{(k)} - l_j} \right) + r_i^{(k,v)} \quad i = 0, 1, \dots, m \\
p_{ij}^{(k,v)} &= \left( u_j^{(k)} - x_j^{(k)} \right)^2 \left( \max \left\{ 0, \frac{\partial f_i}{\partial x_j}(x^{(k)}) \right\} + \rho_i^{(k,v)} (\hat{x}_j - \tilde{x}_j) \right) \\
q_{ij}^{(k,v)} &= \left( x_j^{(k)} - l_j^{(k)} \right)^2 \left( \max \left\{ 0, -\frac{\partial f_i}{\partial x_j}(x^{(k)}) \right\} + \rho_i^{(k,v)} (\hat{x}_j - \tilde{x}_j) \right) \\
r_i^{(k,v)} &= f_i(x^{(k)}) - \sum_{j=1}^n \left( \frac{p_{ij}^{(k,v)}}{u_j^{(k)} - x_j^{(k)}} + \frac{q_{ij}^{(k,v)}}{x_j^{(k)} - l_j^{(k)}} \right)
\end{aligned} \tag{B-3}$$

Notice that the GCMMA approximation has two indices,  $k$  and  $v$ , where the first one is for the outer iteration and the latter one is for the inner iteration. One should notice that the convexity parameter,  $\rho^{(k,v)}_i$ , is updated, if necessary, within every inner iteration. The considered problem (B-2) can now be written with the convex approximation (B-3) as follows:



Minimize

$$g_0^{(k,v)}(\mathbf{x}) + a_0 z + \sum_{i=1}^m \left( c_i y_i + \frac{1}{2} d_i y_i^2 \right)$$

Subject to:

$$g_i^{(k,v)}(\mathbf{x}) + a_i z - y_i \leq 0$$

(B-4)

$$\mathbf{x} \in X^{(k)}, \quad y \geq 0, \quad z \geq 0$$

where,

$$X^{(k)} = \left\{ x \in X \mid 0.9l_j^{(k)} + 0.1x_j^{(k)} \leq x_j \leq 0.9u_j^{(k)} + 0.1x_j^{(k)}, j=1,\dots,n \right\}$$

Clearly, the most part of this convex approximation is identical to that of the original MMA, except for the term with convexity parameter  $\rho^{(k,v)}_i$ . By graphical observations, we can clearly see the effect of this parameter. Suppose, we want to apply a convex approximation to the real valued function;  $y = x^2 + 1$  at  $x = 0.5$  with  $L = 0.0$  and  $U = 1.0$ :

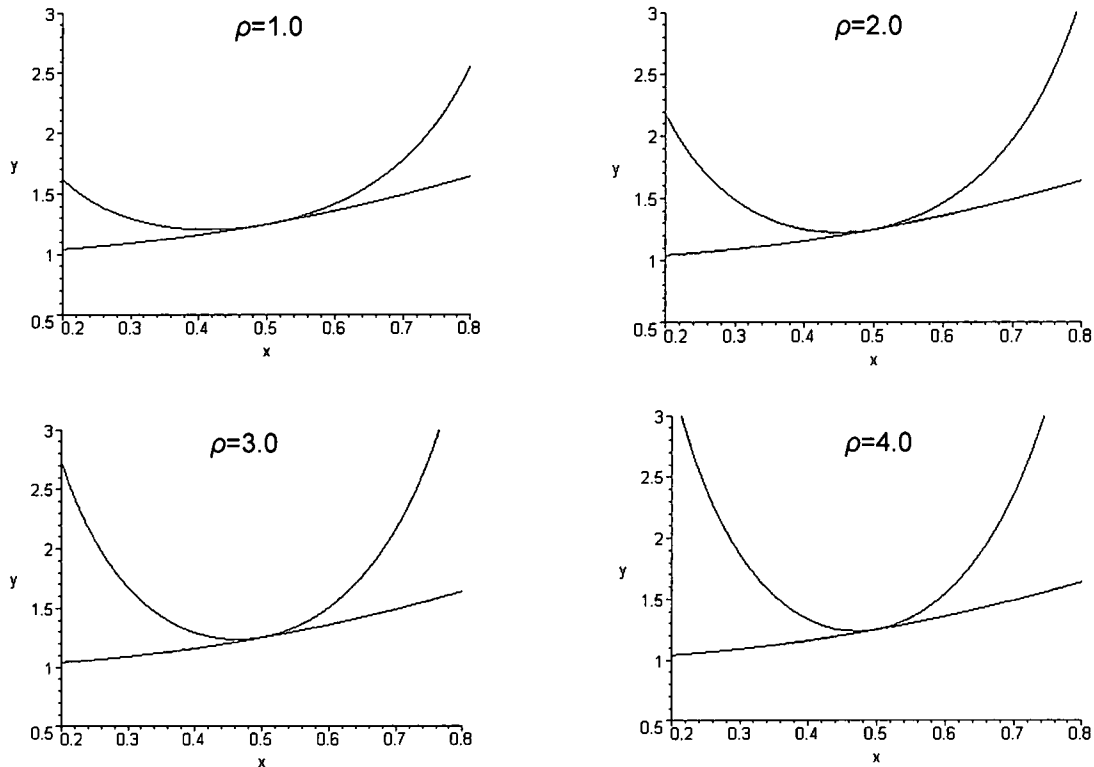


Figure 37 Effect of convexity parameter on the convex approximation

The upper and lower asymptote variables for each iteration point are selected as in the original MMA. For the first two outer iterations;

$$\begin{aligned} l_j^{(k)} &= x_j^{(k)} - 0.5(\hat{x}_j - \check{x}_j) \\ u_j^{(k)} &= x_j^{(k)} + 0.5(\hat{x}_j - \check{x}_j) \end{aligned} \quad (\text{B-5})$$

For subsequent iterations,

$$\begin{aligned} l_j^{(k)} &= x_j^{(k)} - \gamma_j^{(k)}(x_j^{(k-1)} - l_j^{(k-1)}) \\ u_j^{(k)} &= x_j^{(k)} + \gamma_j^{(k)}(u_j^{(k-1)} - x_j^{(k-1)}) \end{aligned} \quad \text{where,} \quad (\text{B-6})$$

$$\gamma_j^{(k)} = \begin{cases} 0.7 & \text{if } (x_j^{(k)} - x_j^{(k-1)})(x_j^{(k-1)} - x_j^{(k-2)}) < 0 \\ 1.2 & \text{if } (x_j^{(k)} - x_j^{(k-1)})(x_j^{(k-1)} - x_j^{(k-2)}) > 0 \\ 1.0 & \text{if } (x_j^{(k)} - x_j^{(k-1)})(x_j^{(k-1)} - x_j^{(k-2)}) = 0 \end{cases}$$

provided that the asymptotes do not violate inequalities,

$$\begin{aligned} l_j^{(k)} &\leq x_j^{(k)} - 0.01(\hat{x}_j - \check{x}_j) \\ l_j^{(k)} &\geq x_j^{(k)} - 10.0(\hat{x}_j - \check{x}_j) \\ u_j^{(k)} &\geq x_j^{(k)} + 0.01(\hat{x}_j - \check{x}_j) \\ u_j^{(k)} &\leq x_j^{(k)} + 10.0(\hat{x}_j - \check{x}_j) \end{aligned} \quad (\text{B-7})$$

If the above inequalities are violated, we change the violated inequalities into equalities and use them as new asymptotes. Since convexity parameters are positive quantities, we can be assured that the approximation will be convex. This implies that there is always a unique solution to the sub-problem:

$$\rho_i^{(1,0)} = 10^{-4} + \frac{0.1}{n} \sum_{j=1}^n \frac{\left| \frac{\partial f_i}{\partial x_j}(\mathbf{x}^{(1)}) \right|}{\hat{x}_j - \check{x}_j} \quad (\text{B-8})$$

$$\rho_i^{(k+1,0)} = \max \left\{ 0.1 \rho_i^{(k, \hat{v}(k))}, 10^{-7} \right\}$$

Here,  $\rho_i^{(k, \hat{v}(k))}$  is the latest convexity parameter from previous outer iteration,  $k$ . As mentioned previously, the convexity parameters are updated in each inner iteration. In each inner iteration, the updating of convexity parameters is based on the solution of the sub-problem from the previous inner iteration:

$$\rho_i^{(k, v+1)} = \max \left\{ 1.1 \rho_i^{(k, v)}, \min \left\{ 10 \rho_i^{(k, v)}, \rho_i^{(k, v)} + 1.1 \delta_i^{(k, v)} \right\} \right\} \quad \text{if } \delta_i^{(k, v)} > 0 \quad (\text{B-9})$$

$$\rho_i^{(k, v+1)} = \rho_i^{(k, v)} \quad \text{if } \delta_i^{(k, v)} \leq 0$$

where

$$\delta_i^{(k, v)} = \frac{f_i(\hat{\mathbf{x}}^{(k, v)}) - g_i^{(k, v)}(\hat{\mathbf{x}}^{(k, v)})}{\max \left\{ 10^{-7}, d^{(k)}(\hat{\mathbf{x}}^{(k, v)}) \right\}} \quad (\text{B-10})$$

$$d^{(k)}(x) = \sum_{j=1}^n \frac{\left( x_j^{\max} - x_j^{\min} \right) \left( u_j^{(k)} - l_j^{(k)} \right)}{\left( u_j^{(k)} - x_j \right) \left( x_j - l_j^{(k)} \right)} \left( x_j - x_j^{(k)} \right)^2 \quad (\text{B-11})$$

GCMMA sub-problem (B-4) is generated and solved in every outer and inner iterations. The sub-problem can be solved using several different approaches. Svanberg mentions two approaches: dual approach and primal-dual interior point approach. In dual approach, we solve the sub-problem in terms of Lagrange multipliers (dual variables). The dual sub-problem can be solved using unconstrained optimization techniques with special treatment to deal with non-negativity requirement of dual variables. For instance,

conjugate direction method (Fletcher-Reeves method) can be used. The primal-dual interior point approach is more involved with consideration of both primal and dual sub-problems. The appropriate approach (dual or primal) is selected within the solution procedure.

## REFERENCES

1. Joshi, J. P., Tidwell, Z., Crossley, W. A., and Ramakrishnan, S., "Comparison of Morphing Wing Strategies Based Upon Aircraft Performance Impacts," *Proceedings of the 45<sup>th</sup> AIAA/ASME/ASCE/AHS/ASC Structures, Structural Dynamics, and Materials Conference*, AIAA 2004-1722, Palm Springs, CA, 2004.
2. Bendsøe, M. P. and Sigmund, O., "Topology Optimization: Theory, Methods, and Applications," Springer, 2<sup>nd</sup>, 2004.
3. Gern, F. H., Inman, D. J., and Kapania, R. K., "Structural and Aeroelastic Modeling of General Planform Wings with Morphing Airfoils," *AIAA Journal*, Vol. 40, No. 4, 2002, pp. 628-637.
4. Prock, B., Weisshaar T. A, and Crossley, W. A., "Morphing Airfoil Shape Change Optimization with Minimum Actuator Energy as an Objective," *Proceedings of the 9<sup>th</sup> AIAA/ISSMO Symposium on Multidisciplinary Analysis and Optimization*, AIAA 2002-5401, Atlanta, GA, 2002.
5. Sanders, B. P., Reich G. W., Joo, J. J., and Eastep, F. E., "Air Vehicle Control Using Multiple Control Surfaces," *Proceedings of the 45<sup>th</sup> AIAA/ASME/ASCE/AHS/ASC Structures, Structural Dynamics, and Materials Conference*, AIAA 2004-1887, Palm Springs, CA, 2004.
6. Cook, A. and Crossley, W. A., "Genetic Algorithm Approaches to Smart Actuator Placement for Aircraft Flight Control," *Proceedings of the 41<sup>st</sup> AIAA/ASME/ASCE/AHS/ASC Structures, Structural Dynamics, and Materials Conference*, AIAA 2000-1582, Atlanta, GA, 2000.
7. Mattingly, M., Roemer, R. B. and Devasia, S., "Optimal Actuator Placement for Large Scale Systems: a Reduced-Order Modeling Approach," *International Journal of Hyperthermia*, Vol. 14, No. 4, 1998, pp. 331-345.
8. Liang, C., Sun, F. P. and Rogers, C. A., "Determination of Design of Optimal Actuator Location and Configuration Based on Actuator Power Factor," *Journal of Intelligent Material Systems and Structures*, Vol. 6, No. 4, 1995, pp. 456-464.
9. Sunar, M. and Rao, S. S., "Distributed Modeling and Actuator Location for Piezoelectric Control Systems," *AIAA Journal*, Vol. 34, No. 10, 1996, pp. 2209-2211.

10. Maghami, P.G., and Joshi, S.M., "Sensor/Actuator Placement for Flexible Space Structures," *IEEE Transactions on Aerospace and Electronic Systems*, Vol. 29, No. 2, 1993, pp. 345-351.
11. Padula, S. and Kincaid, R., "Optimization Strategies for Sensor and Actuator Placement," NASA TM 199 209126, 1999.
12. Joo, J. J., Sanders B P., and Washington, G., "Energy Based Efficiency of Adaptive Structures Systems," *Smart Materials and Structures*, Vol. 15, No 1, 2006, pp. 171-181.
13. Joo, J. J., Sanders, B. P., Johnson, T., and Frecker, M., "Optimal Actuator Location within a Morphing Wing Scissor Mechanism Configuration," *Proceedings of SPIE: Smart Structures and Materials Conference*, SPIE 6166-03, San Diego, CA, March 2006.
14. Pedersen, C. B. W., Buhl, T., and Sigmund, O., "Topology Synthesis of Large-displacement Compliant Mechanisms," *International Journal for Numerical Methods in Engineering*, Vol. 50, pp. 2683-2705.
15. Kawamoto, A., "Path-Generation of Articulated Mechanisms by Shape and Topology Variations in Non-linear Truss Representation," *International Journal of Numerical Methods in Engineering*, Vol. 64, No. 12, 2005, pp. 1557-1574.
16. Maute, K., Reich, G., and Sanders, B., "In-Plane Morphing Designs by Topology Optimization," *15<sup>th</sup> International Conference on Adaptive Structures and Technologies*, Paris, France, Oct. 9-12, 2005.
17. Maute, K. and Reich, G., "Integrated Multidisciplinary Topology Optimization Approach to Adaptive Wing Design," *AIAA Journal of Aircraft*, Vol. 43, No. 1, 2006, pp. 253-263.
18. Lu, Kerr-Jia and Kota, Sridhar, "Design of Compliant Mechanisms for Morphing Structural Shapes," *Journal of Intelligent Material Systems and Structures*, Vol. 14, No. 6, 2003, pp. 379-391.
19. Lu, K.-J., and Kota, S., "An Effective Method of Synthesizing Compliant Adaptive Structures using Load Path Representation," *Journal of Intelligent Material Systems and Structures*, Vol. 16, No. 4, 2005, pp. 307-317.
20. Ramrakhyani, D., Lesieutre, G., Frecker, M., and Bharti, S., "Aircraft Structural Morphing using Tendon-Actuated Compliant Cellular Trusses," *AIAA Journal of Aircraft*, Vol. 42, No. 6, 2005, pp. 1615-1621.
21. Bharti, S., Frecker, M., and Lesieutre, G., "Optimal Structural Design of a Morphing Wing using Parallel Non-Dominated Sorting Genetic Algorithm II (NSGA II),"

- Proceedings of SPIE: Smart Structures and Materials Conference*, SPIE6166-02, San Diego, CA, March 2006.
22. Inoyama, D., Sanders, B., and Joo, J., "Conceptual Design and Multidisciplinary Optimization of In-plane Morphing Wing Structures," *Proceedings of SPIE: Smart Structures and Materials Conference*, SPIE 6166-01, San Diego, CA, March 2006.
23. Gano, S., Perez, V., Renaud, J., and Batill S., "Multilevel Variable Fidelity Optimization of a Morphing Unmanned Aerial Vehicle," 45<sup>th</sup> AIAA/ASME/ASCE/AHS/ASC Structures, Structural Dynamics & Materials Conference, AIAA2004-1763, Palm Springs, CA, 19-22 April 2004.
24. Hetrick, J., and Kota, S., "An Energy Formulation for Parametric Size and Shape Optimization of Compliant Mechanisms," *Journal of Mechanical Design*, Vol. 121, 1999, pp. 229-234.
25. Trease, B., and Kota, S., "Synthesis of Adaptive and Controllable Compliant Systems with Embedded Actuators and Sensors," *Proceedings of IDETC/CIE*, DETC2006-99266, Philadelphia, PA, September 2006.
26. Vanderplaats, G. N., "Numerical Optimization Techniques for Engineering Design," 3<sup>rd</sup> edition, Vnaderplaats Research & Development, Inc., Colorado Springs, CO, 1999.
27. Svanberg K., "The method of Moving Asymptotes – A New Method for Structural Optimization," *International Journal of Numerical Methods and Engineering*, Vol. 24, No. 2, 1987, pp. 359-373.
28. Svanberg K., "A Globally Convergent Version of MMA without Line Search," *Proceedings of the First World Congress of Structural and Multidisciplinary Optimization*, Goslar, Germany, 1995, pp. 9-16.
29. Rodden, W. P. and Johnson, E. H., "MSC.NASTRAN: Aeroelastic Analysis," The Macneal-Schwendler Corporation, version 68, 1994.
30. ASTROS Theoretical Manual, Universal Analytics, Inc., 1997.
31. Frecker, M., Ananthasuresh, G., Nishiwaki, G., Kikuchi, N., Kota, S., "Topological Synthesis of Compliant Mechanism using Multi-criteria Optimization," *ASME Journal of Mechanical Design*, Vol. 119, No. 2, 1997, pp. 238-245.
32. Frecker, M., "Recent Advances in Optimization of Smart Structures and Actuators," *Journal of Intelligent Material Systems and Structures*, Vol. 14, No. 4-5, 2003, pp. 207-216.

33. Saxena A, "Topology Design of Large Displacement Compliant Mechanisms with Multiple Materials and Multiple Output Ports," *Structural and Multidisciplinary Optimization*, Vol. 30, No. 6, 2005, pp. 477-490.
34. Buhl, T., "Simultaneous Topology Optimization of Structure and Supports," *Structural and Multidisciplinary Optimization*, Vol. 23, No. 5, 2002, pp. 336-346.
35. Kudva, J., "Overview of the DARPA Smart Wing Project," *Journal of Intelligent Material Systems and Structures*, Vol. 15, No. 4, 2004, pp. 261-267.
36. Bowman, J., Sanders, B., and Weisshaar, T., "Identification of Military Morphing Aircraft Missions and Morphing Technology Assessment," *Proceedings of SPIE: Smart Structures and Materials Conference*, SPIE 4698-62, San Diego, CA 2002, pp.121-132.
37. Austin, F., Rossi, M. J., Van Nostrand, W., Knowles, G., "Static Shape Control for Adaptive Wings," *AIAA Journal*, Vol. 32, No.9, 1994, pp. 1895-1901.
38. Hall, J., "Executive Summary AFTI/F-111 Mission Adaptive Wing," Wright Research Development Center, Rept. WRDC-TR-89-2083, Wright-Patterson AFB, OH, Sept. 1989.
39. Miller, G., "Active Flexible Wing Technology," Rockwell International, Rept. AFWAL-TR-87-3096, Wright-Patterson AFB, OH, Feb. 1987.
40. Cook, R. D., Malkus, D. S., and Plesha, M. E., Witt, R. J., "Concepts and Applications of Finite Element Analysis," John Wiley & Sons, 4<sup>th</sup>, 2002.
41. Katz, J. and Plotkin, A., "Low-Speed Aerodynamics," Cambridge University Press, 2<sup>nd</sup>, 2001.
42. Bertin, J. J., and Smith, M. L., "Aerodynamics for Engineers," Prentice Hall, 2<sup>nd</sup>, 1989.
43. Anderson, J. D., "Fundamentals of Aerodynamics," McGraw Hill, 3<sup>rd</sup>, 2001.
44. Kincaid D. and Cheney W., "Numerical Analysis: Mathematics of Scientific Computing," 3<sup>rd</sup>, Brooks/Cole, 2002.



R702033556